RPN 94

**DASA 2477**

Final Report

# DIAGNOSTICS AND APPLICATIONS OF PULSED SELF-FOCUSED RELATIVISTIC ELECTRON BEAMS

Covering the Period 1 March through 31 December 1969

Submitted Under:

Contract DA-49-146-XZ-553 (III)

Submitted to:

Defense Atomic Support Agency
Washington, D.C.

THIS RESEARCH HAS BEEN SPONSORED BY THE DEFENSE ATOMIC SUPPORT AGENCY UNDER NWER SUBTASK LA013 CONTRACT DA-49-146-XZ-553 (III)

ION PHYSICS CORPORATION
BURLINGTON, MASSACHUSETTS

# FOREWORD

During the period of this contract, March through December, 1969, studies of pulsed electron beams with energies from 400 keV to 2.6 MeV and currents of 17 kA to 40 kA were conducted covering beam propagation, beam diagnostics and ion acceleration. The contributors to this report are:

| | |
|---|---|
| S.E. Graybill | Project Manager and experimental studies of beam motion, ion acceleration and diagnostic development. |
| J.R. Uglum | Analytical studies, ion acceleration mechanism, analysis of ion acceleration data. |
| W.H. McNeill | Analytical studies |
| J.E. Rizzo | Laser interferometry, ion magnetic analysis |
| R. Lowell | 400 keV beam studies |
| G. Ames | Experimental work and data reduction. |

Others who contributed significantly to the program are S.V. Nablo and R.N. Cheever. Assistance through the loan of equipment and advice on its use was provided by A. Guenther of AFWL for the Q-switched laser, W.R. Van Antwerp of USANDL for the electron magnetic spectrometer and W. Lupton of NRL for the silver activation neutron detector.

# ABSTRACT

During the period of March through December 1969 the following investigations were conducted under Contract DA-49-146-XZ-553 (III).

## DIODE DIAGNOSTICS

To compliment the time resolved diode current information which is measured on each machine firing, a coaxially mounted capacitive voltage monitor was designed and constructed early in this program. The voltage monitor views the shank supporting the cathode a few inches behind the cathode. To correct for the inductive voltage drop between the monitor and cathode, short circuit measurements are made to determine the effective inductance of that short section of line. All non-shorted voltage measurements are then corrected for the inductive contribution to the signal.

The voltage and current monitors, which are individually calibrated using a short pulse transmission line assembly, have allowed us to not only measure the time-resolved impedance of various diode configurations, but also cross-check other measurements such as total energy calorimeter measurements and electron beam spectra obtained with a magnetic spectrometer. In all cases the cross-checking of diagnostics has been most successful (± 10% agreement).

The ability to time-resolve the impedance of various diodes has proved to be very useful in understanding diode behavior. A brief summary of the results include:

(a) A 7-10 ns formative time period is necessary before the diode reaches its steady impedance level.

(b) Carbon cathodes have a shorter formative time period than do metal cathodes (aluminum, brass, stainless steel).

(c) The time to diode closure is a function of anode material. Specifically, a somewhat longer time duration occurs before closure when carbon anodes are used.

(d) The diode impedance depends linearly on the ratio (d/r), (when d = anode - cathode spacing and r = cathode radius), not quadratically. This result is in agreement with the predictions of parapotential flow and disagrees with the Langmuir-Childs law.

## BEAM PROPAGATION

It had been known from previous work that, for electron beams with $\nu/\gamma \geq 1$, the pressure regime of 1 Torr gives the most efficient energy transport. These earlier results were primarily based on calorimetric measurements. We have now used the reproducibility of our machine to measure both the current and spectral quality of the beam as a function of longitudinal distance from the entrance plane. The most striking feature is that the spectral quality of the beam is preserved over as much as a 3 meter drift length when the drift tube pressure is at 1 Torr. For pressures above and below this, the spectral quality is degraded to lower energies as the drift distance increases. Also, under the best drift conditions of 1 Torr, 75% of the beam energy can be transported over 3 meters.

Other beam propagation studies included the study of beam front propagation under varying pressure conditions. Two diagnostic tools were used for this experiment. The first consisted of a return current shunt to measure the arrival of the beam current. The second measurement used a thin Ta converter to register the arrival time of high energy electrons, not the lower energy electrons which could correspond to a degraded beam front. The results in air can be summarized as:

(a) In the 0.1 Torr range the beam front velocity starts out low, and then is "accelerated" to a velocity corresponding to roughly injection conditions. At higher pressures

(0.5 Torr) the beam front is decelerated and at 1.0 Torr (and 0.05 Torr) the velocity is roughly constant.

(b) The "velocity" profile for both measurements are roughly equivalent, but there is a time delay between the arrival of the current pulse and the arrival of energetic electrons. In most cases the time difference is only a few nanoseconds, which is consistent with the finite rise-time of the injected pulse.

## ION ACCELERATION STUDIES

This work was a continuation of the studies, started under the previous phase of this contract, to investigate the phenomena by which ions are accelerated by linear electron beams. The most significant new results consist of:

(a) improved time-of-flight measurements indicate, that for $H^+$ and $D^+$, the ion energy is pressure dependent. The maximum energy occurs for a filling pressure of 0.2 Torr.

(b) Range measurements have been used to identify clearly the atomic constituent in the ion beam. In all cases only ions corresponding to the filling gas were accelerated.

(c) Magnetic spectrometer measurements were used to identify charge states of the ions. $He^{++}$ was the main component for helium filling gas. For nitrogen, the main charge state corresponded to six-times ionized nitrogen. For argon the results showed 12-times ionized charge states.

The study of this ion acceleration process has led us to propose two possible applications of this beam. One is to use the ion beam as a source of pulsed, high energy neutrons. Fluence levels of $10^{10}/cm^2$ are probably attainable. The second application consists of using the ion beam to generate K-shell conversions in metal targets. The resulting X-ray yield could be used to calibrate the spectral and time response of diagnostic tools used as X-ray detectors.

## LASER INTERFEROMETRY

A Q-spoiled laser was used in conjunction with a multi-pass Mach-Zender interferometer to determine early time electron densities in beam plasma systems. The results show that nearly complete ionization in the plasma volume is achieved very early in time (less than 200 ns in helium). The measurements further indicated that the plasma pinches subsequent to the electron beam pulse and then slowly expands on a long time scale.

## THEORETICAL STUDIES

Besides carrying out a fairly detailed calculation on the generation of plasma return currents and also developing a computer code to study the dynamics of electron beam flow in a beam-plasma system, a physical model was constructed which explains the experimental results relating to the ion acceleration process. The model is that of an accelerated potential well, with the electron beam being the source of the well and avalanche breakdown the mechanism by which the well is accelerated. This model can now be used to understand the scaling laws for ion energy.

# TABLE OF CONTENTS

TABLE OF CONTENTS (Continued)

## LIST OF ILLUSTRATIONS

## LIST OF ILLUSTRATIONS (Contined)

## LIST OF ILLUSTRATIONS (Continued)

## LIST OF ILLUSTRATIONS (Continued)

# SECTION 1

# ELECTRON BEAM DIAGNOSTICS

## 1.1 Introduction

The primary diagnostics used in these studies are the return current shunt, capacitive voltage monitor, magnetic spectrometer, and calorimeter. The optical diagnostics and the accelerated ion diagnostics are covered in their individual sections.

The return current shunts shown in Figure 1 have been completely described in previous reports on this contract.(1) The magnetic spectrometer has also been discussed in detail in these reports.

## 1.2 Voltage Monitor

During this contract phase (III) a capacitive voltage divider was fabricated to give the voltage-time signature associated with the diode. If $C_1$ is the capacitive coupling to the cathode and $C_2$ is the probe capacitance then the output voltage is:

$$V_{out} = \frac{C_1}{C_2} \frac{Z_o}{(R_L + Z_o)} V_c \text{ if } C_2 >> C_1$$

$Z_o$ is the oscilloscope impedance and $R_L$ the load resistance. Since $C_2$ $(R_L + Z) = \tau$ the decay time which must be much greater than the pulse width, and $Z_o$ is in practice 50 or 125 ohms, then $C_1$ is fixed and there remains a free choice between $R_L$ and $C_2$. The defining of $C_1$ means that the area of the probe is defined and the choice between $R_L$ and $C_2$ amounts to the choice of dielectric thickness.

In order to link as little length of the cathode as possible, the monitor was made as a band encircling the cathode in the post-tube section. It is positioned five inches back from the anode. The signal is brought out through a 50 ohm vacuum line to a 50 ohm G.R. connector. The load resistor is as

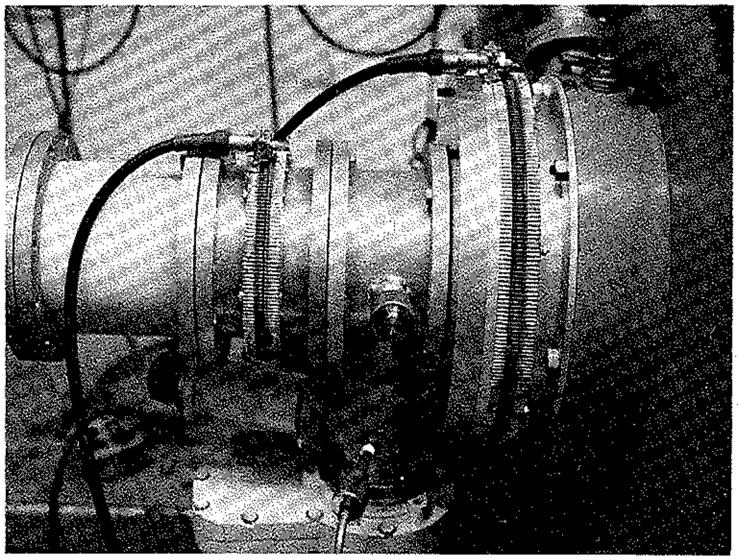

Figure 1 Drift Tube and Field Emission Tube Current Shunts

2-779

close to the monitor as possible. A guard ring of the same capacitance, and with a resistance of $(R_L + Z_o)$ to ground, is on each side of the active element. The rings reduce the fringe fields of the monitor. The device in position is shown in Figure 2.

The calibration of the current and voltage diagnostics is accomplished with tapered transmission lines of constant impedance. A modular set up was manufactured so that tapered lines are available to fit any of the drift tube sizes or the exit sections of either FX-25 or FX-1. The tapered section and diagnostic section have a nominal impedance of 50 ohms. The continuity of the impedance is checked with a Tektronix TDR. A pulse is launched from a transmission line (square wave) pulser, and is monitored at the end of the calibration line. The pulse from the current sensor is monitored on a sampling scope or on a Tektronix model 581. In this way the sensor is calibrated and its risetime measured. The arrangement is shown in Figure 3 where a pickup loop in a 6-inch pipe is under test. The conical sections seen in the background are for tapering up to the field emission tube diameter. The tapered line is also helpful in the design phase of diagnostic gear.

The response of the voltage monitor is shown in Figure 4, where it is seen that the risetime is subnanosecond. The slump was shown to be 0.4 μs ($e^{-1}$ time) in another test.

The calibration of the monitor depends on the cathode shank diameter through the parameter

$$C_1 = \frac{2\pi\epsilon_o}{\ln r_o/r_c} L$$

where L is the length of the monitor, $r_o$ and $r_c$ are the radii of the tube extension and cathode respectively. The calibration has been done both with the 50 ohm transmission line test set up and by use of the Be (γ, n) threshold (1.67 MeV) determination. The calibration with the 1/8-inch shank did not agree with the others, and the measurements of the high impedance gap that is produced by this shank were erratic. This is probably due to the cloud of

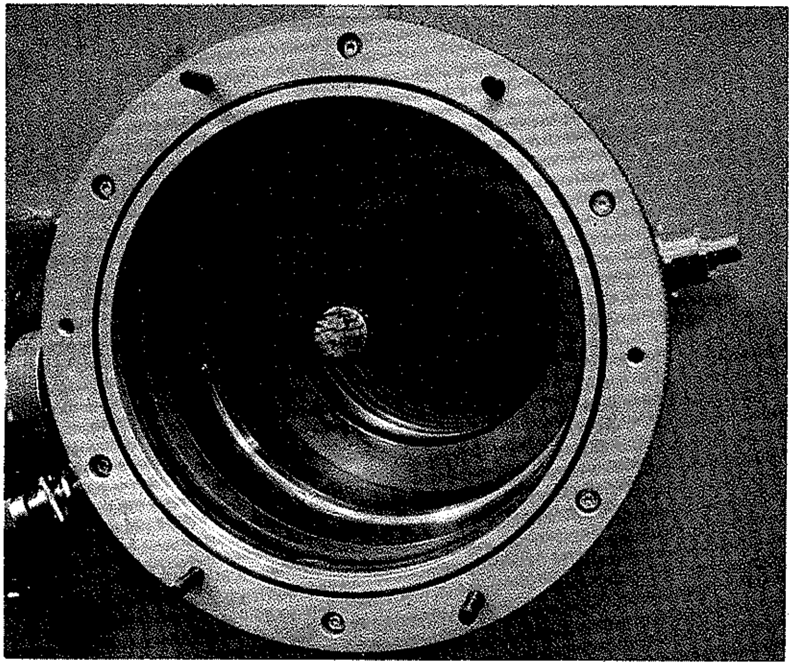

Figure 2 Capacitive Voltage Monitor and Return Current Shunt

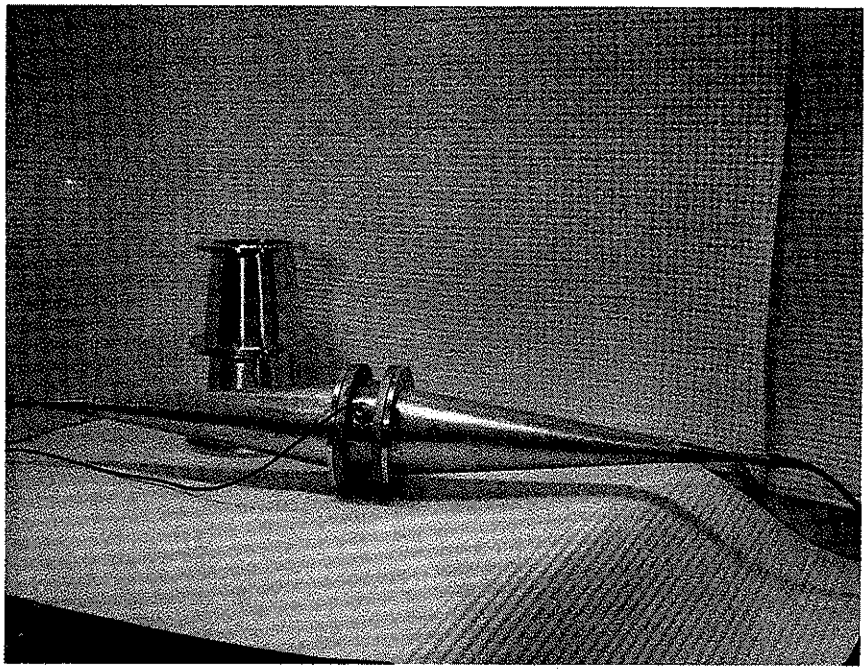

Figure 3 Calibration of Current Sensor with Tapered Transmission Line

2-1206

Sampling Oscilloscope Traces

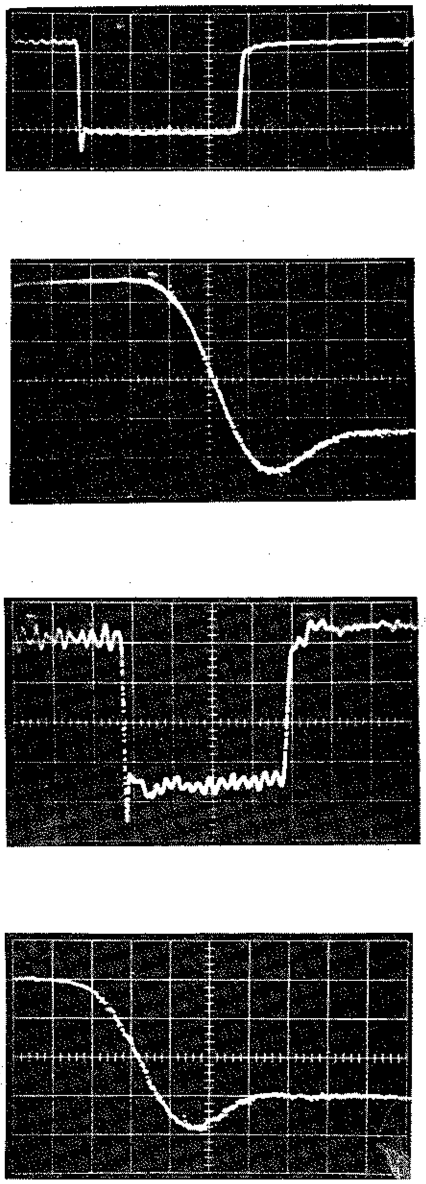

Test Pulse

5 ns/cm

0.2 ns/cm

Voltage Monitor Output

5 ns/cm

0.2 ns/cm

Figure 4 Biconical Transmission Line Calibration of Capacitive Voltage Monitor

2-1386

electrons emitted from the shank. It is known that more emission occurs from this shank than from larger diameter ones,(1) and with a high impedance gap (> 100 ohms) the electrons will be trapped at a greater radius than is the case with the low impedance gaps. This is probably the reason that the calibration gives a higher sensitivity than is calculated.

The voltage and current sensors are used simultaneously to obtain the time resolved current-voltage characteristics of the field emission diode. The oscilloscopes used to record the signals are synchronized by use of a square wave pulser. The resulting current-voltage traces for a 150 ohm and a 40 ohm gap are shown in Figure 5.

The traces must be corrected for the inductive contribution. The trace as displayed on the scope is $V_c + Li$, where L is the inductance of the cathode from the point of the monitor to the gap. This effective inductance is measured by shorting the gap and simultaneously measuring the short circuit current and the resultant voltage which is Li. One then differentiates the current pulse or integrates the voltage trace to ascertain L. This only needs to be done once for each cathode set-up.

Once the value of L is obtained, the voltage pulses can be corrected by differentiating the current pulse and subtracting Li. We have developed a computer program on our time-shared facility for doing this. This program also calculates impedance, $\nu/\gamma$, energy spectrum, power transmitted and total energy.

## 1.3 Calorimeter

The final diagnostic tool to be discussed is a total energy calorimeter which is simply a 5-inch aluminum disc with a thermocouple at the center and edge. The equilibrium temperature is related to the total energy incident on it.

## 1.4 Experimental Results

The most extensively studied beam is the one produced by the 20 pin cathode at a 2.0 cm spacing.

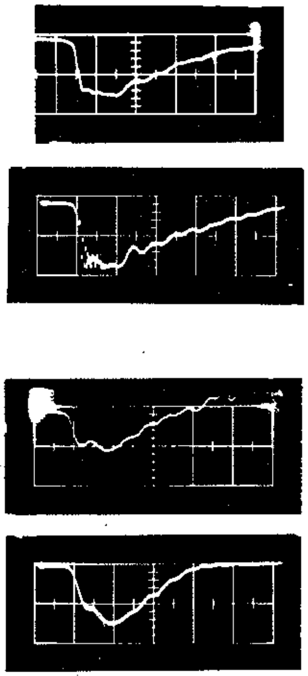

1. 7 MV/div
20 ns/div

13 kA/div
20 ns/div

1/8 inch Diameter
Hemispherical Cathode
2. 7 cm Gap

1. 7 MV/div
20 ns/div

26 kA/div
20 ns/div

20 Point Cathode
2. 0 cm Gap

Figure 5 Voltage and Current Pulses

Figure 6 shows the corrected voltage pulse, the current pulse, impedance and $\nu/\gamma$, all on a common time base. It is seen that the cathode takes about 8 ns to reach its stable operating level. The impedance falls continuously, but $\nu/\gamma$ is reasonably constant.

The calculated and measured energy transfer with the gap are in excellent agreement as shown.

The spectra calculated from the I, V profiles and those measured with the magnetic spectrometer should agree as to end point energy and location of maxima. The relative heights will not in general agree because the beam profile probably changes as $\nu/\gamma$ increases with time. The I, V calculated spectrum takes the entire beam into account where the spectrometer measures only the portion of the beam that is paraxial. This means that only the central portion of the beam is measured, regardless of drift conditions, since any electrons deflected in from off axis positions cannot be paraxial. The same argument holds for electrons emitted from the cathode shank and pinched in at the anode.

Figure 7 shows the spectrum derived from the current-voltage waveforms for the 20 pin cathode shown in Figure 6. Figure 8 shows the magnetically analyzed data for the same gap. The locations of the 1.5 MeV and 1.2 MeV peaks agree well but the 0.9 MeV peak that appears in the magnetic data does not appear in the I, V data. In Figure 6 it is seen that this voltage level occurs just as $\nu/\gamma$ is reaching its equilibrium value, so it could be due to a shift of current density in the cathode tip due to the plasma formation.

In Figure 9 is shown the current, voltage, impedance and $\nu/\gamma$ data for a 1.7 cm diameter carbon cathode and a spacing of 1.5 cm. This configuration gives a slightly higher impedance than the 20 pin geometry and was used for the recent ion work.

Figures 10 and 11 show the spectra calculated from the I, V characteristic and obtained from magnetic analysis. The agreement is quite good.

Figure 12, 13 and 14 show the same data for the 1/8-inch diameter, hemispherical end cathode. This is the one for which the calibration difficulties previously discussed arose. The basic voltage calibration used here was the $D_2(\gamma, n)$ reaction threshold at 2.23 MeV. The sensitivity of the voltage monitor

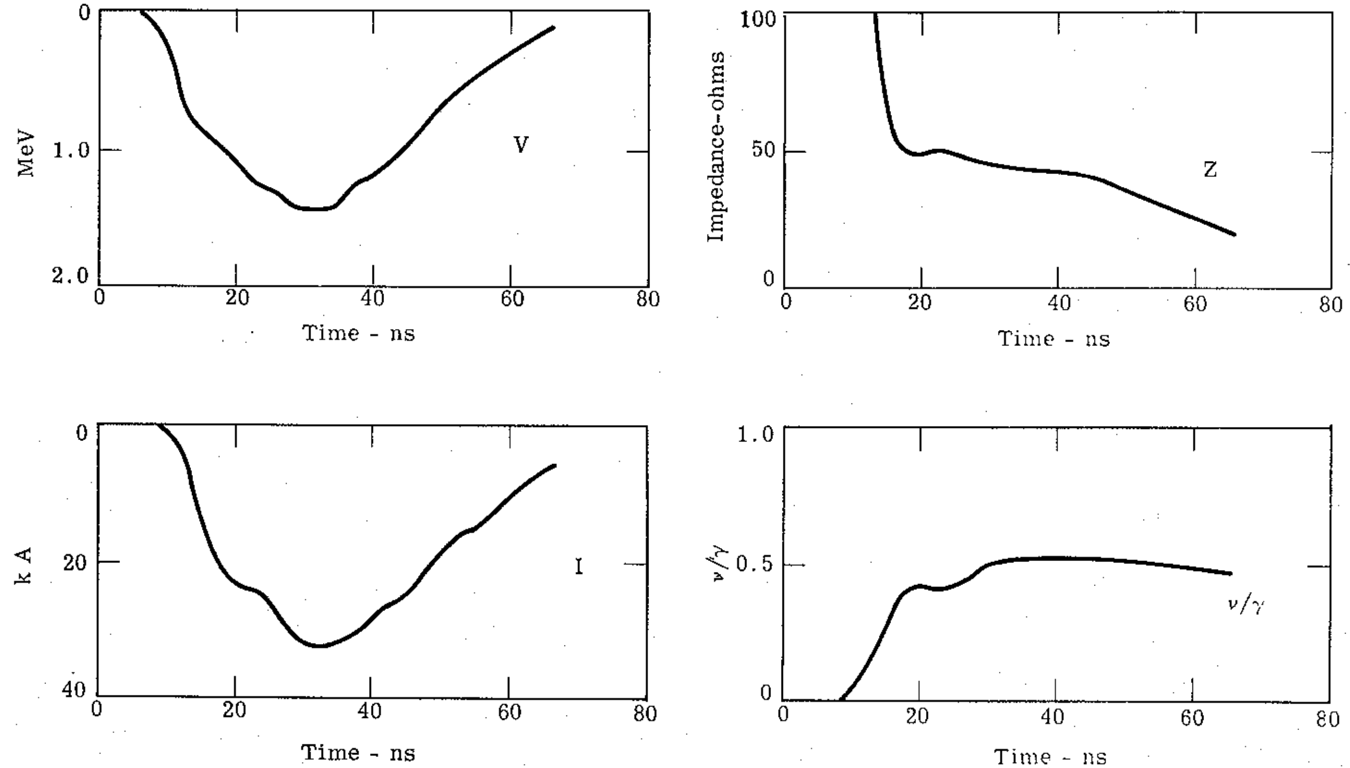

20 Pin Cathode
2.0 cm Gap, 3 inch Window
$\int I(t)\,V(t)\,dt = 1.2$ kJ
Calorimeter = 1.2 - 1.3 kJ

Figure 6. Field Emission Diode Characteristics

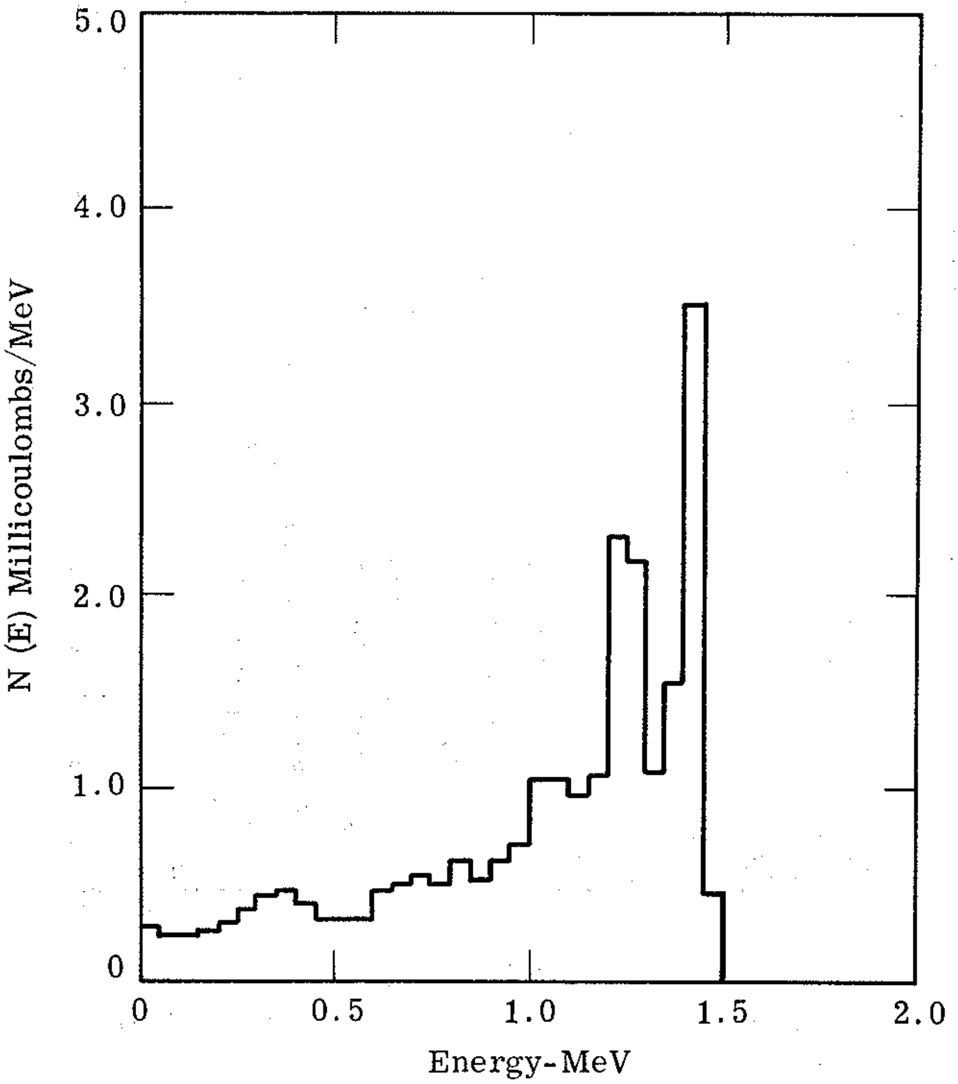

20 Pin Cathode
2.0 cm Gap 3 inch Window

Figure 7. Energy Spectrum Derived from Current-Voltage Waveforms

1-4454

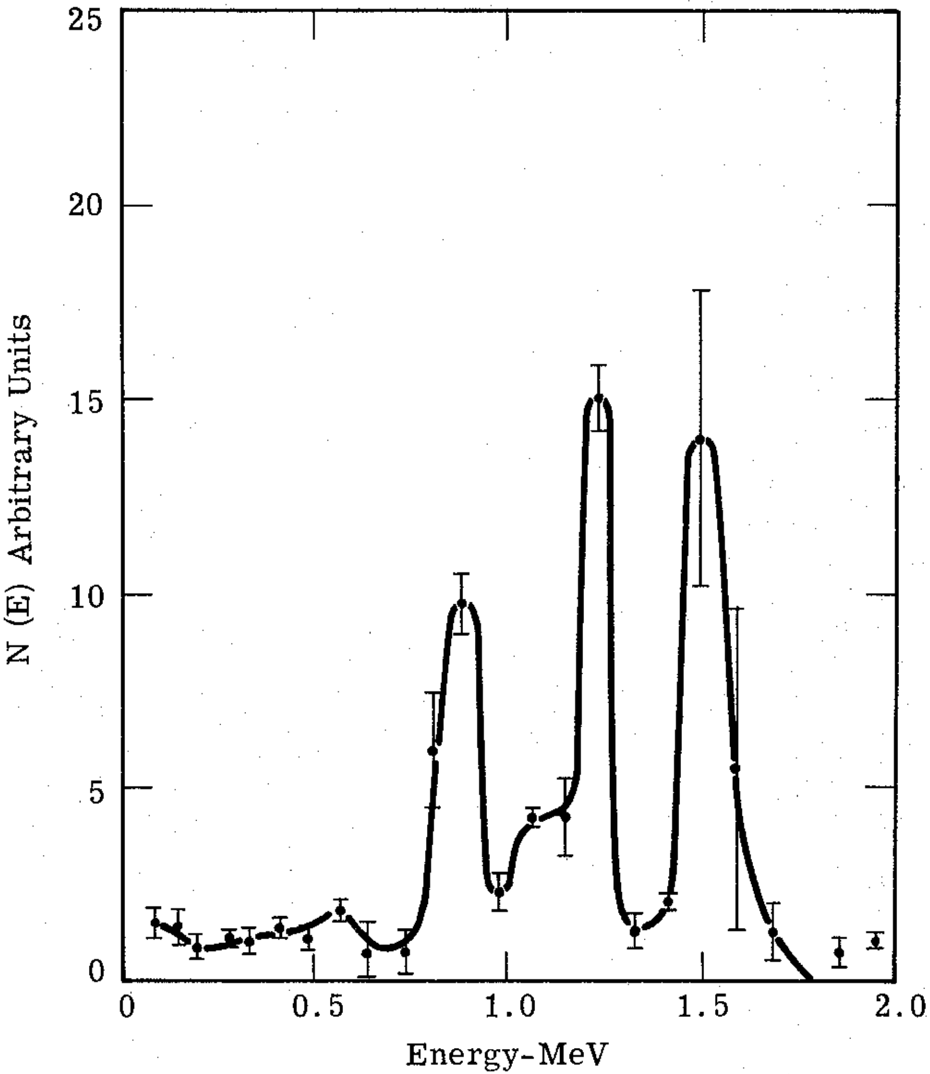

20 Pin Cathode, 2.0 cm Gap, 3 inch Window

Figure 8. Magnetically Analyzed Energy Spectrum

1-4455

1-4456

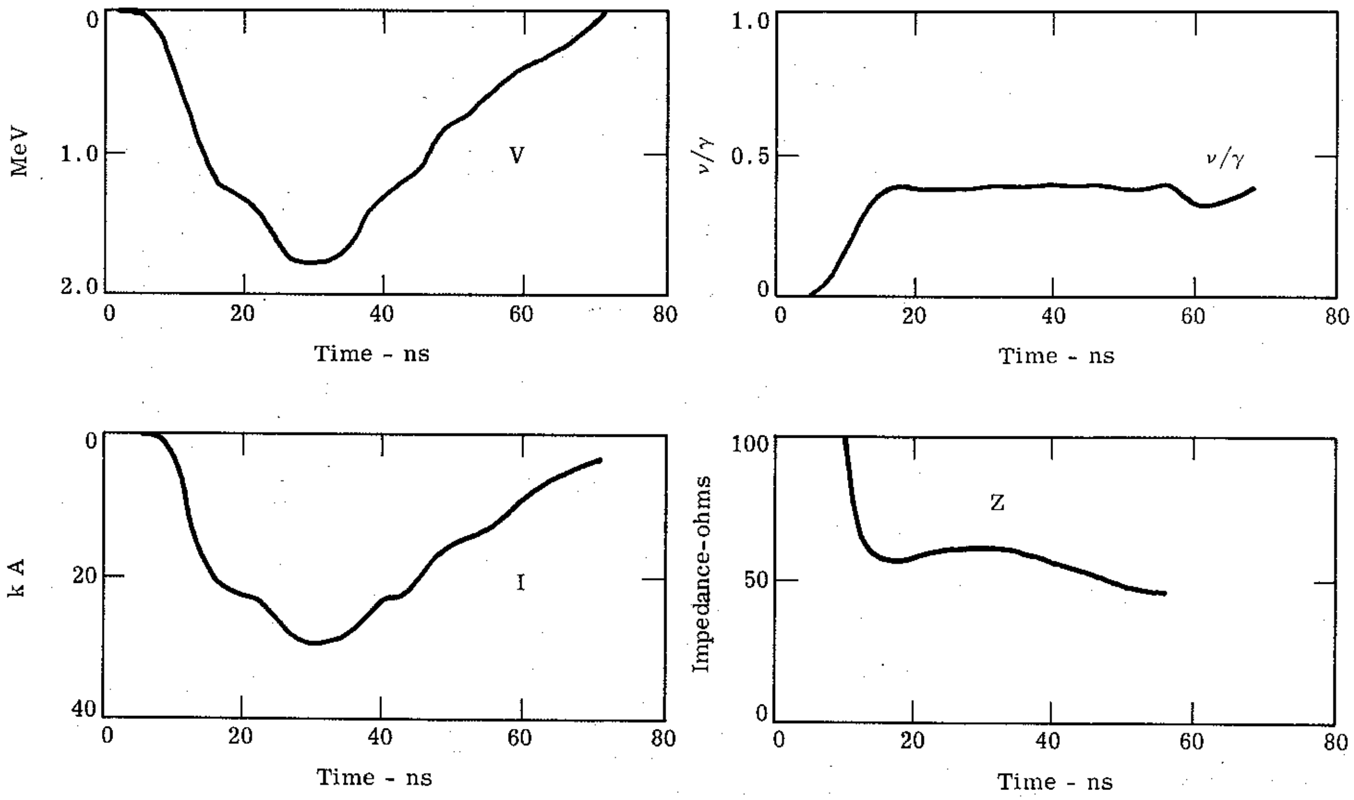

Carbon Cathode
1.7 cm dia, 1.5 cm Gap
$\int I(t)\,V(t) = 1.3$ kJ

Figure 9. Field Emission Diode Characteristics

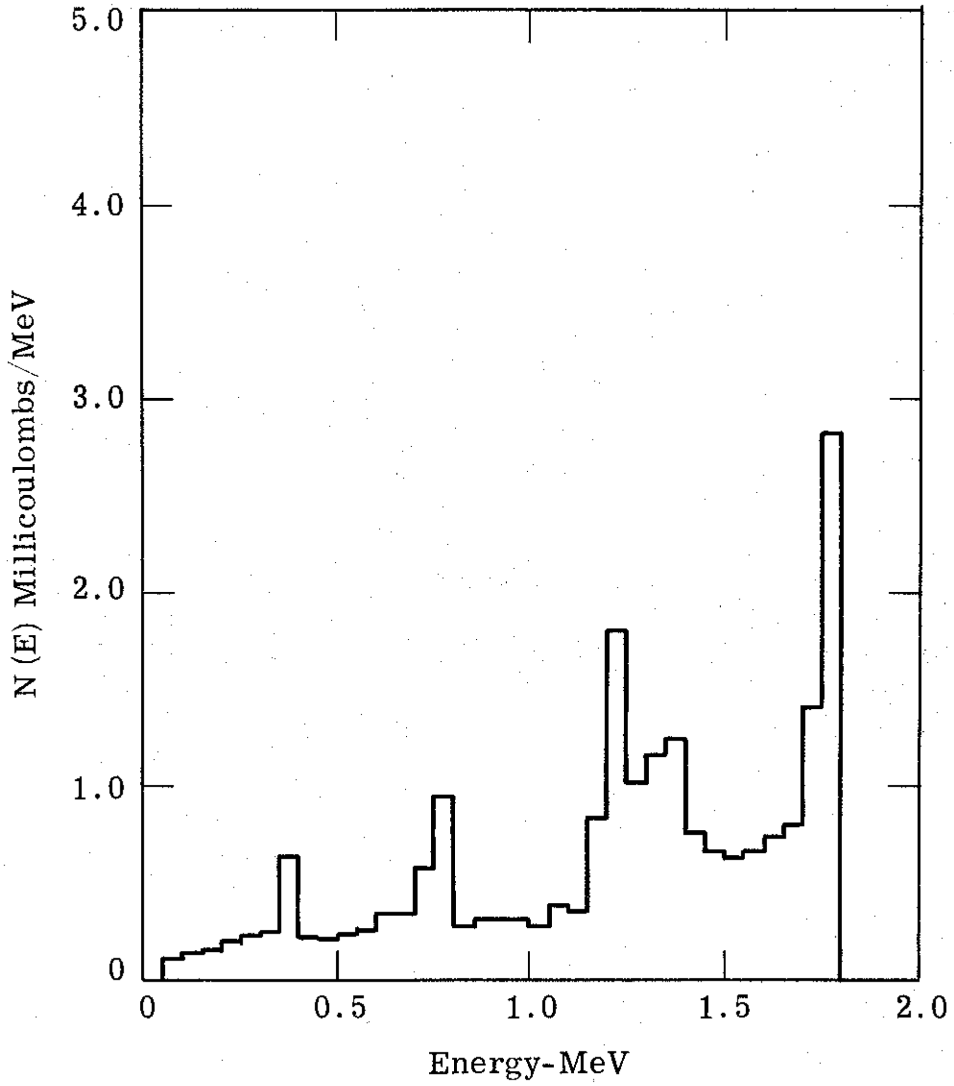

Carbon Cathode
1.7 cm dia, 1.5 cm Gap

Figure 10. Energy Spectrum Derived from Current-Voltage Waveforms

1-4457

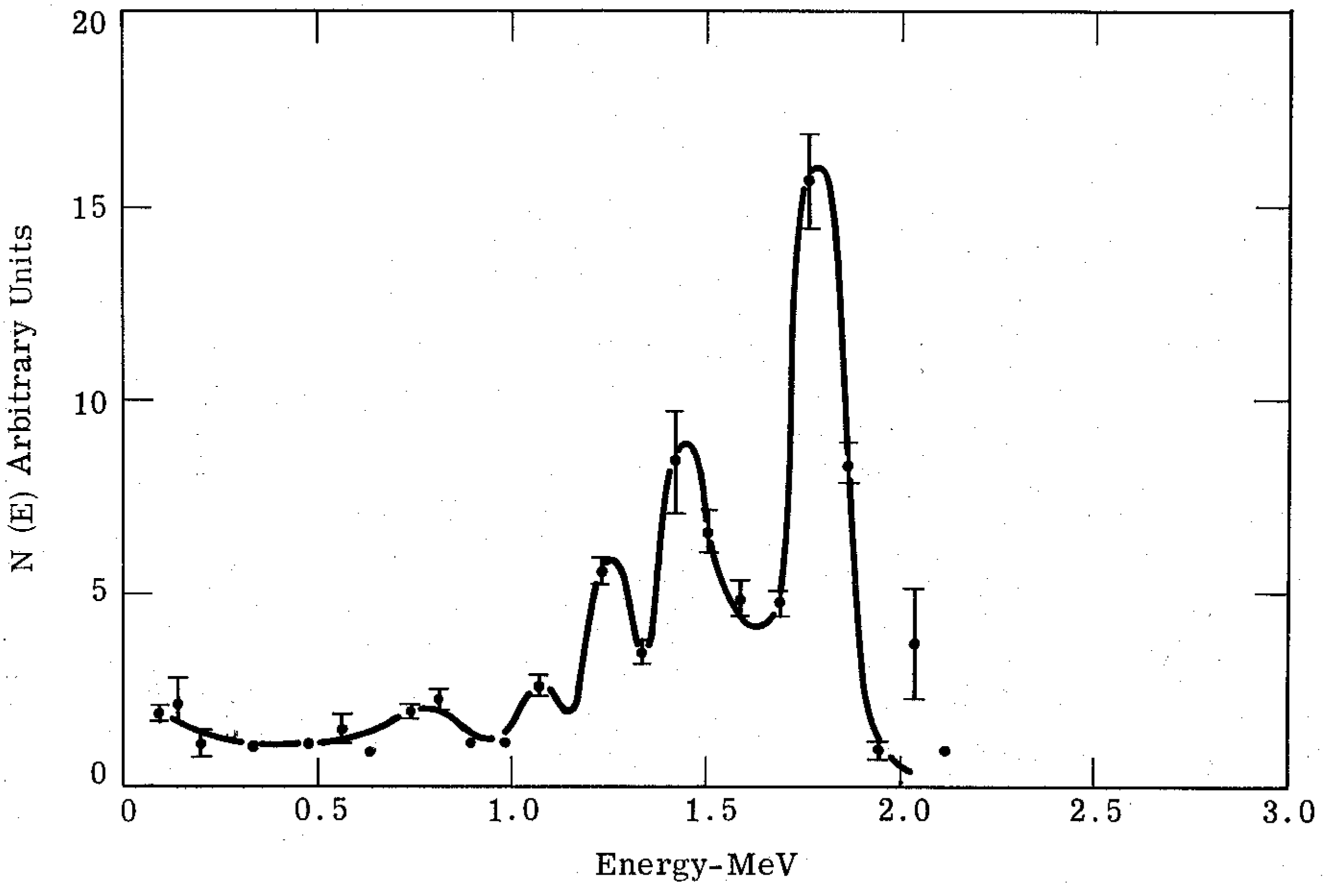

Carbon Cathode
1.7 cm dia, 1.5 cm Gap, 3 inch Window

Figure 11. Magnetically Analyzed Energy Spectrum

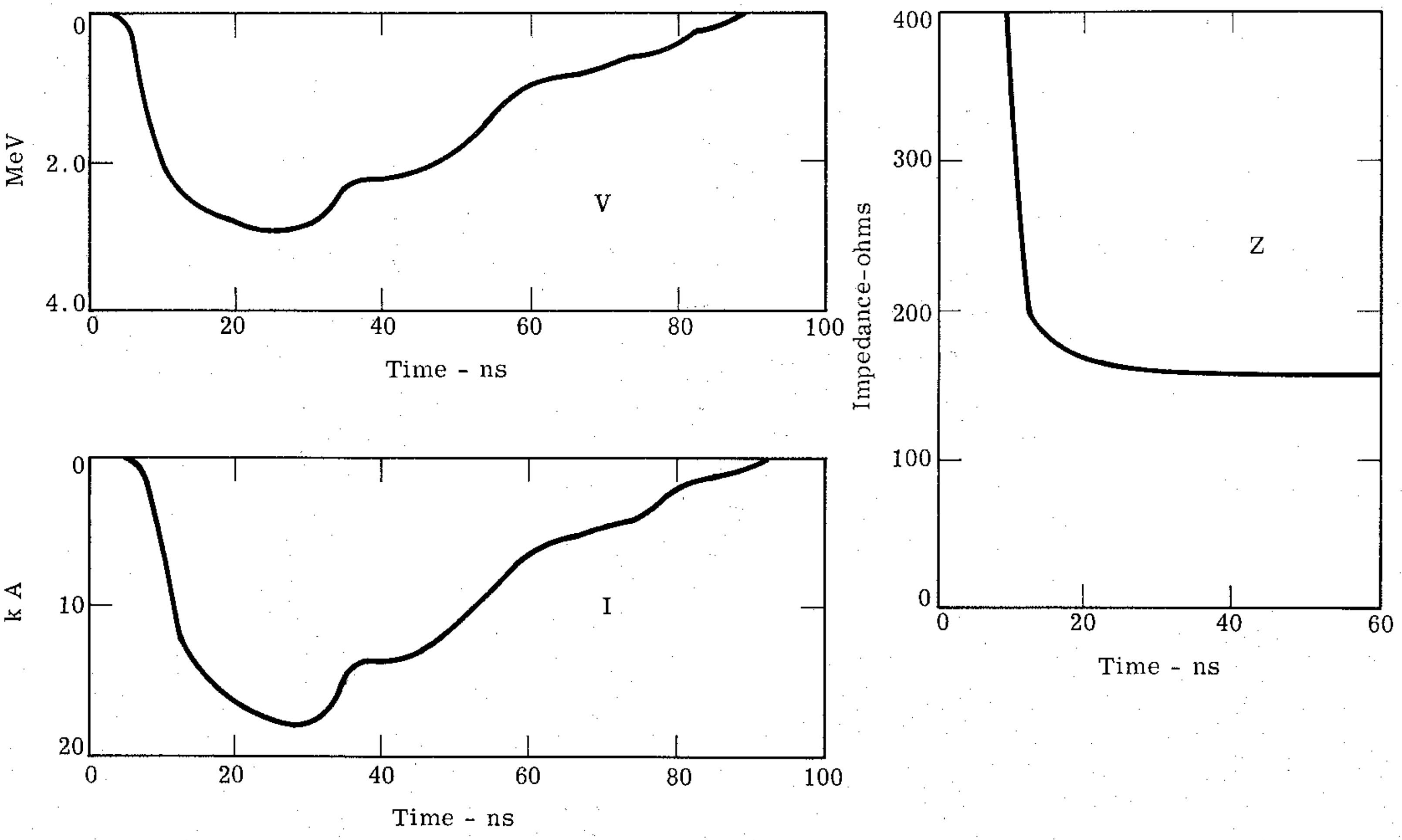

1/8 inch Cathode
2.7 cm Gap, 3 inch Window
$\int I(t)\ V(t) = 1.7$ kJ
Calorimeter - 1.3 kJ

Figure 12. Field Emission Diode Characteristics

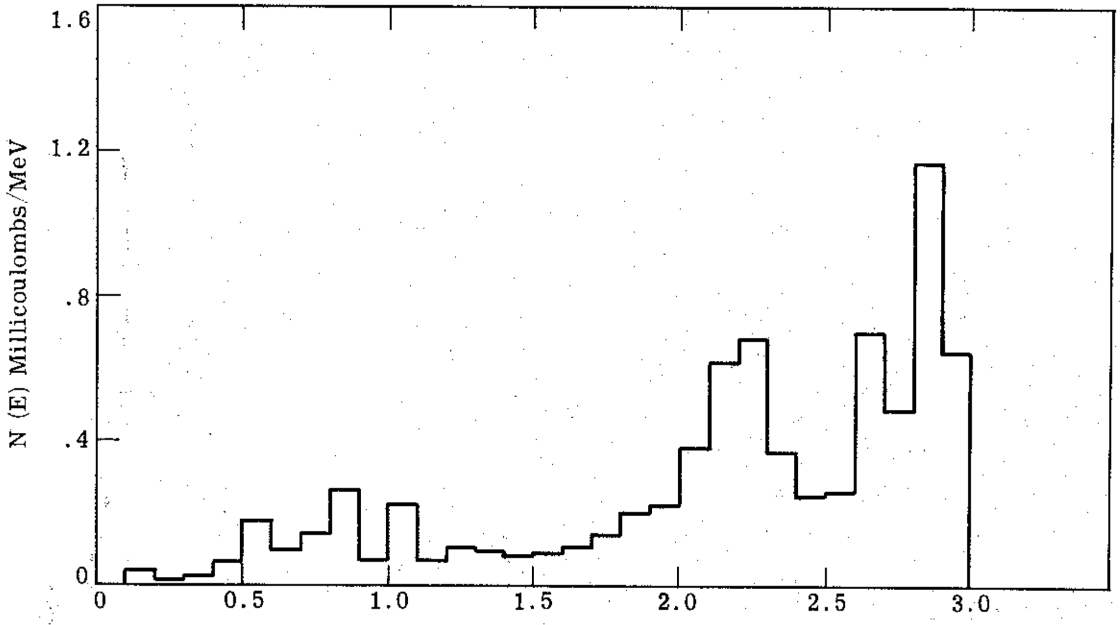

1/8 inch Cathode
2.7 cm Gap, 3 inch Window

Figure 13. Energy Spectrum Derived from Current-Voltage Waveforms

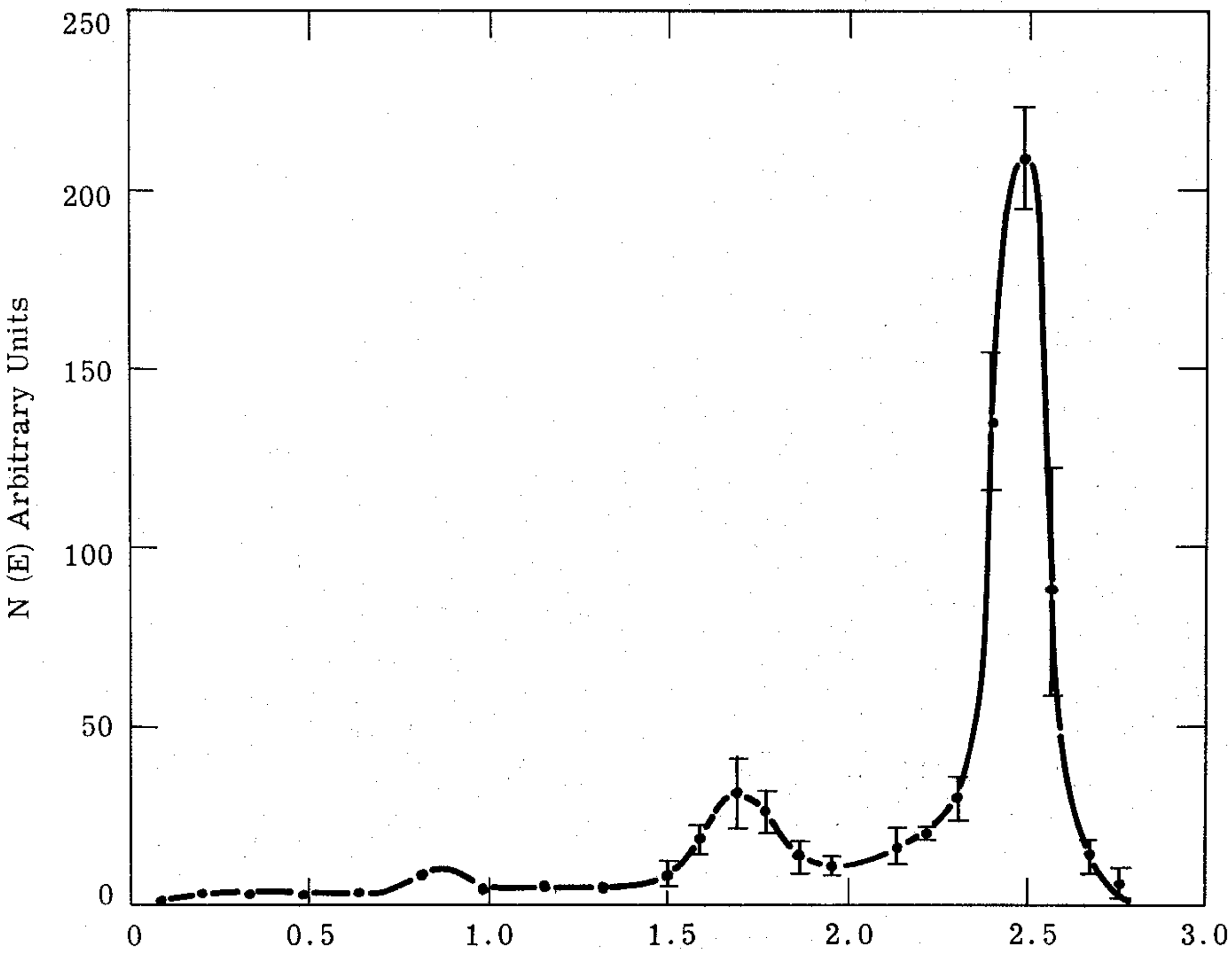

1/8 inch Cathode
2.7 cm Gap, 3 inch Window

Figure 14. Magnetically Analyzed Energy Spectrum

1-4461

seems to increase with cathode voltage for this configuration, as might be expected from a cloud of radially emitted electrons. Here the calibration at 2.23 MeV leads to an energy spectrum that is 10% high at the end point, and a calculated energy delivered that is 20% higher than the calorimeterically measured value.

The characteristics of the $\nu/\gamma = 1.5$ beam studied are shown in Figure 15. This beam was produced by a 2-inch diameter carbon cathode with a gap of .6 cm. The beam has been used extensively and is highly reproducible.

It is seen that $\nu/\gamma$ is increasing for the greater part of the pulse and the impedance is decreasing continuously. The gap closes in $\approx 50$ ns. The discrepancy between the calculated energy produced of 360 J and the calorimeterically observed value of 470 J is attributed to the analytical difficulty of handling the late part of the pulse near closure, where the inductive correction carries over to parts of the voltage pulse which are negative. That is, V is greater than zero but less than LI.

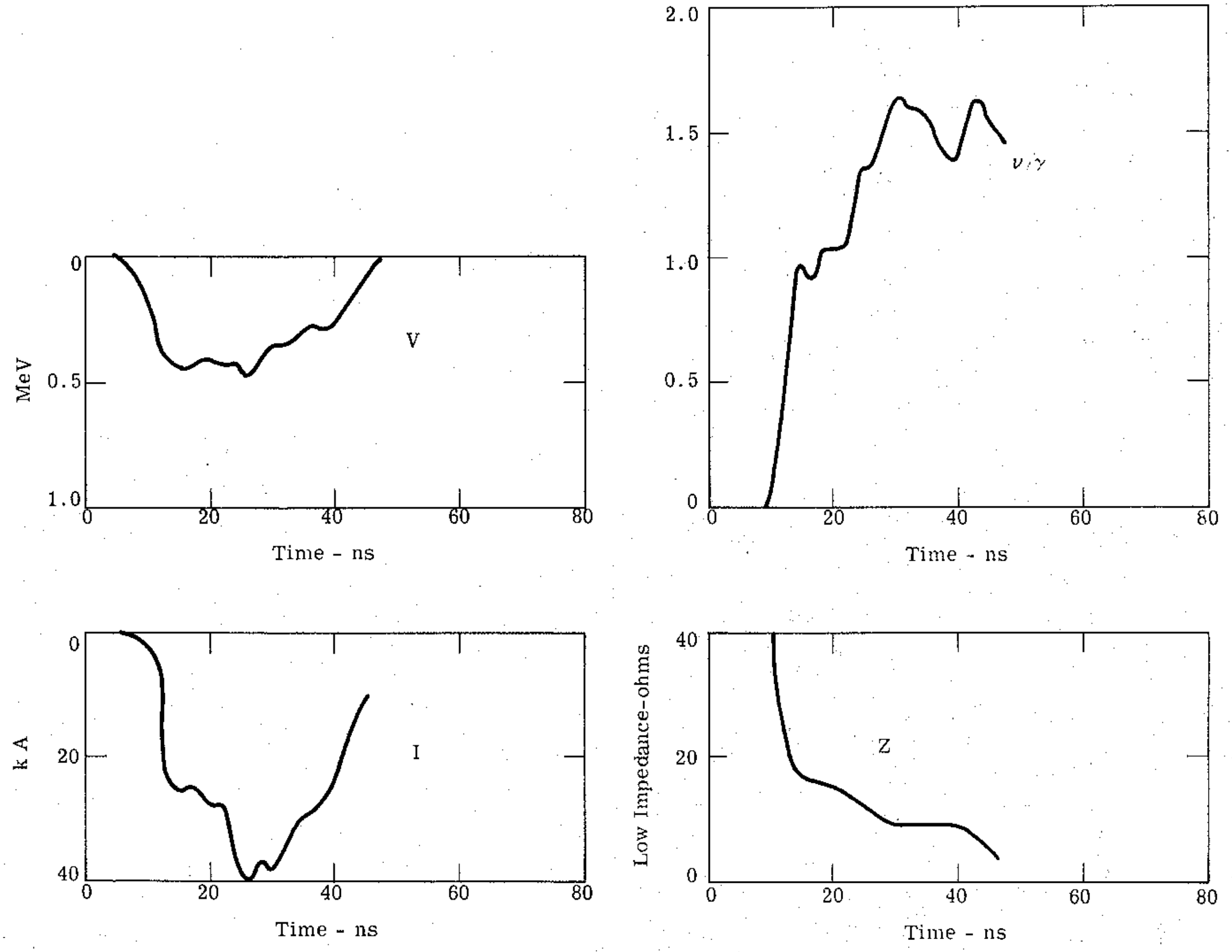

Carbon Cathode
2 inch dia, 0.6 cm Gap
$\int I(t)\,V(t)\,dt = 360\ J$
Calorimeter - 470 J

Figure 15. Field Emission Diode Characteristics

# SECTION 2

# ELECTRON BEAM PROPAGATION

## 2.1 Introduction

In this section data pertaining to the propagation of two beams are presented. The $\nu/\gamma = .5$ beam characterized in Figure 6 and the $\nu/\gamma = 1.5$ beam described in Figure 15 are compared.

A rather complete description of beam behavior at various drift region pressures was given in previous reports of this project. In summary, it was shown in these reports that the beam has four distinct drift conditions:

(a) < .1 Torr
Little charge neutralization
No Volume return current
Beam expands

(b) .1 to .5 Torr
High degree of charge neutralization
$(f > 1 - \beta^2)$
No volume return current
Beam pinches

(c) .5 to 10.0 Torr
High degree of charge neutralization
Large volume return current
Beam drifts under force free conditions in approximately paraxial flow.

(d) > 10. Torr
High degree of charge neutralization
Low volume return current due to collision suppression.
Beam pinches.

In the previous reports cited, the effect of these conditions on beam behavior is discussed. In this report we look at the effect of these conditions on the beam propagation over several meters.

## 2.2 Beam Front Velocity

The beam front time-of-arrival was studied by use of the drift tube return current shunt and with a bremsstrahlung target and scintillator-photodiode detector. Both detectors were read out on fast oscilloscopes and were time referenced to the injection current pulse. In the case of the bremsstrahlung target (Ta) the detector was carefully shielded from window and drift chamber bremsstrahlung. The bremsstrahlung detector is sensitive only to energetic electrons and when compared to the wall current yields rough energy estimates.

Figure 16 shows the beam front arrival time for the $\nu/\gamma = .5$ beam as measured by the return current shunt, referenced to the injection current pulse. The nearest point to the anode that could be monitored was Z = 10 cm, due to the size of the shunt and its mounting hardware. We see from this, and later data, that it takes the beam about two nanoseconds to reach the 10 cm drift distance. The reference current shunt on the field emission tube is five centimeters back from the anode but even taking this into account, the early part of the beam seems to be propagating with a velocity $\beta \approx .2$ to $.3$.

At the lowest pressure examined, .05 Torr, the only part of the beam detected is the part near the axis since the remainder is lost from the expanding beam. At .15 Torr the arrival times is later due to the beam being mostly composed of focused current which cannot be paraxial. At .5 Torr the beam slows down as the front advances. This behavior is reproducible but not understood. At 1.0 Torr the front velocity is identical to .05 Torr as paraxial flow is approached due to plasma return currents. At 10. Torr, the highest beam front velocity occurs again in the pressure regime of volume return currents allowing paraxial flow. Other than the .5 Torr beam, all beam fronts show an increasing velocity as the front advances.

Figures 17 through 22 show the data points that produced the curves shown in Figure 16 plus the data from the bremsstrahlung target measurement of the beam front velocity.

In Figure 17 is shown the .05 Torr data, where the beam front velocity increases from a $\beta = .5$ to $\beta = .8$ (electron velocity at 1.5 MeV is

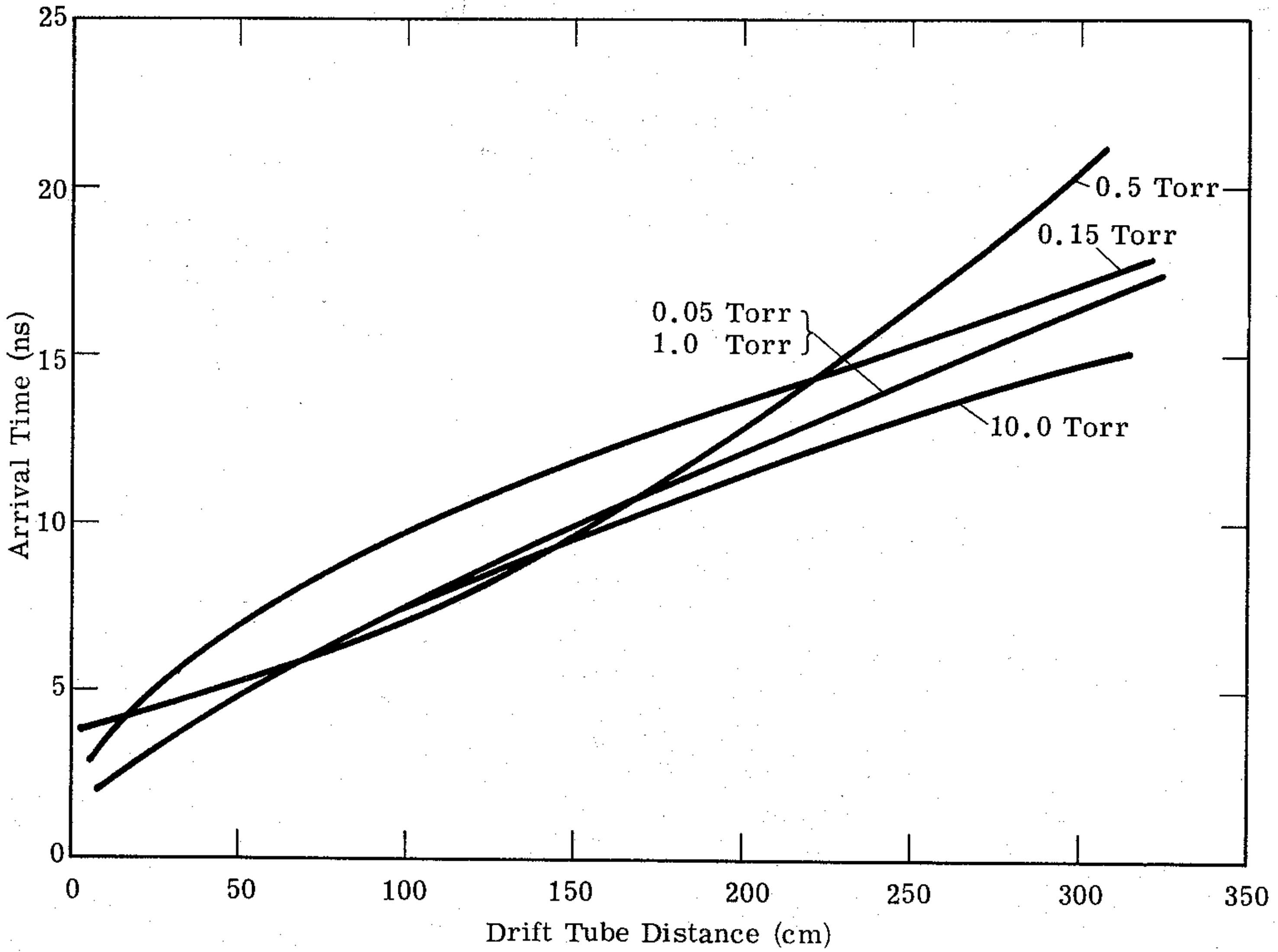

Figure 16. Electron Beam Arrival Time versus Distance
20 Pin Cathode, 2.0 cm. gap.

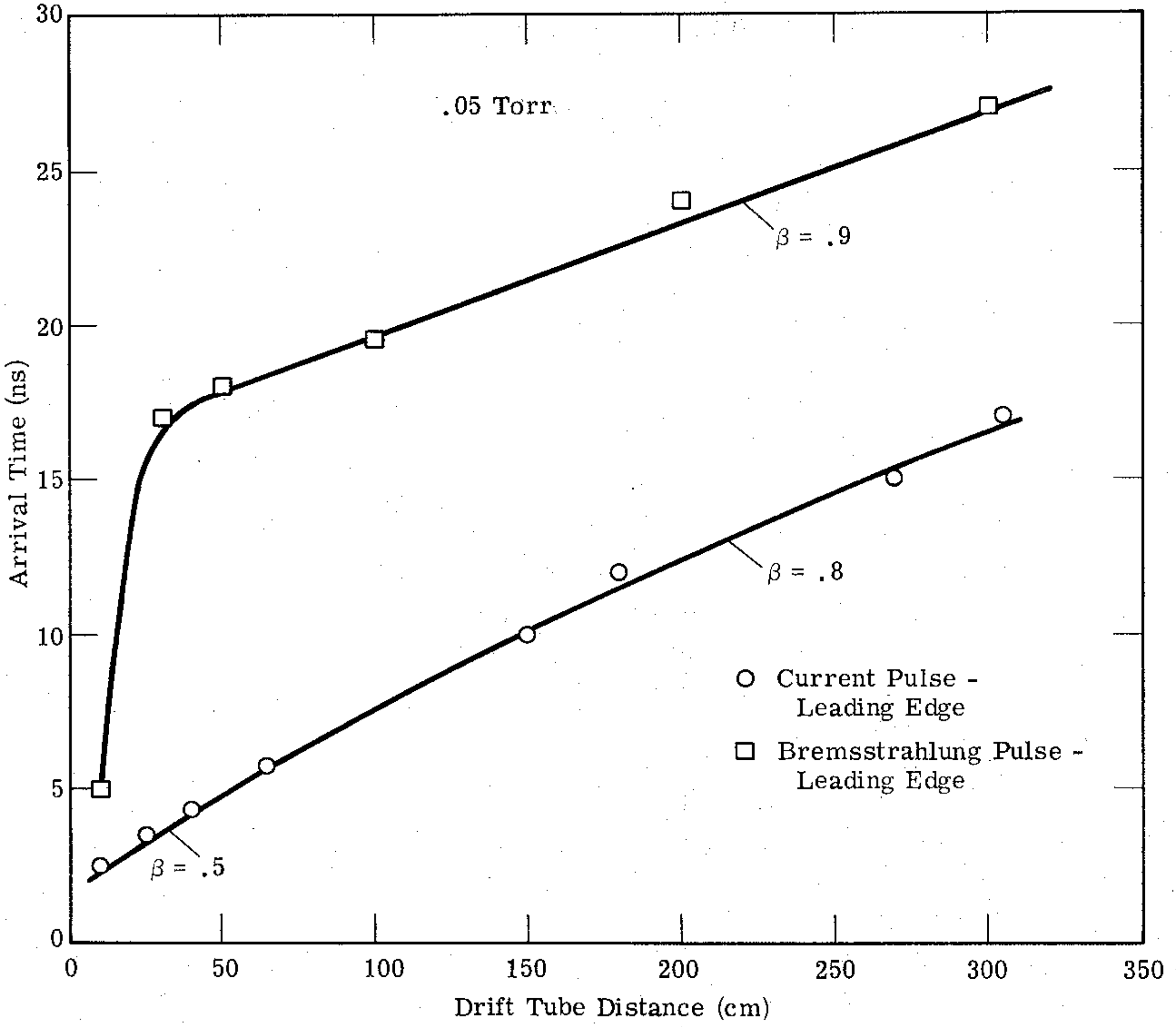

Figure 17. Electron Beam Arrival Time versus Distance
20 Pin Cathode, 2.0 cm Gap.

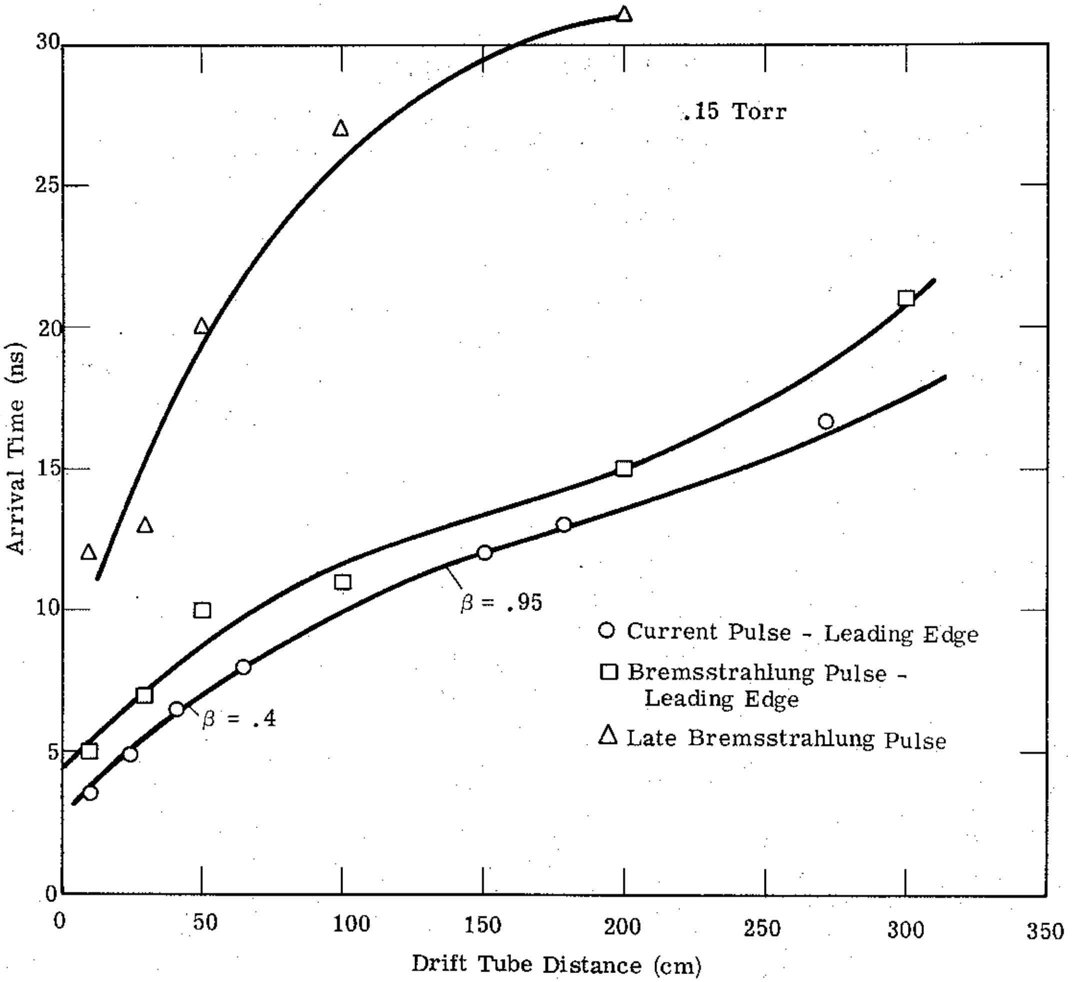

Figure 18. Electron Beam Arrival Time versus Distance 20 Pin Cathode, 2.0 cm. Gap.

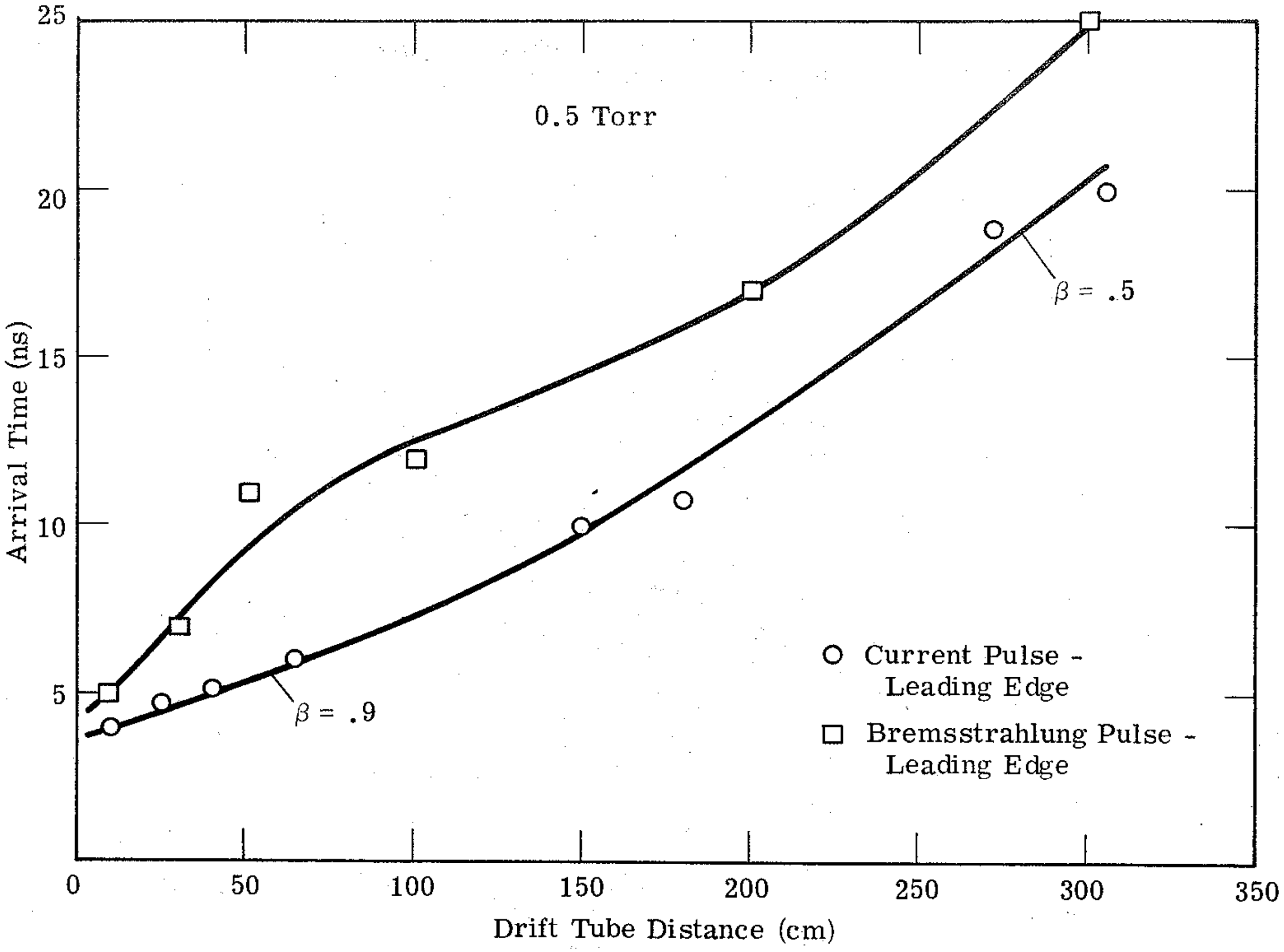

Figure 19. Electron Beam Arrival Time versus Distance
20 Pin Cathode, 2.0 cm. Gap.

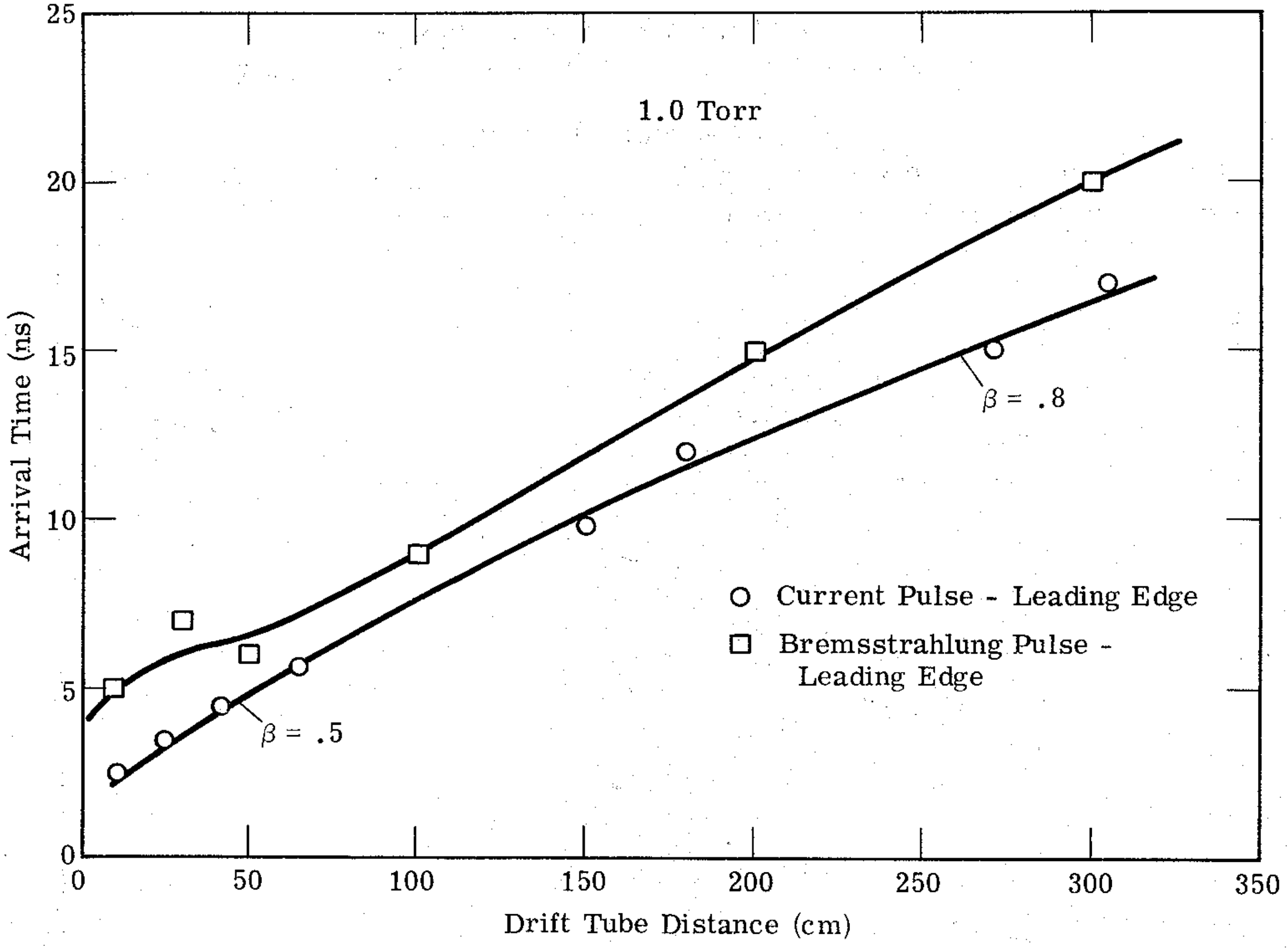

Figure 20. Electron Beam Arrival Time versus Distance 20 Pin Cathode, 2.0 cm. Gap.

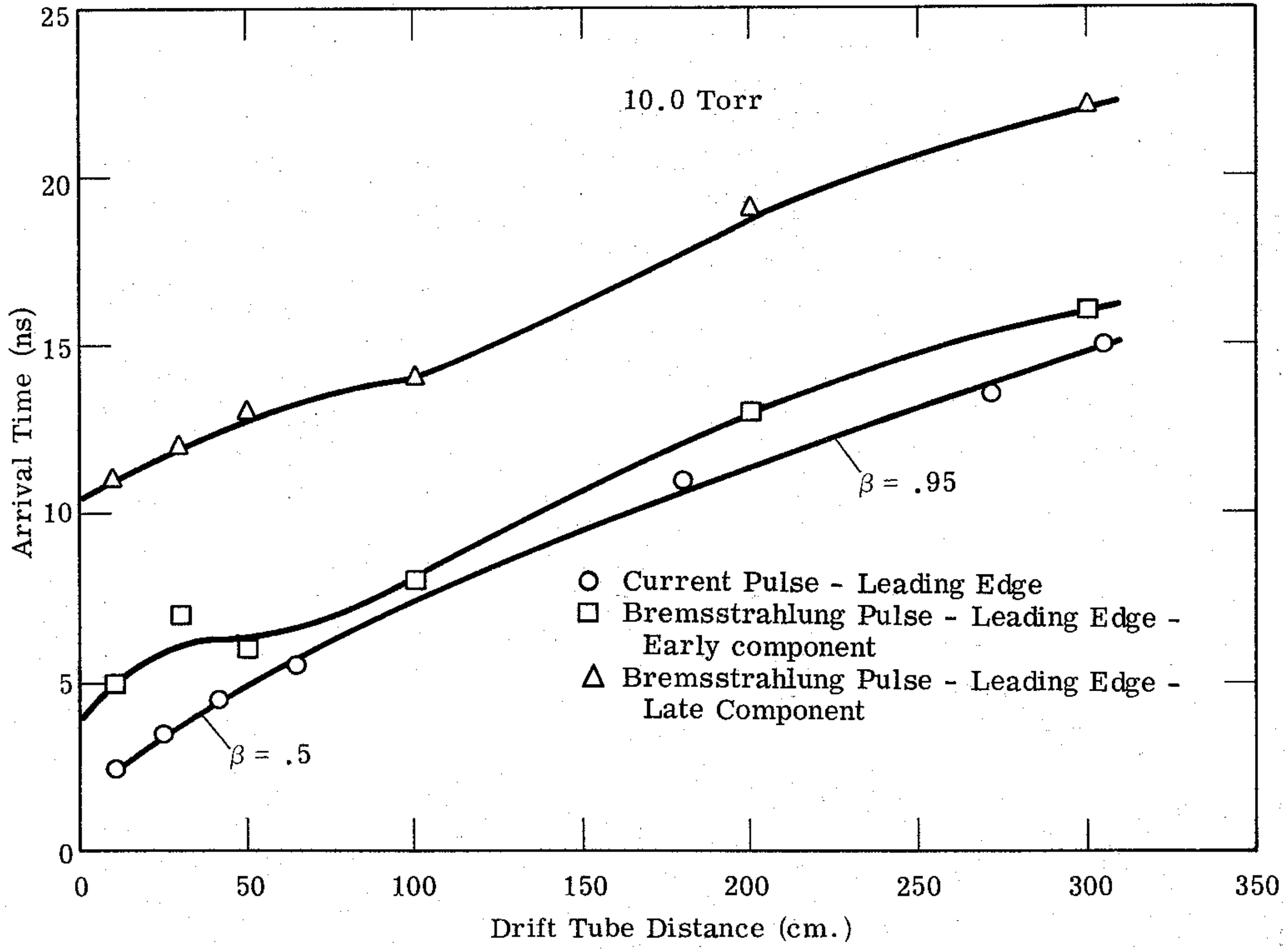

Figure 21. Electron Beam Arrival Time versus Distance 20 Pin Cathode, 2.0 cm Gap.

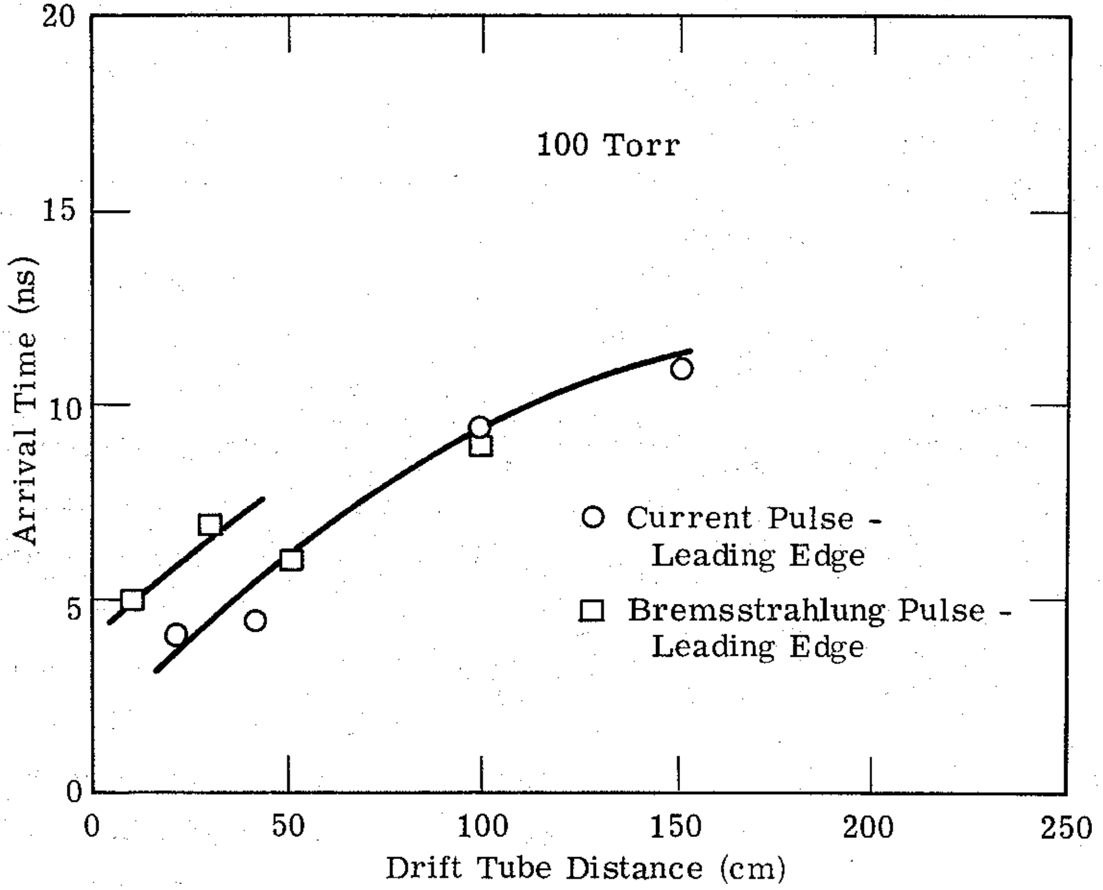

Figure 22. Electron Beam Arrival Time versus Distance 20 Pin Cathode, 2.0 cm. Gap.

$\beta = .96$). The bremsstrahlung signal is greatly delayed in time but advances at about the same rate as the current front. The ten nanosecond time delay is not understood.

In Figure 18 the .15 Torr data are shown. The current front goes from $\beta = .4$ to $\beta \approx .95$. The early bremsstrahlung trace arrival time parallels the current front arrival time with a two nanosecond delay, which is explainable from the bremsstrahlung dependence on electron energy. The late bremsstrahlung pulse shown was quite distinguishable from the early pulse, and is due to the focusing of the off-axis components of the beam. The time delay of ≈ 10 ns is about right for a neutralization time.

Figure 19 shows the .5 Torr beam which is the only one studied which slows down as it advances. The front velocity goes from $\beta = .9$ to $\beta = .5$. The bremsstrahlung data are in reasonable agreement.

Figure 20 shows the 1. Torr beam, with increasing velocity from $\beta = .5$ to $\beta = .8$. Figure 21 shows the 10 Torr data where a late bremsstrahlung component delayed by 5 ns appears, presumably due to the reappearance of focused components.

Figure 22 shows the beam front at 100 Torr where it does not propagate past 150 cm and the bremsstrahlung signal is not detectable beyond 30 cm.

Figure 23 shows the beam front data for the 400 keV beam with $\nu/\gamma = 1.5$. Here the 1.0 Torr beam shows evidence of paraxial flow. All pressures show an initial time delay of 5 ns past the injection current pulse. Both .5 Torr and 5.0 Torr show a slowing down as the beam front advances and all other pressures show an acceleration.

All beams showed a similar behavior in hydrogen, except all pressures are increased due to the smaller ionization cross section.

## 2.3 Beam Energy Transport

### 2.3.1 Calorimeter Studies

In the last report the correlation of net beam current with beam pinching was covered. The net current versus pressure data shown in Figure 24

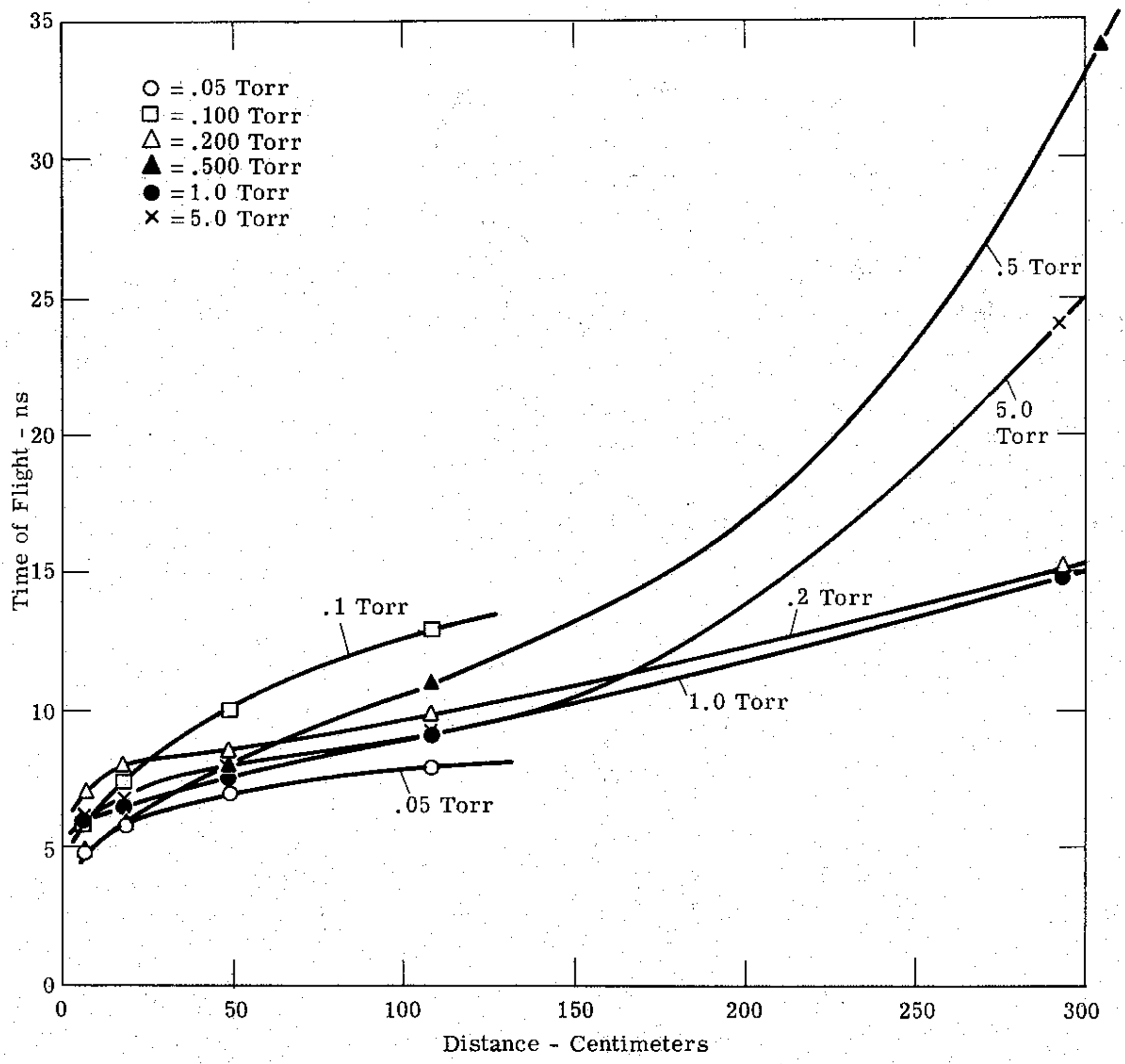

Figure 23. Electron Beam Arrival Time versus Distance 2-inch Diameter Carbon Cathode 0.6 cm Gap.

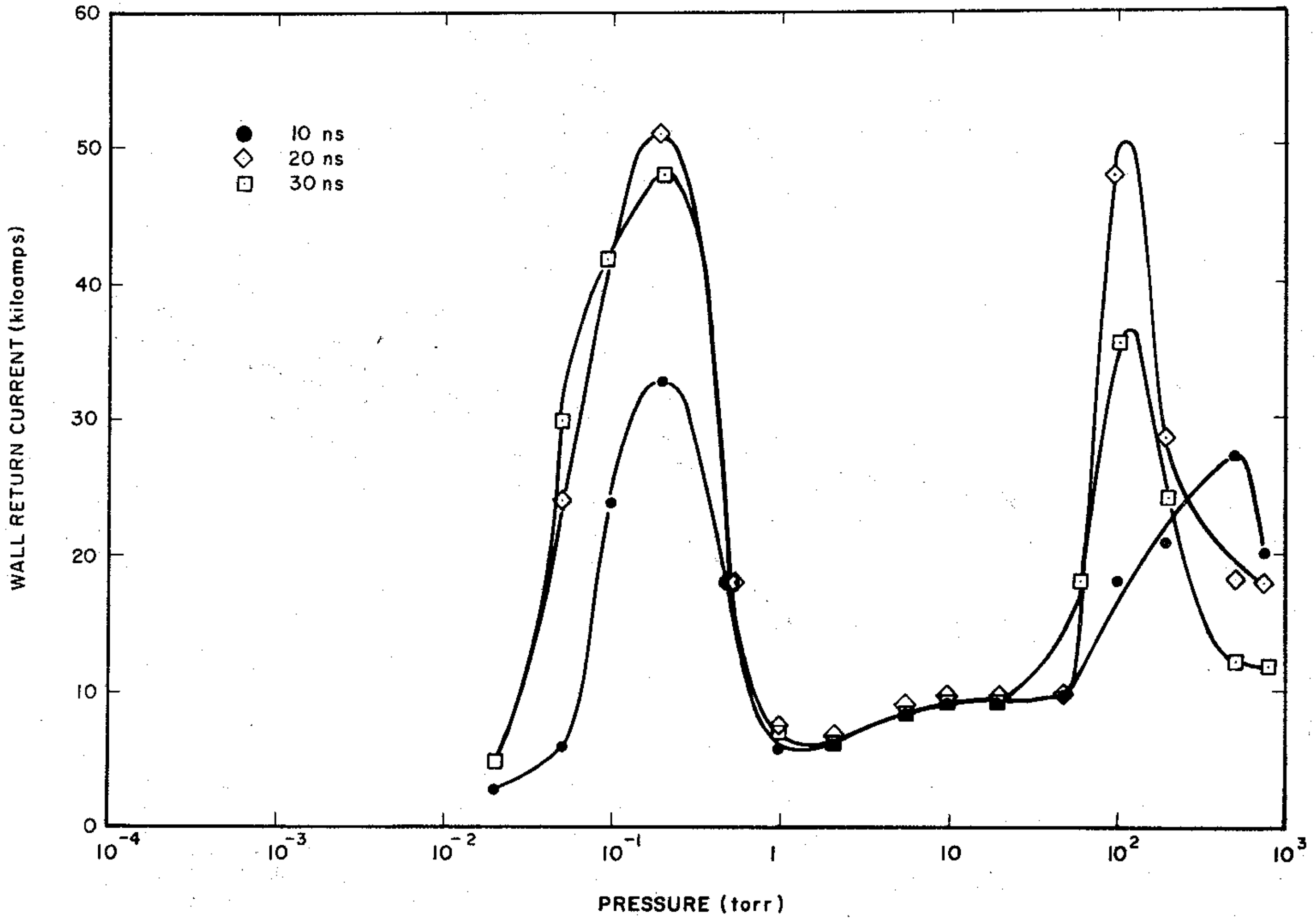

Figure 24. Wall Current as a Function of Drift Tube Pressure (Air)

was presented. In Figure 25 is shown the beam energy fluence at 20 cm as a function of pressure for this $\nu/\gamma$ = .5 beam. The focusing characteristics are the same as for the high impedance beam discussed in all earlier reports.

The total energy transport over large distances was measured with a large calorimeter which intercepted the entire beam. The results of this measurement are shown in Figure 26. As expected, we see the highest energy transport is under the approximately paraxial flow conditions obtained at a few Torr pressure. In this case the best energy transport, over 3 meters is at 2 Torr. At this pressure, 75% of the beam energy is transported over the 3 meters.

In Figure 27 are shown similar data for hydrogen. The energy transport at 3 meters is slightly less than is the case in air. The optimum pressure is twice as high, 4 Torr rather than 2 Torr, as would be expected due to the smaller ionization cross section.

The 400 keV beam with $\nu/\gamma$ = 1.5 was propagated with a high degree of reproducibility. The highest energy fluence was found at 3 cm as shown in Figure 28. The pressure dependence is shown in Figure 29, where the striking feature is that for these high $\nu/\gamma$ beams even the highest energy fluence is in the one Torr regime as opposed to tenth Torr for lower $\nu/\gamma$ beams.

In Figure 30 is shown the total energy transport for this beam, and we find better than 80% energy transport for this $\nu/\gamma$ = 1.5 beam at one meter and greater than 60% at 3 meters. Again the optimum pressure is one Torr and, as is obvious, must be carefully controlled for optimum energy transport. The reproducibility in voltage and current for this beam is ± 5% which makes these studies possible. To obtain this degree of reproducibility the deflection of the window even at these low drift region pressures must be measured and the gap set accordingly. This is the most critical parameter, since the machine parameters are easily reproduced accurately. These data are a striking demonstration of the usefulness of dc machines for these studies.

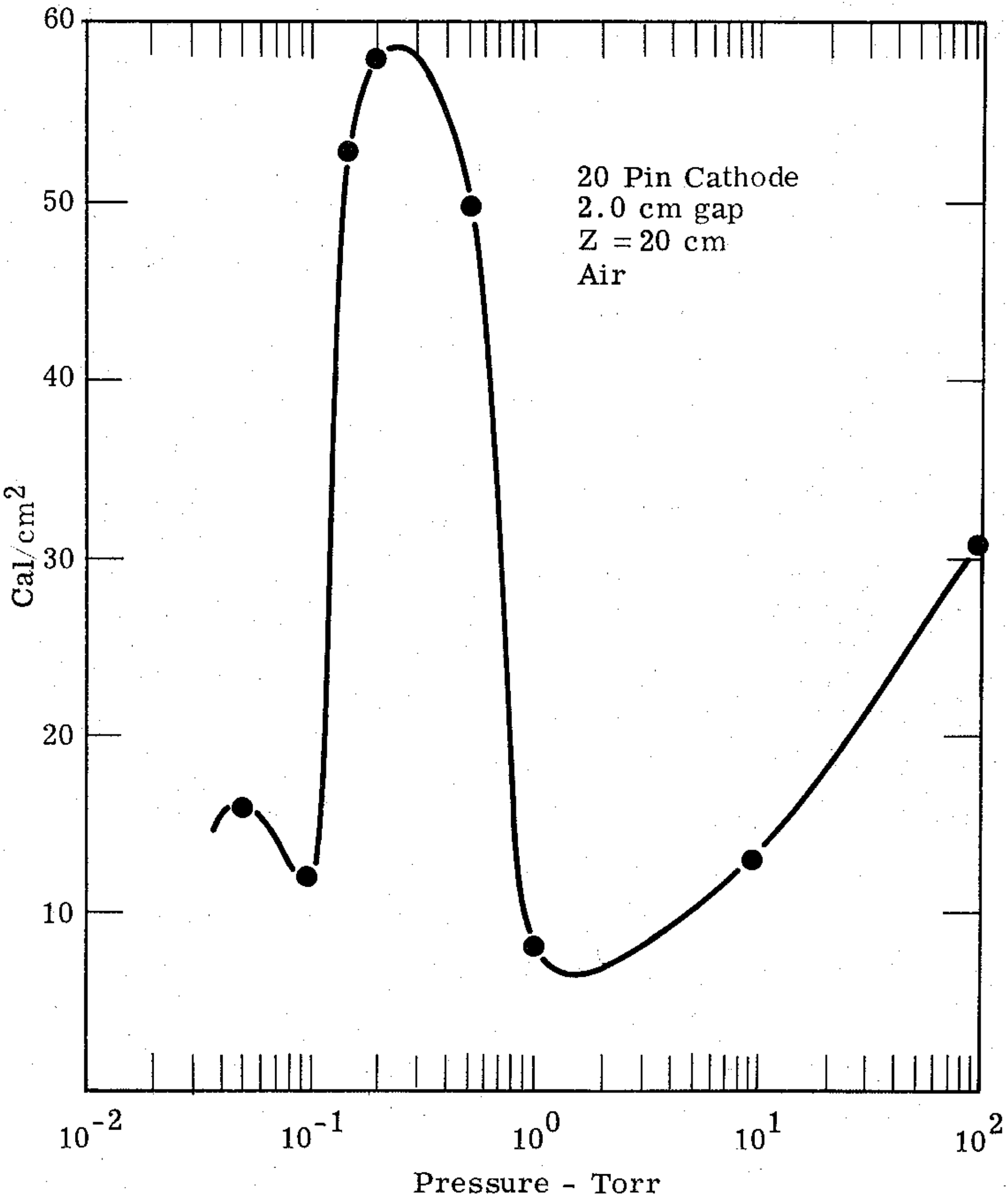

Figure 25. Beam Energy Fluence

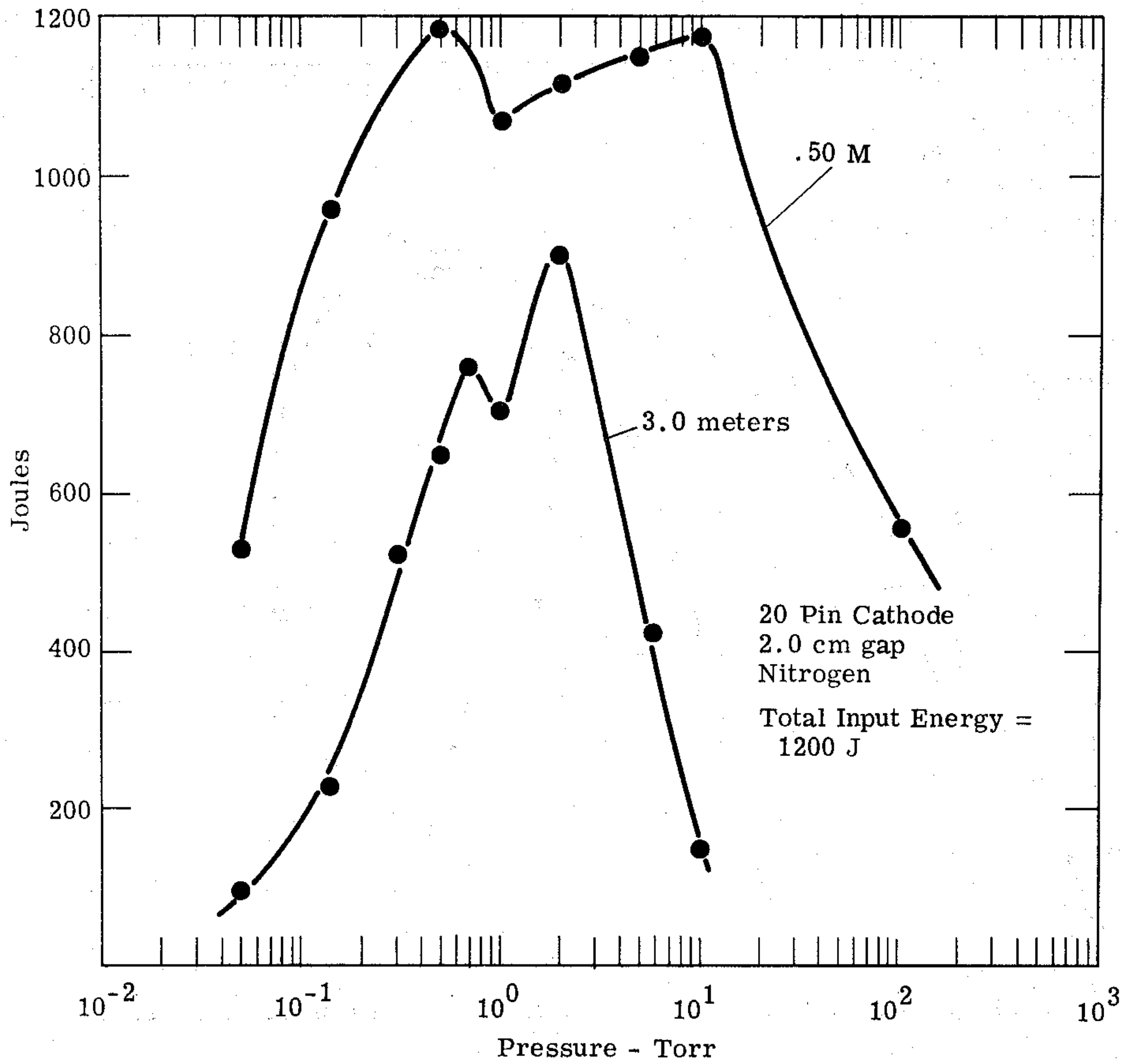

Figure 26. Total Transmitted Beam Energy.

1-4472

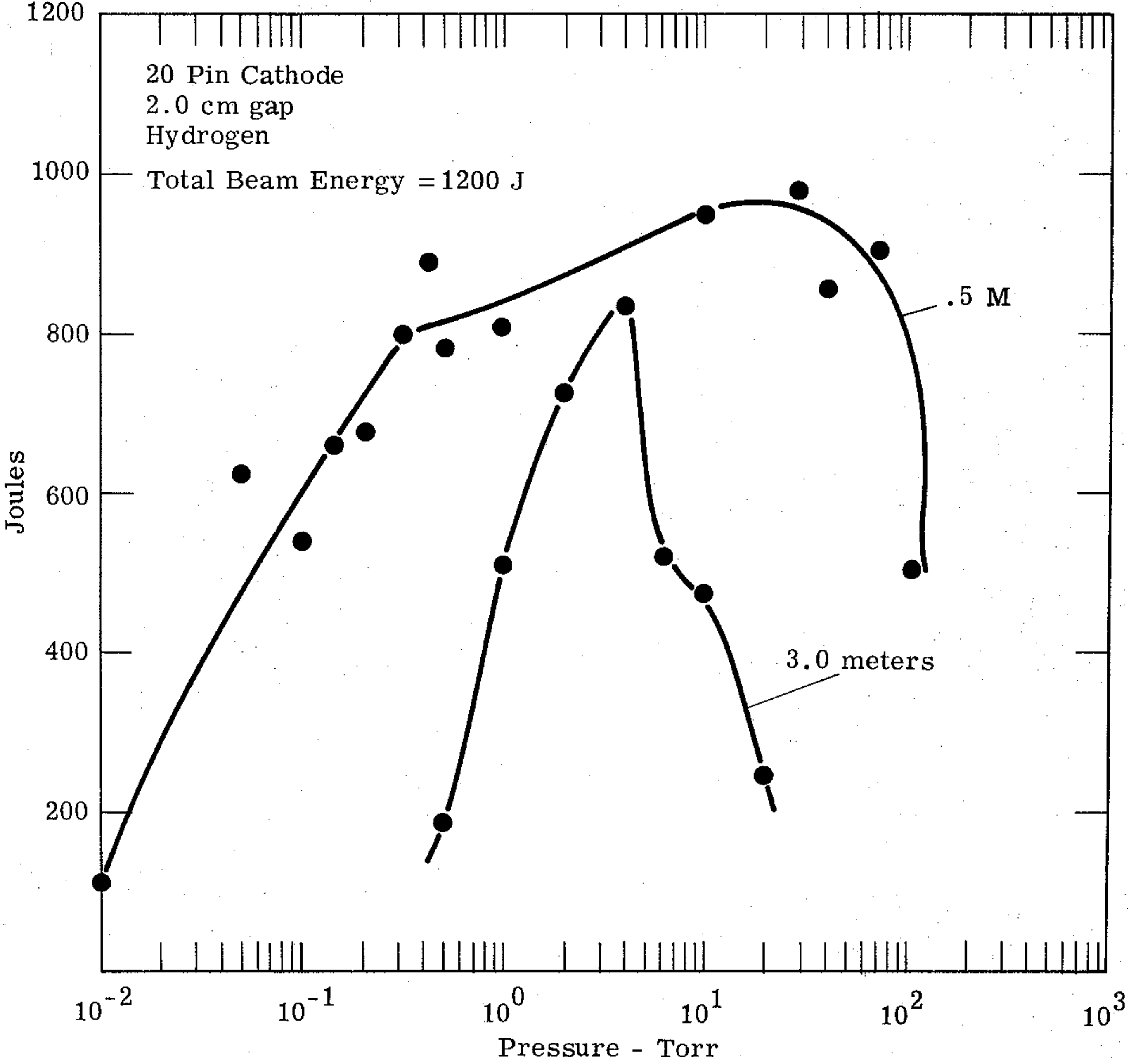

Figure 27. Total Transmitted Beam Energy.

1-4473

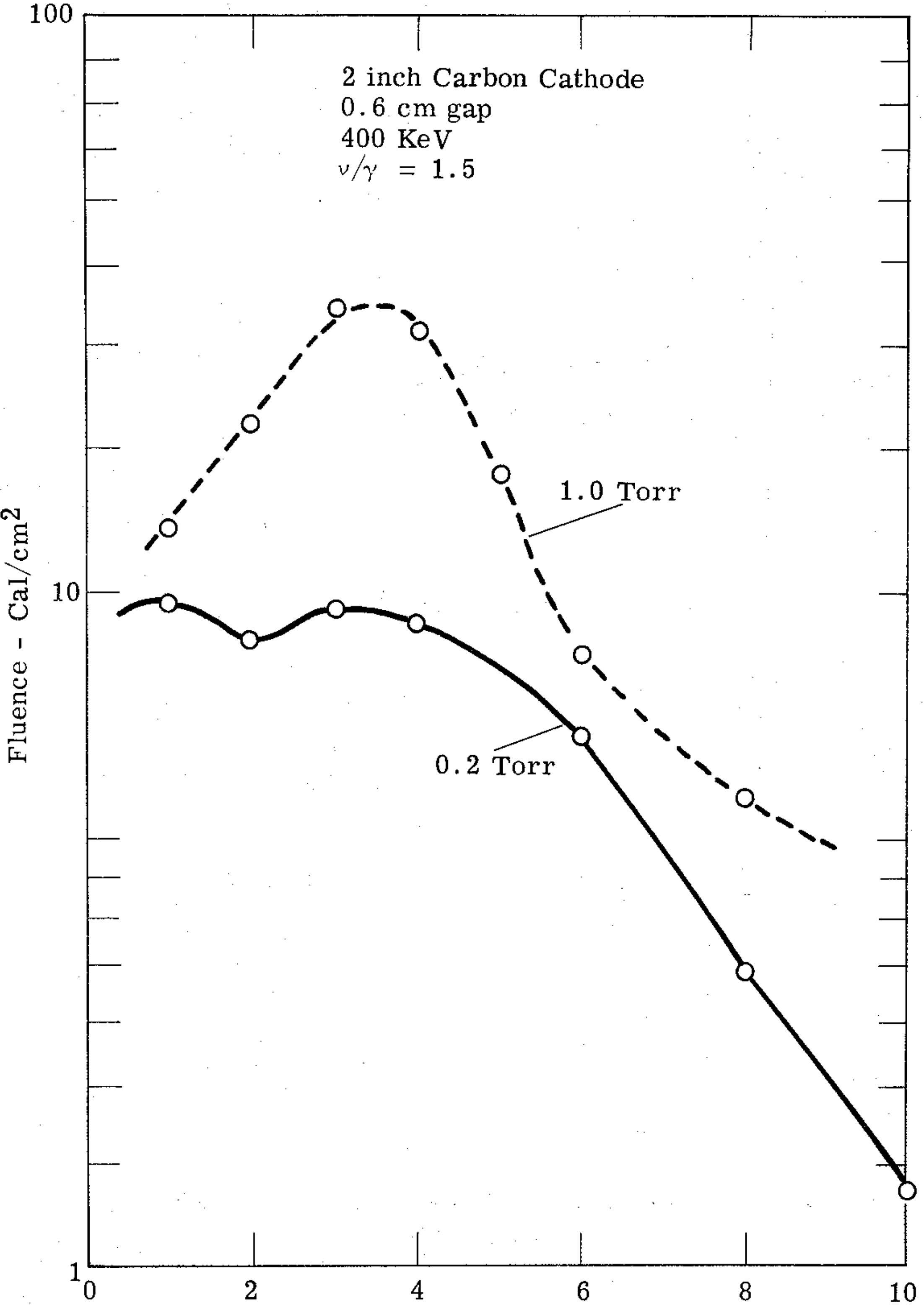

Figure 28. Beam Energy Fluence versus Distance

1-4474

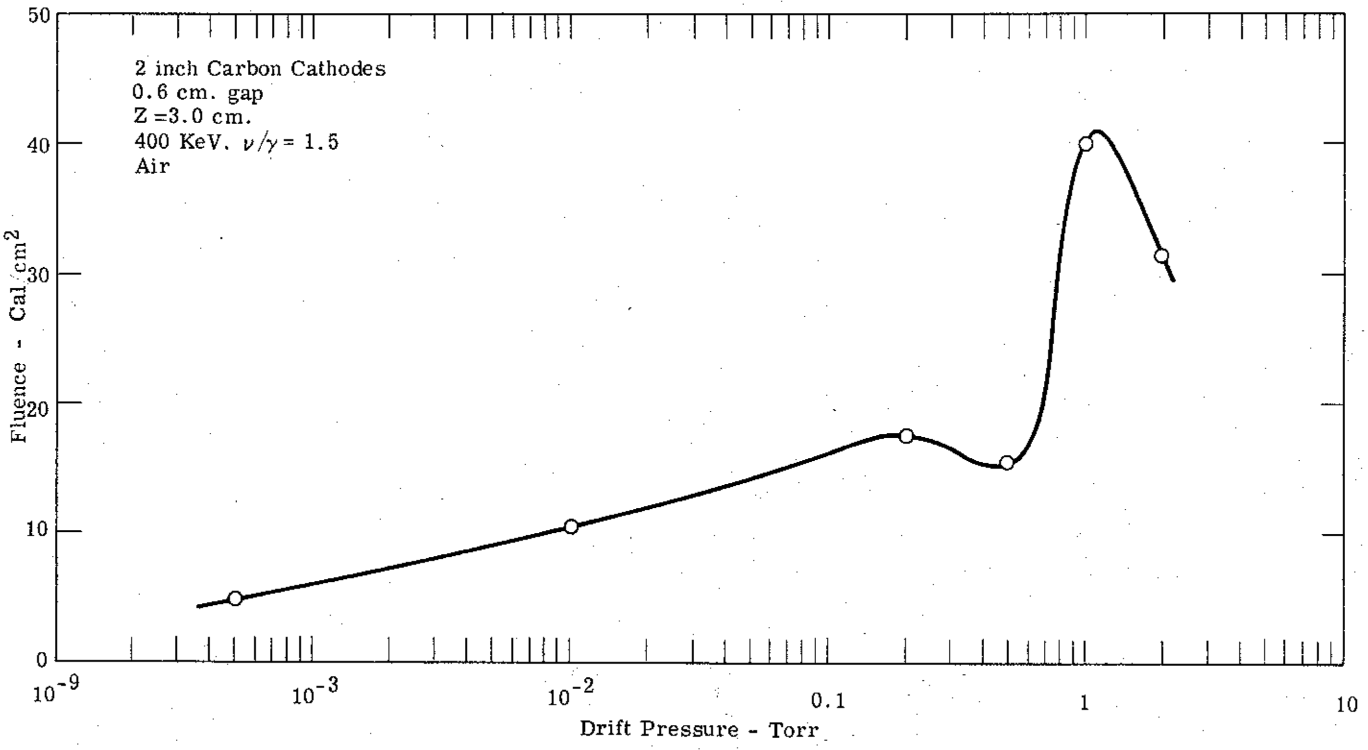

Figure 29. Beam Energy Fluence versus Pressure.

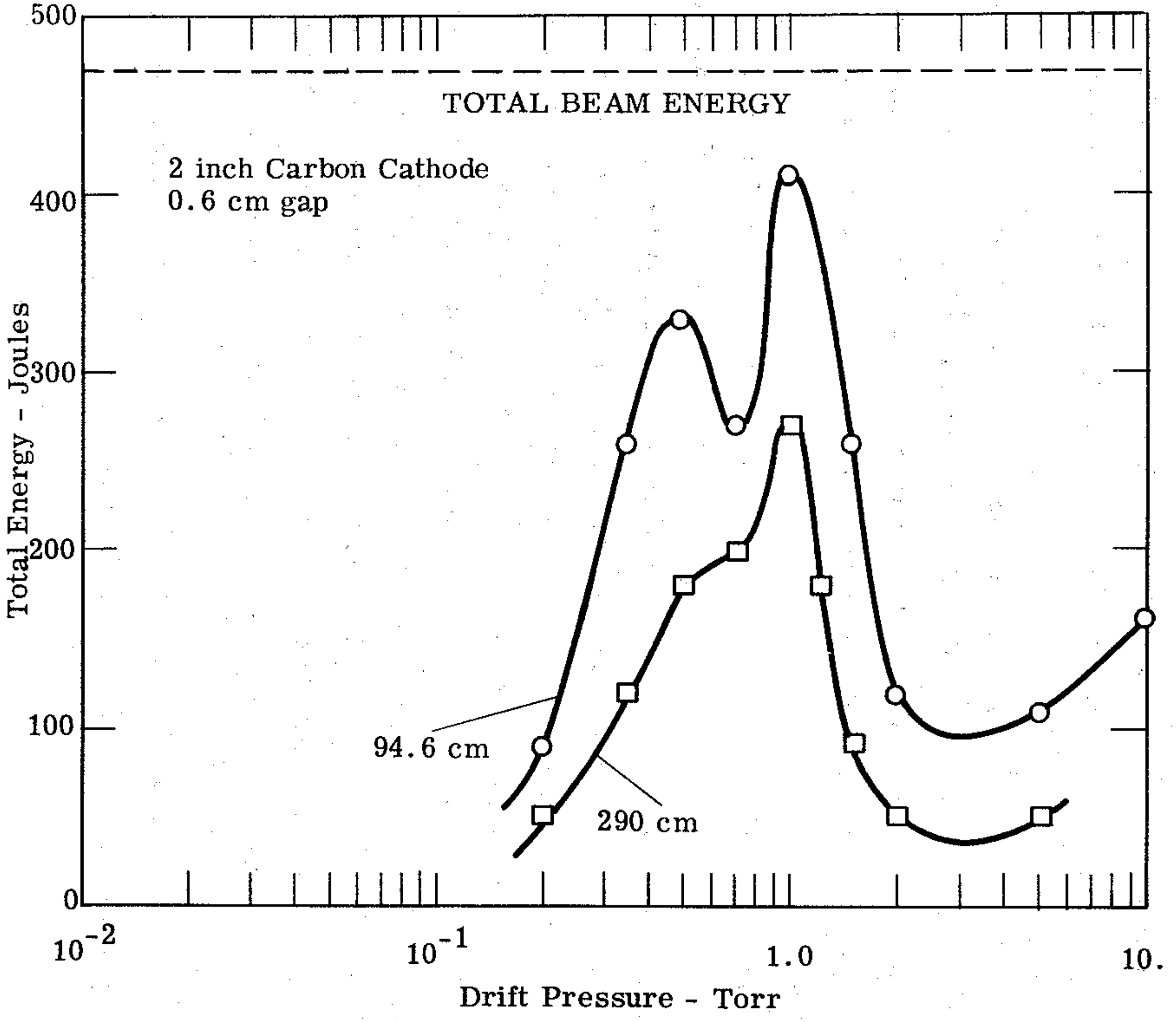

Figure 30. Total Transmitted Beam Energy

### 2.3.2 Spectrometer Studies

With the beam focusing behavior and total energy transport now understood, there remains the question of energy spectrum change under drifiting conditions. This is an important point in simulation work and of some import in CASINO applications. In this series of measurements the 180° magnetic spectrometer was used to measure the beam energy spectrum as a function of pressure and distance.

In Figure 31 is shown the spectrum of the beam from the 20 pin cathode measured at 20 cm in relatively good vacuum ($3 \times 10^{-4}$ Torr). Also shown is the same measurement at 50 cm. The obvious result is that the energy spectrum is the same but the current is decreased as would be expected from a spreading beam.

In Figure 32 is shown a set of spectral measurements for the pinched beam at .2 Torr. We see evidence of spectral degradation even at 20 cm and a lowering of the average energy and the current as the beam advances downstream. The vertical axis is in arbitrary but constant units so the lowering of the amplitude of N(e) corresponds to a decrease in current density into the spectrometer.

In Figure 33 we show the spectrum of the beam drifting under the paraxial, one Torr condition. It is seen that the energy spectrum is remarkably well preserved and the current density is only slightly decreased. This, of course, is in agreement with the calorimeter findings. This measurement is of utmost importance to the application of beams to simulation problems. Again the importance of reproducibility to understanding beam phenomenology is demonstrated.

In Figure 34 we show the 100 Torr condition, where there is rapid spectral degradation and loss of current density.

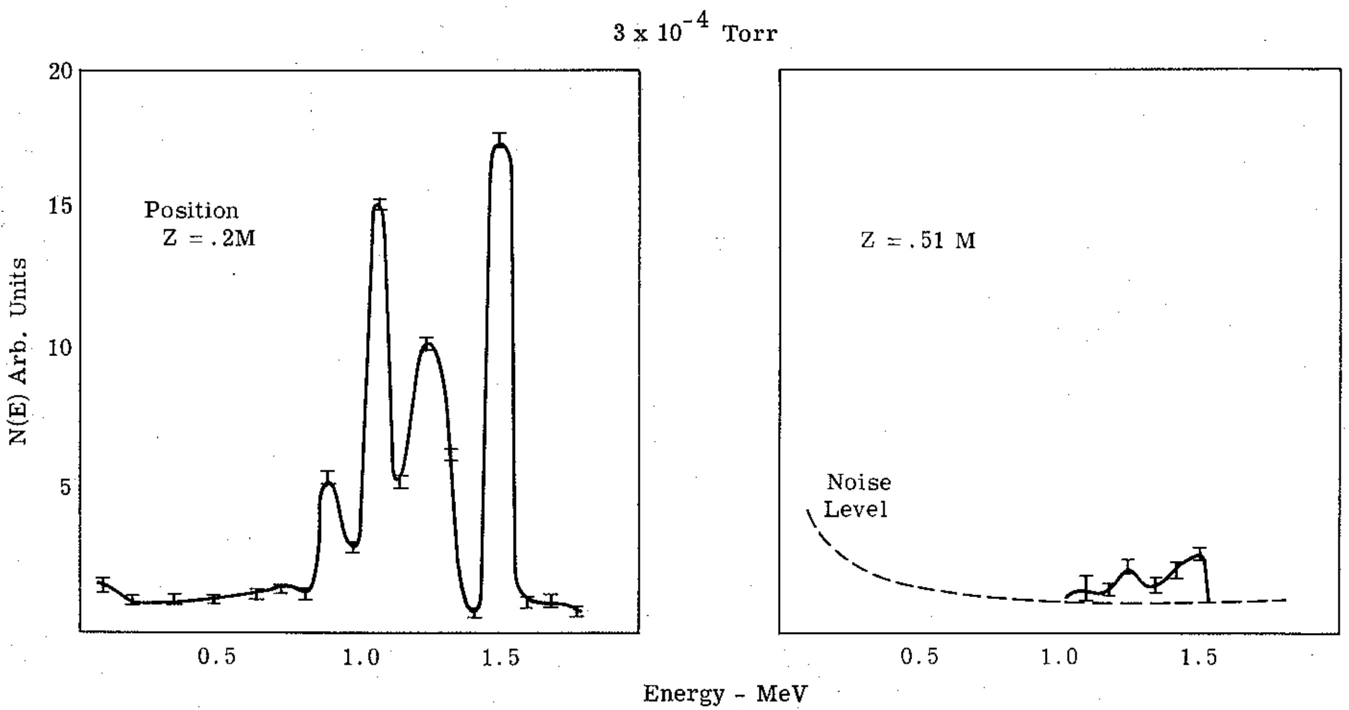

Figure 31. Electron Energy Spectrum

20 pin cathode

2.0 cm gap

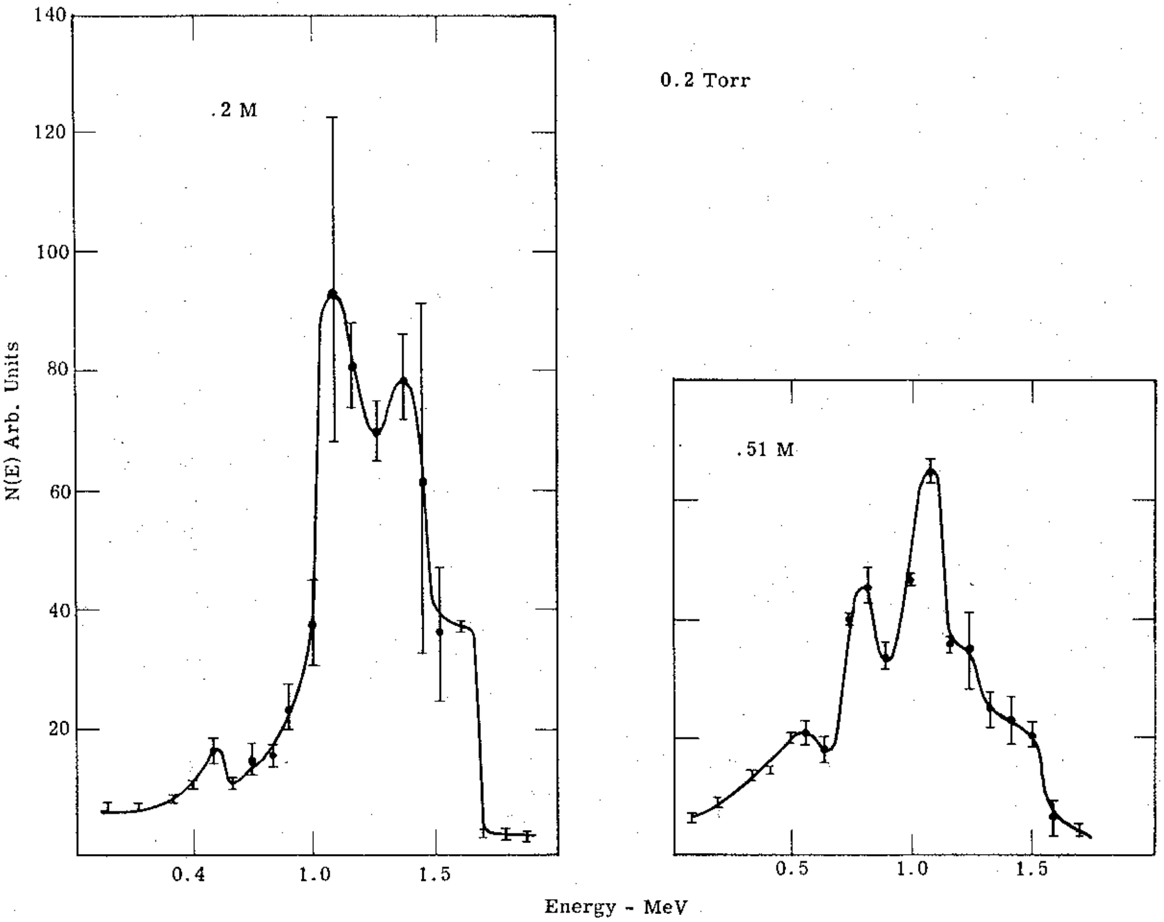

Figure 32. Electron Energy Spectrum
20 Pin Cathode
2.0 cm gap

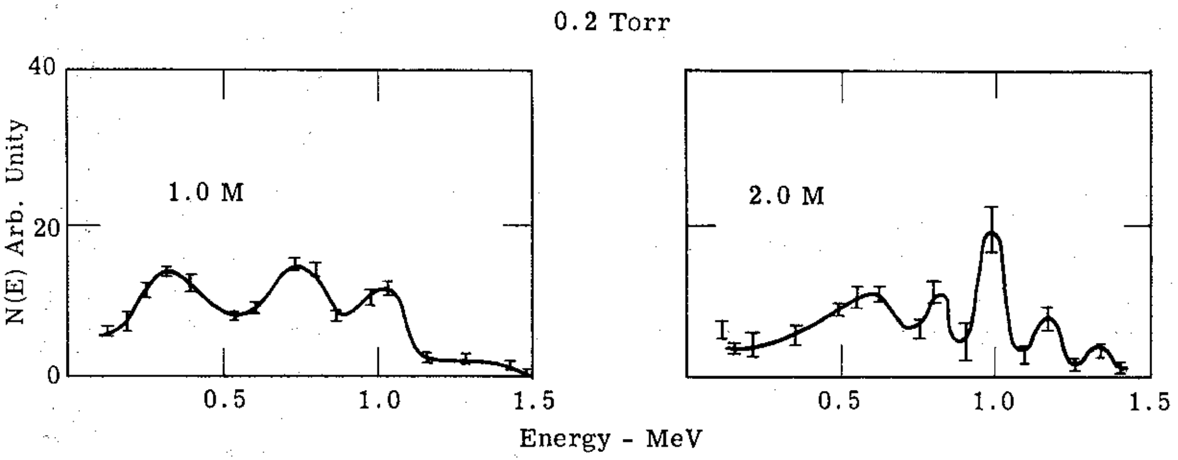

Figure 32 - Continued

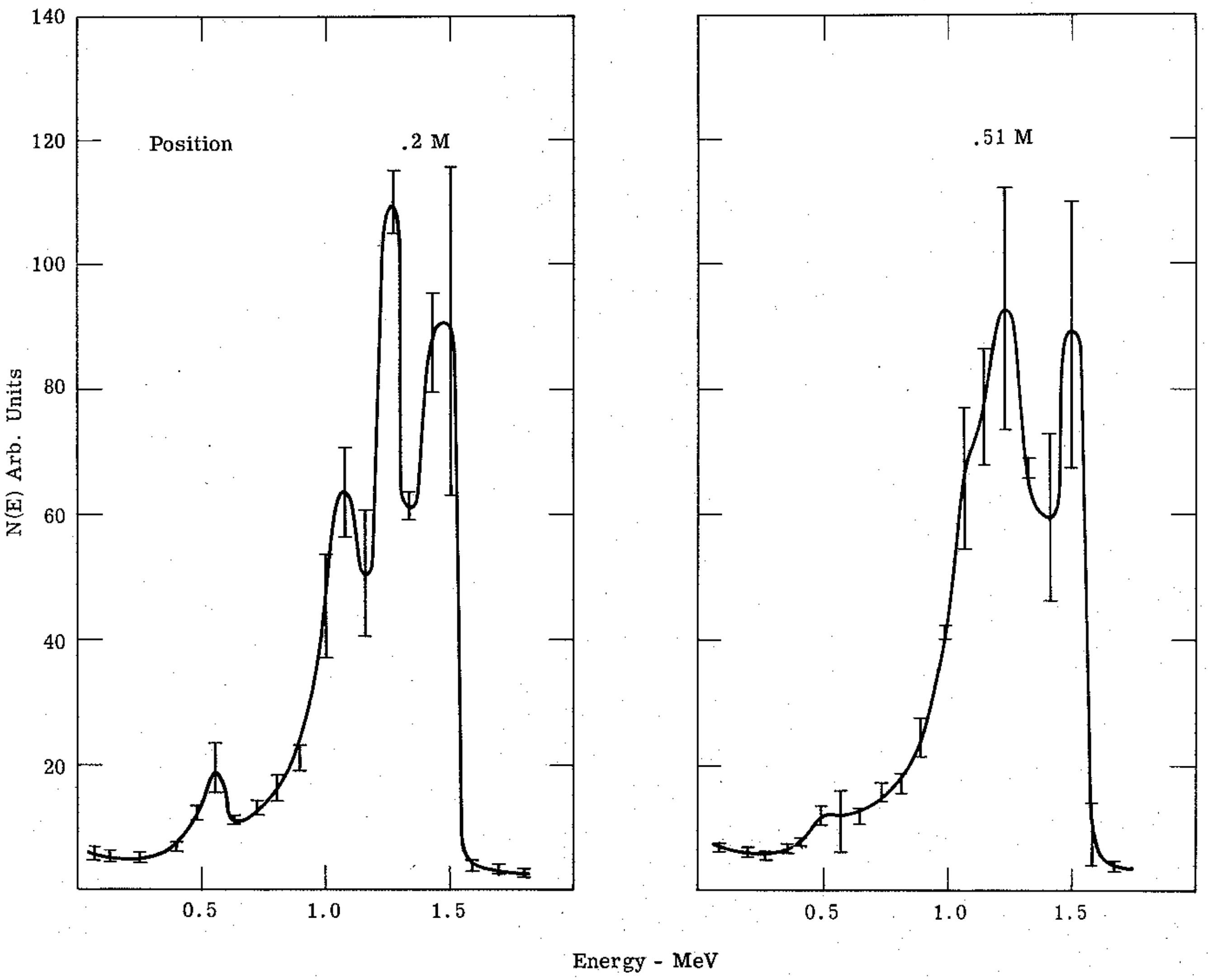

Figure 33. Electron Energy Spectrum - 20 pin Cathode, 2 cm. Gap for Four Longitudinal Positions at P = 1 Torr of Nitrogen.

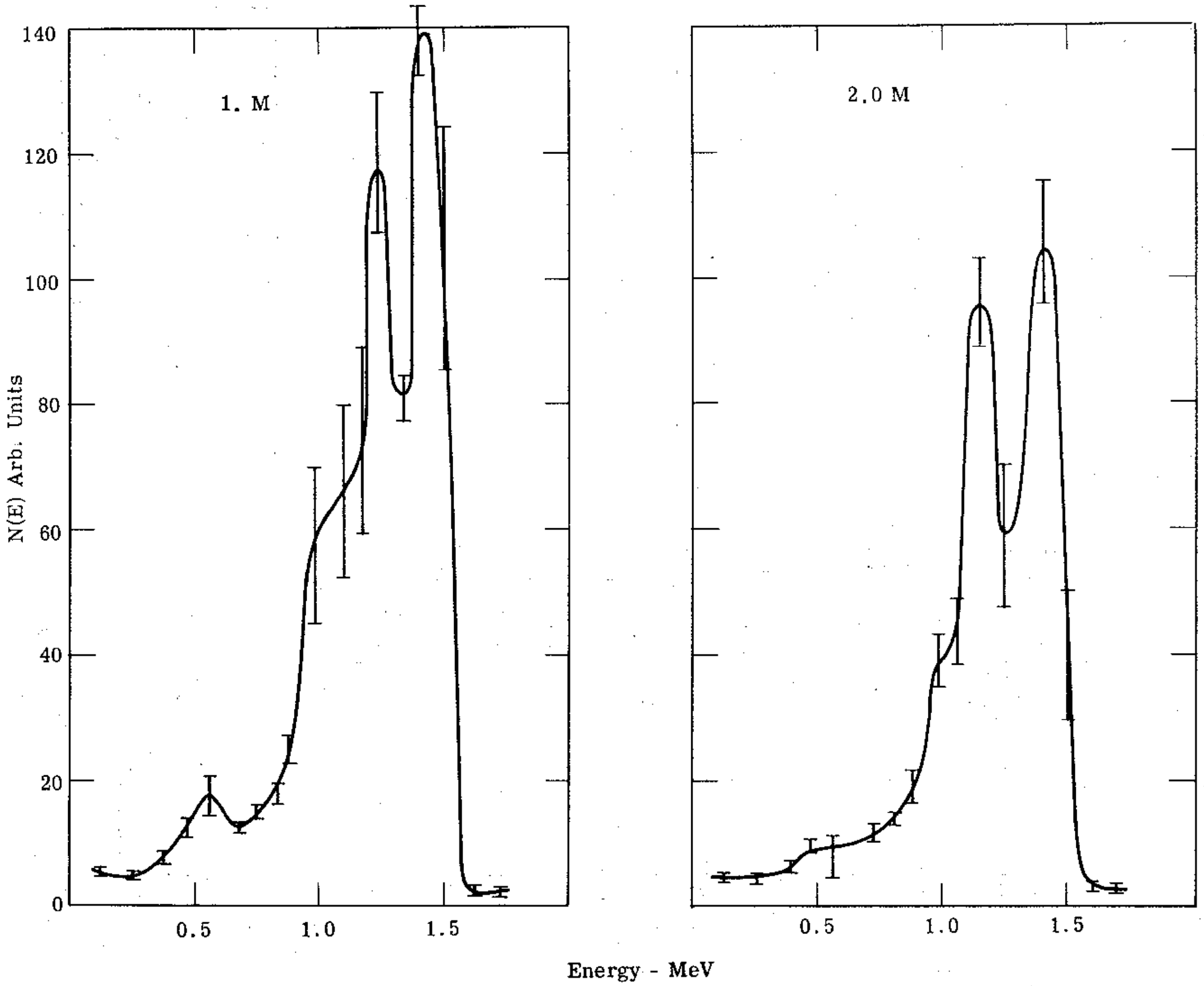

Figure 33. Continued

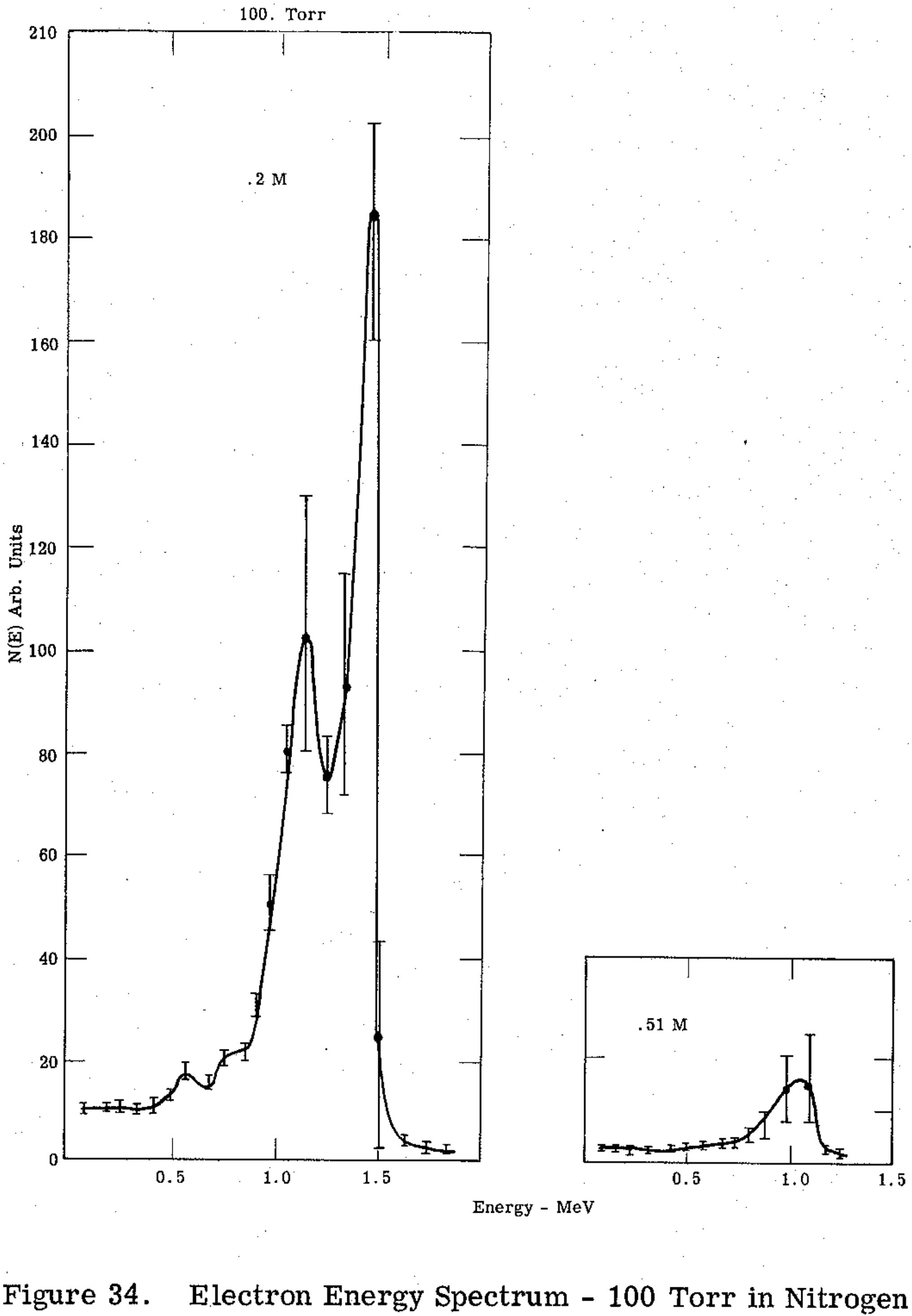

Figure 34. Electron Energy Spectrum - 100 Torr in Nitrogen 20 Pin Cathode, 2 cm gap - at two Longitudinal Positions

1-4480

# SECTION 3

# LASER INTERFEROMETRY

## 3.1 Introduction

Under previous phases of this contract(1) spectroscopic studies of the light emitted from relativistic electron beam produced plasmas showed that energetic, non-equilibrium plasmas could be formed under some conditions. The appearance of spectral lines of O VIII and N VII and the temporary darkening of nearly all transitions shortly after the electron beam passage indicated that electron densities in the region of $10^{16}$ electrons $cm^{-3}$ were being produced.

In order to make absolute measurements of these plasmas and to observe their production by the electron beam, a laser illuminated multiple pass Mach Zehnder interferometer was designed and built. An experimental program was carried out using two IPC accelerators. A helium-neon laser coupled with photomultiplier detectors and a Q-switched ruby laser recording on Polaroid film were used in separate parts of the study. The resulting data gives a time and spatially resolved picture of the formation and expansion of plasmas formed by pulsed electron beams.

Densities of $10^{17}$ electron $cm^{-3}$ were observed. Plasmas were seen during the primary electron pulse (in helium) and were detected as late a 11 microseconds later (in air and argon). Both axially peaked and hollow electron beam distributions were observed along with evidences of plasma confinement and compression.

Laser illuminated interferometry has been successfully used in studies of plasma produced by shock tubes(2), pinches(3), laser sparks(4) and the ionization of solid material(5) by lasers. These techniques were extended in order to perform measurements on relativistic electron beam produced plasmas. The rapid formation and short lifetimes of these plasmas limit the wavelengths that can be used to the visible. Only in that region are the necessary fast photoelectric detectors and sensitive photographic films available.

These combined with stable and powerful lasers make visible light interferometry a useful tool for the study of short lived dense plasmas.

## 3.2 Theory

In the presence of a plasma where the angular frequency of the light ($\omega$) much exceeds the plasma angular frequency ($\omega_p$) the electromagnetic wave equations of motion reduce to:[(6)]

$$\frac{\partial^2 E_y}{\partial x^2} - \frac{4\pi N_e e^2 E_y}{m_e c^2} = \frac{1}{c^2} \frac{\partial^2 E_y}{\partial t^2} \tag{1}$$

for a wave in which $E_y$ propagates along the X axis. For a solution of the form

$$\exp i (kx + \omega t) \tag{2}$$

the dispersion relation becomes

$$k^2 = \frac{c^2}{1 - \omega_p^2/\omega} \tag{3}$$

Thus:

$$\frac{c^2}{v^2} = \epsilon = 1 - \frac{\omega_p^2}{\omega^2} = 1 - \frac{f_p^2}{f^2} \tag{4}$$

The shift in phase due to the plasma is

$$k = \frac{1}{\lambda_p} = \frac{1}{\lambda_o} \sqrt{\epsilon} \tag{5}$$

crossing a given length of plasma

$$\Phi = k L \tag{6}$$

The phase shift is thus measured in units of wavelengths of the light or in fringes in an interferometer.

$$\Delta \Phi = \left[\frac{1}{\lambda_o} - \frac{1}{\lambda_p}\right] L = \frac{1}{\lambda_o}\left[1 - \sqrt{\epsilon}\right] L \tag{7}$$

or, from equation 4

$$\Delta \Phi = \frac{1}{\lambda_o}\left\{1 - \sqrt{1 - \frac{f_p^2}{f^2}}\right\} L \tag{8}$$

The plasma angular frequency is defined$^{(7)}$ as:

$$\omega_p = \left(\frac{4 \pi N_e e^2}{m_e}\right)^{1/2} \tag{9}$$

or numerically

$$f_p = \frac{\omega_p}{2 \pi} = 8.97 \times 10^3 \; N_e^{1/2} \tag{10}$$

where $N_e$ is measured in electron $cm^{-3}$.

At $N_e = 10^{16}$ (the density we expect) $f_p = 8.97 \times 10^{11}$ Hz. For ruby lasers $f = 4.318 \times 10^{14}$ $H_2$. For $H_e$ - $N_e$ lasers $f = 4.737 \times 10^{14}$ Hz. Thus, a 1 cm thick plasma of $N_e = 10^{16}$ $\mathrm{cm}^{-3}$ will shift the phase of a He - Ne laser beam by .028 fringes.

A multiple pass instrument is thus necessary to make meaningful measurements.

## 3.3 The Interferometer

A folded Mach Zehnder interferometer was designed and constructed to best fit the requirements of this study. The open arm Mach Zehnder interferometer was chosen as it is easier to adjust than the closed arm Michelson system. This is particularly important where the light paths must be offset in order to carry a pattern of straight fringes a considerable distance from the instrument. It was found necessary to have the photomultiplier detectors outside the accelerator vault to shield them from radiation and electrical noise, so this is a considerable advantage. As the plasmas are roughly cylindrical, it was considered more important to be able to adjust the number of passes than to have fine resolution along the electron beam axis. A photograph of the instrument is shown in Figure 35. It consists of an aluminum space frame. The accelerator drift tube fits between the open ends of the U. The instrument is tilted to get the maximum aperature consistent with having the reference beam clear the bottom of the drift tube.

In operation the laser beam is expanded and refocused to a parallel beam with lenses. It passes through a 5 mm wide slit. As the electron beam is horizontal, this rectangular light beam is aligned with its long axis vertical, and filling the instrument aperture. It passes through a 45° beam splitter. The upper (active) beam passes through the drift chamber, which has non-reflecting windows, and the plasma. It is passed back and forth through the chamber by low loss dielectric mirrors, which are adjusted to keep the beam at the same height and to move it further downstream with each bounce. It finally misses the edge of the further mirror and goes to a 45° reflector which sends it to the second beam splitter where it is recombined with the lower (reference) beam.

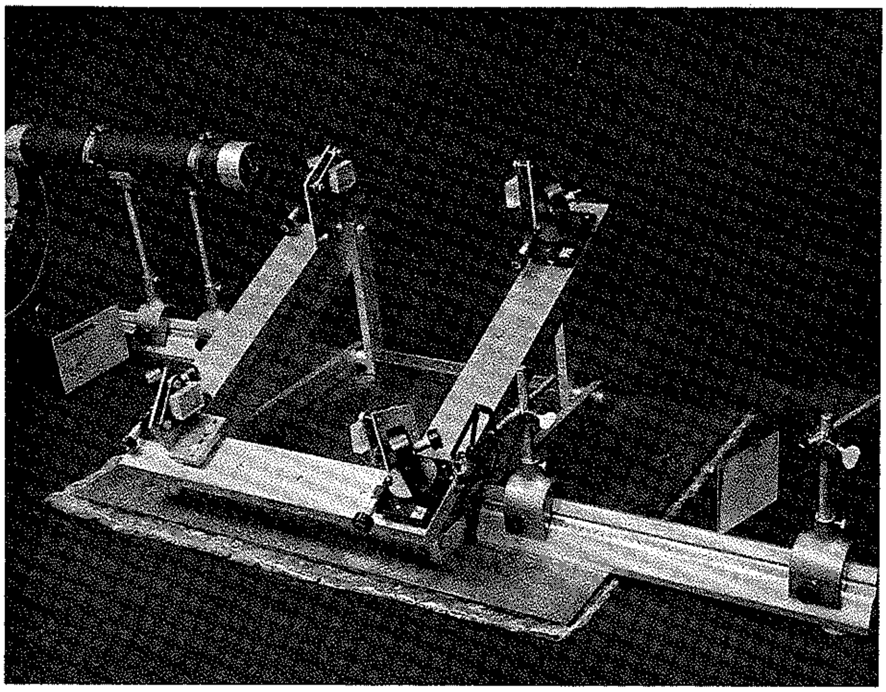

Figure 35 Multiple Pass Interferometer

The course of the reference beam is the same as the active beam except that it misses the chamber. It is folded in order to provide an equal path length for both arms, to minimize coherence requirements on the laser and to minimize the effect of room vibrations on the instrument. It was not found necessary to use a single mode laser. Setting the interferometer on a steel plate, separated from a heavy table by polyethelyne air bag insulation (normally used in shipping) provided adequate vibration insulation.

With this type of interferometer, if the outer and inner mirrors were set accurately parallel, the resulting parallel recombined beam would be light or dark depending on the relative length of the two split beams. A change of phase will produce interference fringes moving across the face of the recombined beam. In actual operation, one of the mirrors is tilted slightly to provide a pattern of fringes suitable to the detection system used.

## 3.4 Helium Neon Laser Measurements

The interferometer was set up to measure the electron density produced by the FX-1 accelerator. Using a multiple pin cathode a pulse of 37,000 A peak lasting 30 ns (half maximum) was produced. The voltage and current characteristics of this beam are shown in Figure 36.

A 4 mW He-Ne laser was used to illuminate the interferometer which was set to traverse the plasma nine times. The setup is shown in Figure 37. The mirror was adjusted to produce fringes parallel to the electron beam. The spatial position of the fringe pattern was optically indexed so that its position was known relative to the electron beam axis. The fringe pattern was sent (using mirrors) 15 meters away to the detectors which were shielded by a concrete wall and lead bricks.

The image pattern was rotated with a dove prism to align it with the (vertical) detector slits. The detector assembly is shown in Figure 38. It is constructed of two identical detectors. Each detector consists of a slit, a laser band pass filter and a photomultiplier. The fringe pattern is split parallel to the fringes by a mirror between the detectors. The size and spacing of the fringes are adjusted with a lens so that the two detectors record parts of nearby fringes,

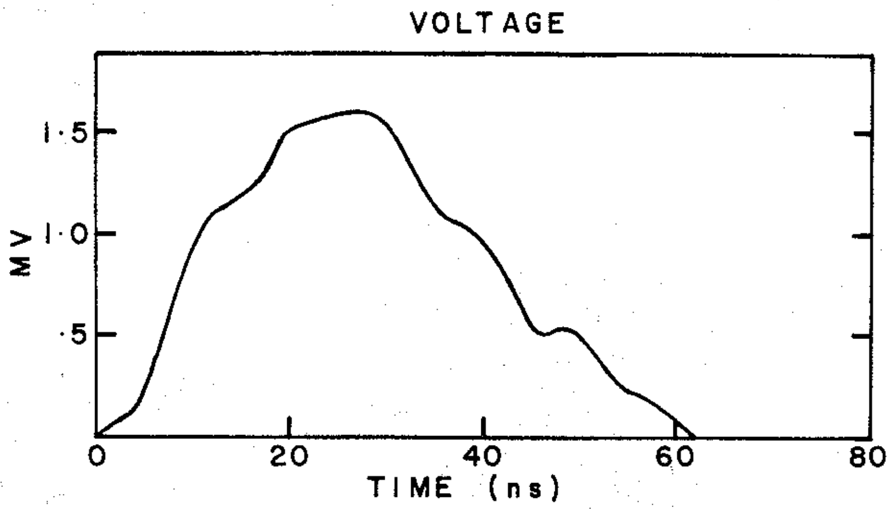

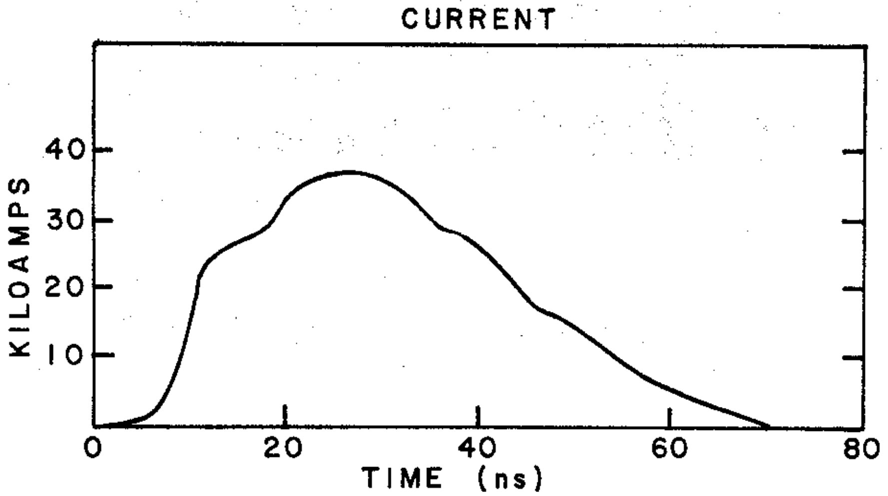

Figure 36. Voltage and Current
20 Pin Cathode, 2.0 cm Gap

1-3741

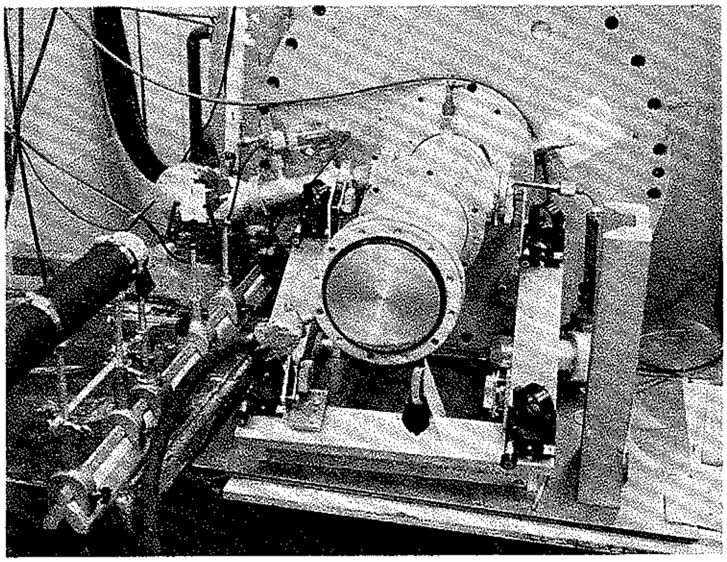

Figure 37. He-Ne Interferometer Experiment

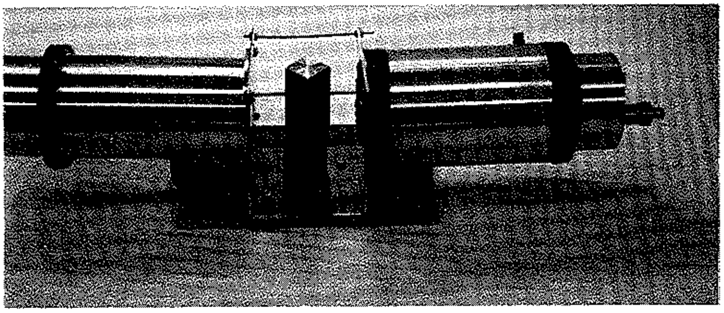

Figure 38 Fringe Shift Detector Assembly

a non integral number of half wavelengths apart. By reading the indicated shifts from the two detectors an unambiguous measurement can be made of the peak density, which is seen as a shift of a partial fringe on at least one of the detectors.

Fringes representing a measured spatial position inside the drift chamber were allowed to fall on the detector assembly. The time history of the intensity of the fringe crossing the set positions were recorded on two oscilloscopes. A sample set of three fringe signatures seen at .3 Torr in air, on the electron beam axis 25 cm from the beam entrance window are shown in Figure 39. Traces of the signals from the two detectors (a and b traces) are shown on two time scales (.2 μs and 2 μs) for three successive pulses of the accelerator, under identical conditions. In each case a shift of approximately three fringes is seen (on the fast sweep) as the density increases, leading to a reversal of the fringe direction (a partial fringe) at about two microseconds, followed by a shift of three more fringes as the density decays.

The time and spatial history of a "typical" plasma can be unfolded by an analysis of a series of such pulses taken at different positions in the drift chamber. Displays of this typical plasma development are shown (in air, 25 cm downstream) in Figure 40 at .15 Torr and in Figure 41 at .3 Torr pressure. Five different radial sections were measured. The horizontal error bars include all the times at which a specific shift was observed for both detector measurements for three pulses at each position. The vertical error bars indicate the estimated partial fringe shift at peak density. The whole display represents the average electron density distribution of fifteen pulses.

An examination of the two displays shows that they are quite different. From the earliest detected shift until the peak density is reached, the central shift leads the off axis shifts at .15 Torr and trails them at .3 Torr. Thus at the lower pressure an axially peaked plasma is indicated and at the higher pressure a hollow plasma is oberved. By this technique, changes in electron density can be followed in time for a limited number of positions. The absolute density can be estimated from the indicated width of the plasma. As an example, in Figure 40 (.15 Torr in air) at 1 μs a centrally peaked distribution about 1 cm

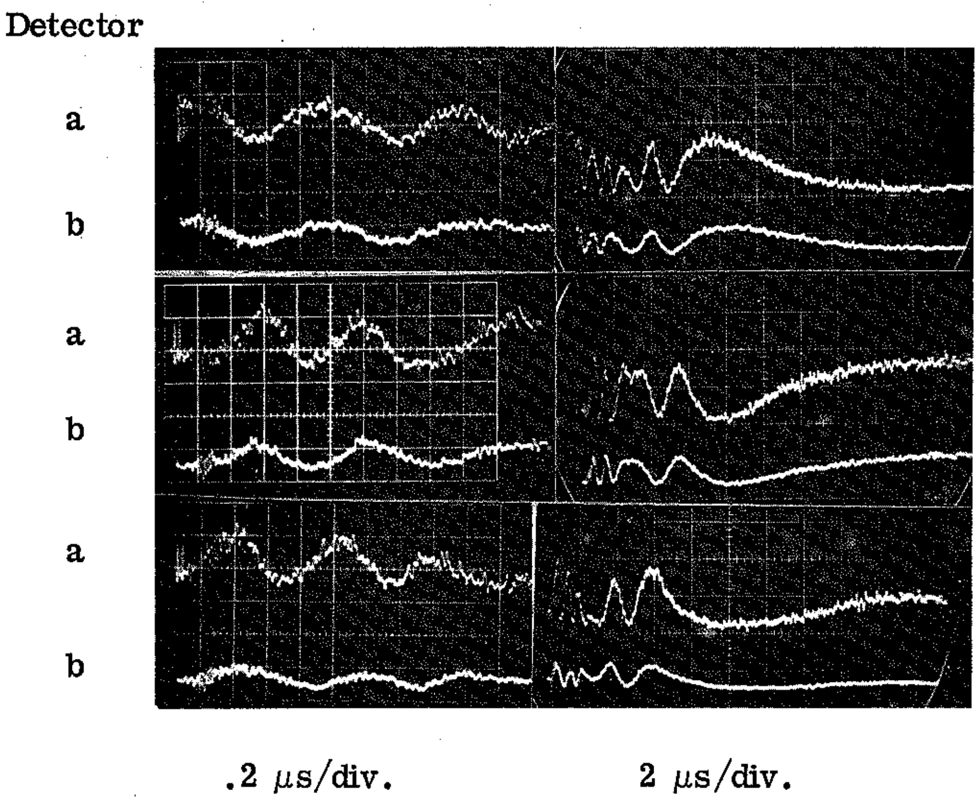

Figure 39. Photo Electric Readout. (Fringe Intensity versus Time.)

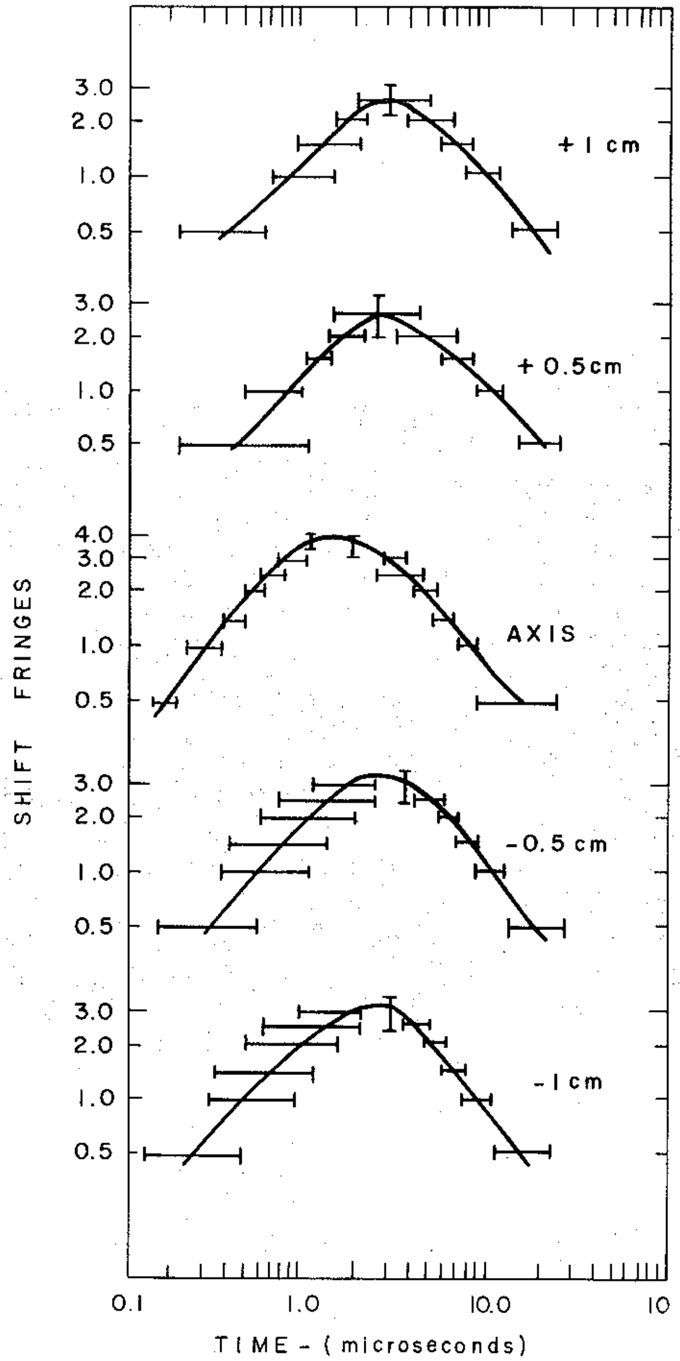

Figure 40. Fringe Shifts versus Time .15 Torr, 25 cm Down Stream

1-4114a

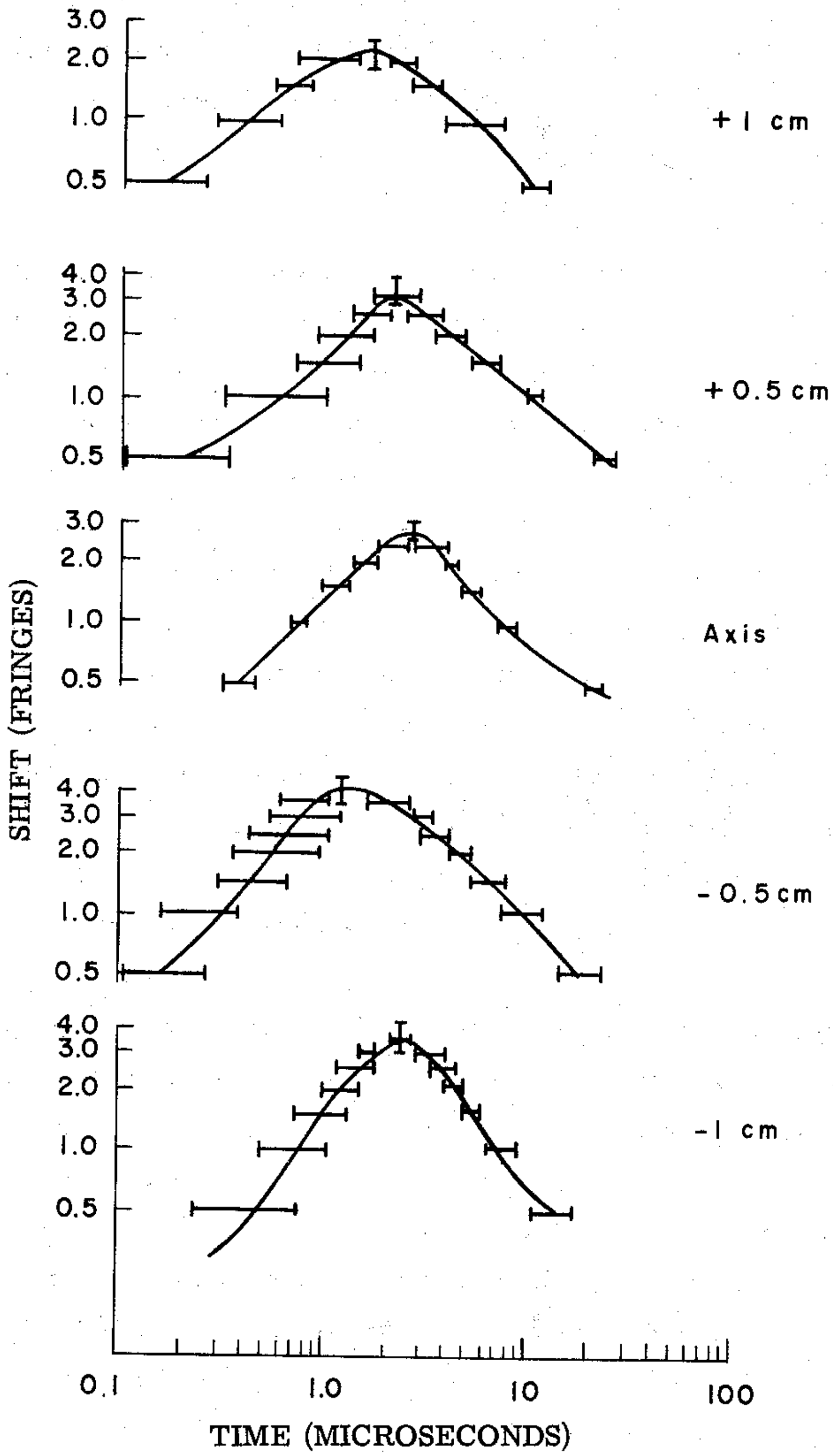

Figure 41. Fringe Shifts versus Time at 0.3 Torr, 25 cm Downstream.

thick is indicated with a total shift of 3.5 fringes. This gives an electron density of $1.4 \times 10^{17}$ $cm^{-3}$ for this "typical" distribution at this time.

## 3.5 Ruby Laser Measurements

Up to approximately 1 μs the plasmas were found to be smaller than the aperture of the interferometer. During these early times in the plasma development it is practical to illuminate the interferometer with a Q-switched ruby laser and record the fringe pattern across the whole plasma at one time using photographic film. The experimental arrangement was changed slightly. A photograph of this set up is shown in Figure 42. The mirrors were adjusted so that the fringe pattern was perpendicular to the electron beam axis. A Korad K 1500 laser (out of sight behind the accelerator) was used at a low power and without its amplifier to illuminate the interferometer. The parallel light beam coming out of the interferometer carrying the fringe pattern was terminated with a ground glass screen. The image on the screen was photographed with a crown graphic camera through a ruby laser band pass filter. Type 47 Polaroid film was used. This film is normally insensitive to 6943 Å light but will record the Q-switched laser pulse. The camera shutter was left open.

The laser and accelerator were triggered in timed sequence. The laser flash lamps were fired first. Then when the flash lamp output peaked, the accelerator was fired and a timed delay later the Q-switch was triggered. As both units have intrinsic jitters of less than 10 ns accurate timing was possible. The current was monitored with a return current shunt. There are two recombined laser beams beyond the last beam splitter. The previously unused one was sent to a photodiode which recorded the laser pulse. Matched delay cables were used, leading to two Tektronix 519 oscilloscopes. It takes 12 ns for light to traverse the interferometer when nine passes are used. This represents the ultimate time resolution of the system. As used, the accelerator pulse had a 30 ns half height width and the laser pulse about a 20 ns half height width.

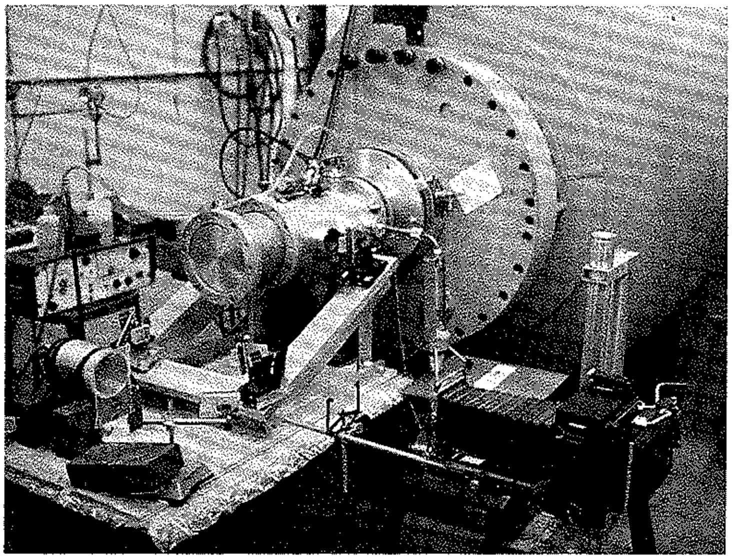

Figure 42. Ruby Laser Experiment

In Figure 43 a series of fringes are shown to display the development of a plasma in Helium at .8 Torr, 10 cm from the beam entrance window. The distance between the index lines corresponds to 1 cm inside the drift tube. The first picture in the display is of the unperturbed fringe pattern, taken without firing the accelerator. This display is quite stable from pulse to pulse but does drift slowly during operation. The second pattern was taken (i.e., the laser light peaked) at 65 ns after the leading edge of the beam entered the chamber. The timing of the light and current pulses is shown for this pattern above the fringe display. In this case the measurement overlaps the trailing edge of the current pulse. In the fringe pattern a small inflection of the fringes is seen (relative to the reference fringes) just at the central index mark. In the next two fringes at 100 ns and 125 ns this pattern can be seen to grow. It grows further at 150 and 200 ns. The fringes had to be adjusted so these last two are referred to the final reference fringe.

A view of the later development of a plasma is shown in Figure 44 in air at .15 Torr. The fringe shifts are seen to increase and expand from .3 μs to 2 μs. After 1.5 μs the plasma fills the aperture of the instrument and the edges of the fringe pattern move, making absolute measurement impossible.

In Figure 45 a series of fringes are shown at various times for .3 Torr pressure in air, at the 30 cm downstream port. The fringe patterns observed are either flat topped or slightly concave at the center supporting the earlier average observation of a hollow plasma distribution, under the same conditions.

The fringe patterns of the plasmas produced under varying conditions were analyzed by tracing each fringe and its appropriate reference pattern, taken shortly before or after (without firing the accelerator). These were overlaid and the net shift was read in fringes each 2 mm across the aperture. Net fringe shift curves were constructed and their height in fringes and widths (full width half maximum) in cm were measured. There were too few data points to perform an Abel inversion to compute radial fringe shift distribution and many distributions were neither smooth nor symmetrical. The width of the measured profile was taken to be the fringe ( and therefore density) half width accepting

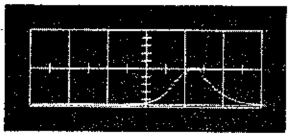

Laser Pulse

20 ns/div

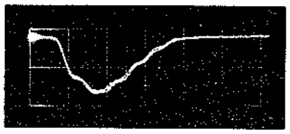

Accelerator Pulse

20 ns/div

Timing for Fringe Display
Labeled 65 ns

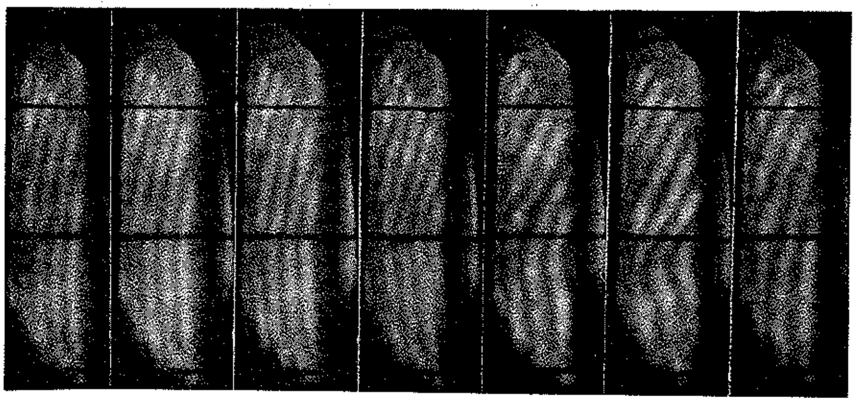

Unperturbed Fringes (65 to 125 ns) | 65 (ns) | 100 (ns) | 125 (ns) | 150 (ns) | 200 (ns) | Unperturbed Fringes (150 to 200 ns)

Figure 43 $N_e$ Profiles at Early Times in 0. 8 Torr of He at 10 cm Window

2-1387

Reference Fringes

0.3 (μs)

0.4 (μs)

0.5 (μs)

0.75 (μs)

0.95 (μs)

1.5 (μs)

2.0 (μs)

Figure 44 $N_e$ Profiles in Air at 0.15 Torr Pressure, 30 cm Downstream

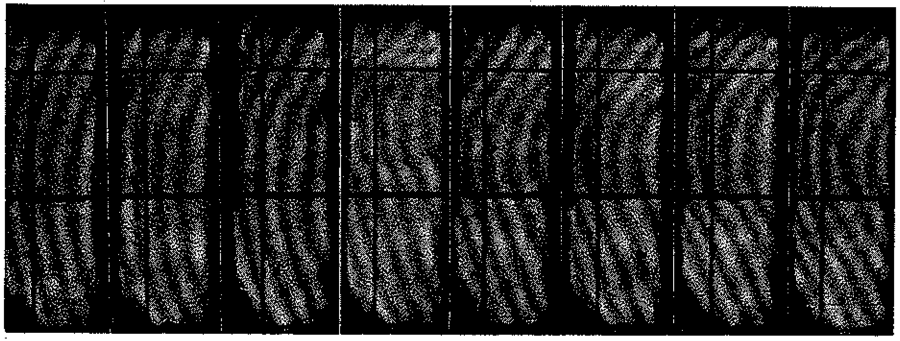

Figure 45. $N_e$ Profiles in Air at 0.3 Torr Pressure, 30 cm Downstream at Discrete Times.

the small error which results. On this basis measured widths (FWHM) and electron densities were computed for various gases and pressures and are displayed in the following eight figures as a function of time for two locations, 10 cm and 30 cm from the beam entrance window.

The results are shown for helium in Figure 46 at .9 and .9 Torr pressure. The earliest time at which a plasma was detailed was at .8 Torr in Helium, where a fringe shift at the 10 cm position was seen at 65 ns (after the entrance of the leading edge of the electron beam into the drift chamber). For the first 200 ns both the density and the width of the plasma grow then remain stable for 600 ns. At later times the width of the plasma again grows filling the instrument aperture which prevents later measurement by this technique. The stable value of electron density appears to be above the original density of available electrons in the neutral gas ($N_e^o$).

In hydrogen at .9 Torr at 10 cm (Figure 47) the plasma visibly narrows after several hundred nanoseconds and the density rises to several times $N_e^o$, then quickly expands. The effect is not seen at 30 cm although the density is high.

In air at .3 Torr (Figure 48) the narrowing effect and late density rise is again seen. Further downstream the plasma maintains its width and a density less than $N_e^o$ (presuming 7 available electrons per atoms) for a microsecond. In air at .15 Torr (Figure 49) in both locations show an earlier density rise and a gradual decay. In nitrogen at .3 Torr (Figure 50) and at .15 Torr (Figure 51) the density signatures are substantially the same as in air. With somewhat fewer points the data appeared to scatter more in nitrogen. With argon at .3 Torr (Figure 52) and .15 Torr (Figure 53) the whole plasma signature in width and density slowed down and the general trends decreased in amplitude. The observed densities did not approach $N_e^o$ for argon (with 18 electrons).

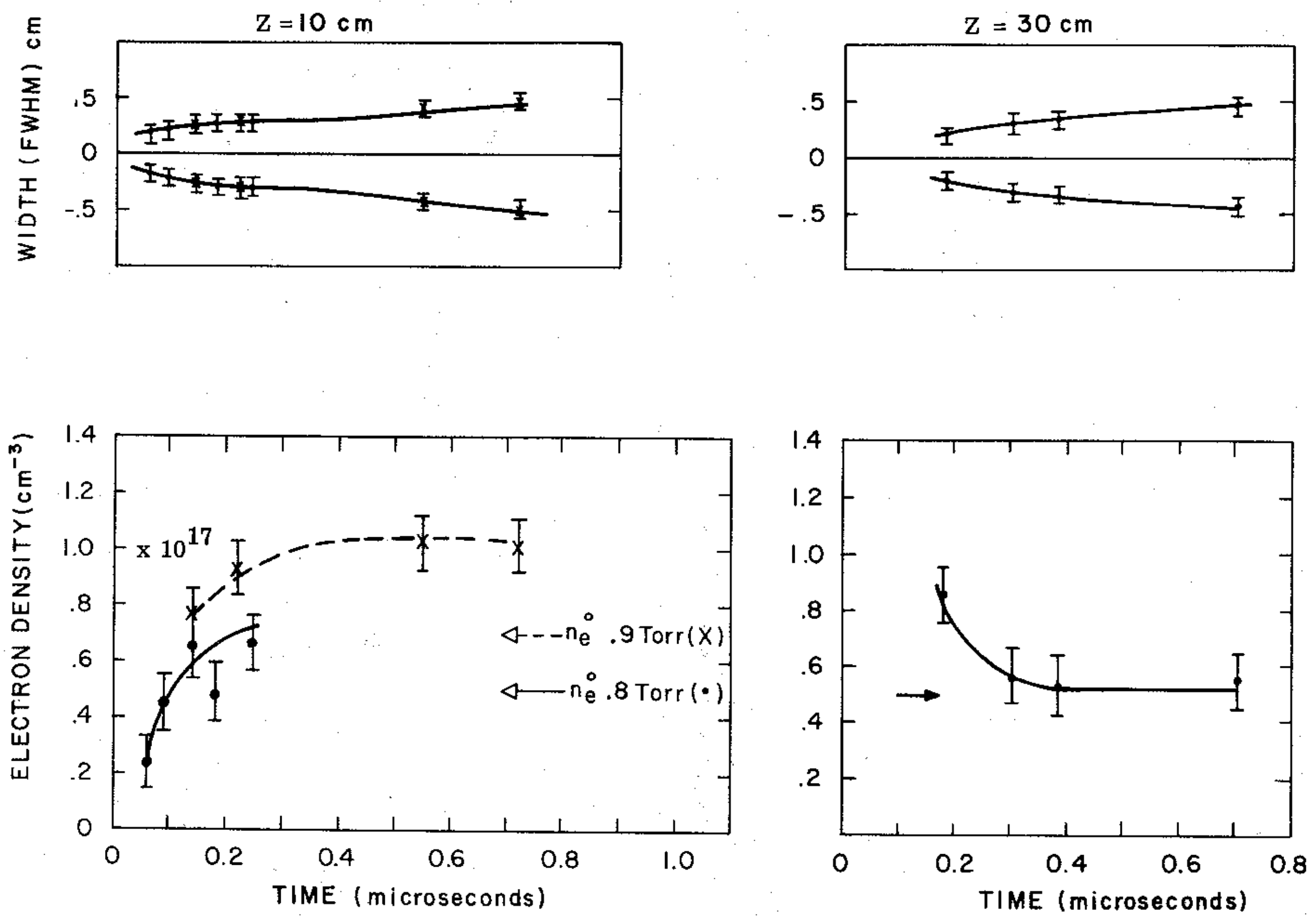

Figure 46. $N_e$ in Helium at .8 and .9 Torr

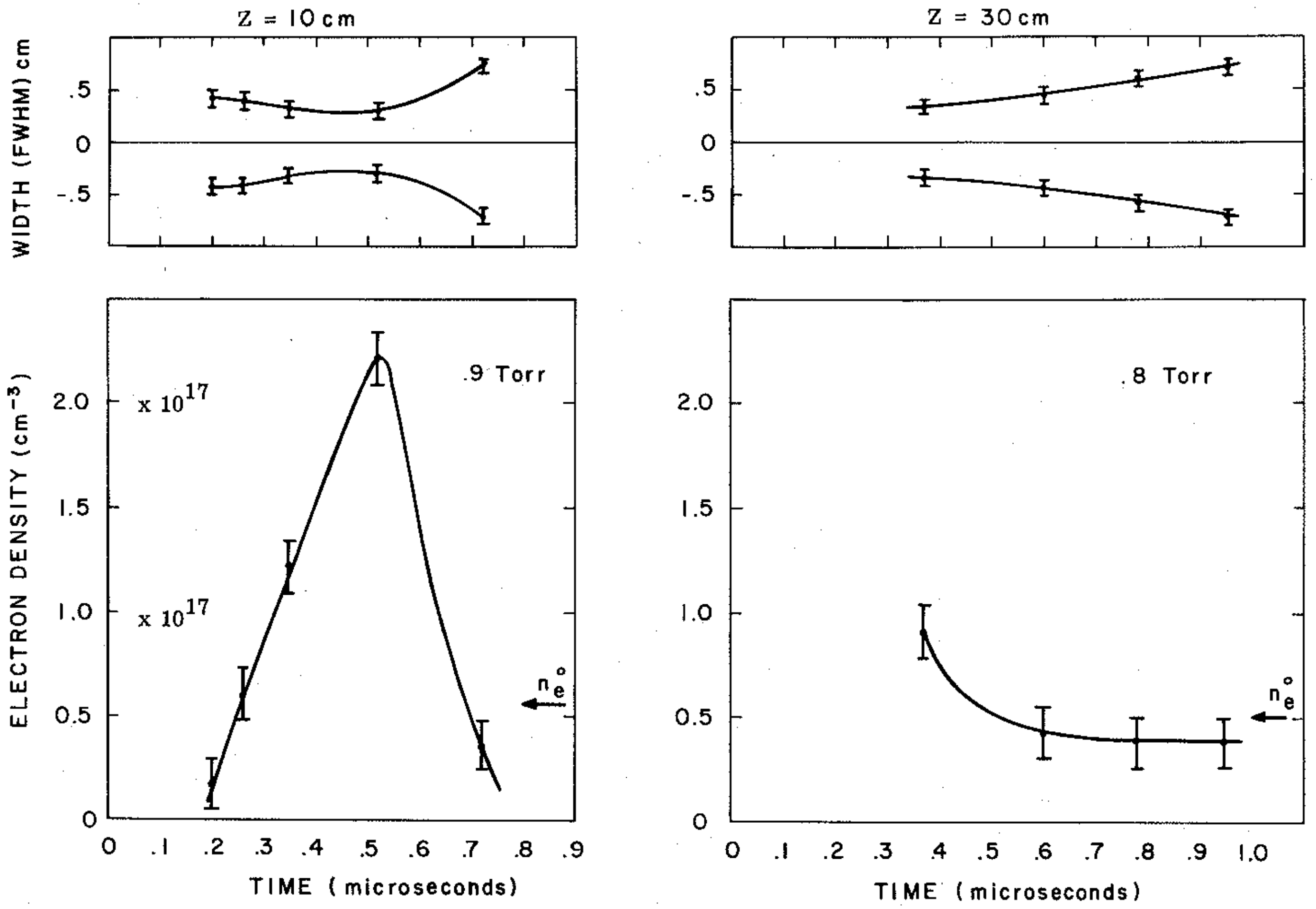

Figure 47. $N_e$ in Hydrogen.

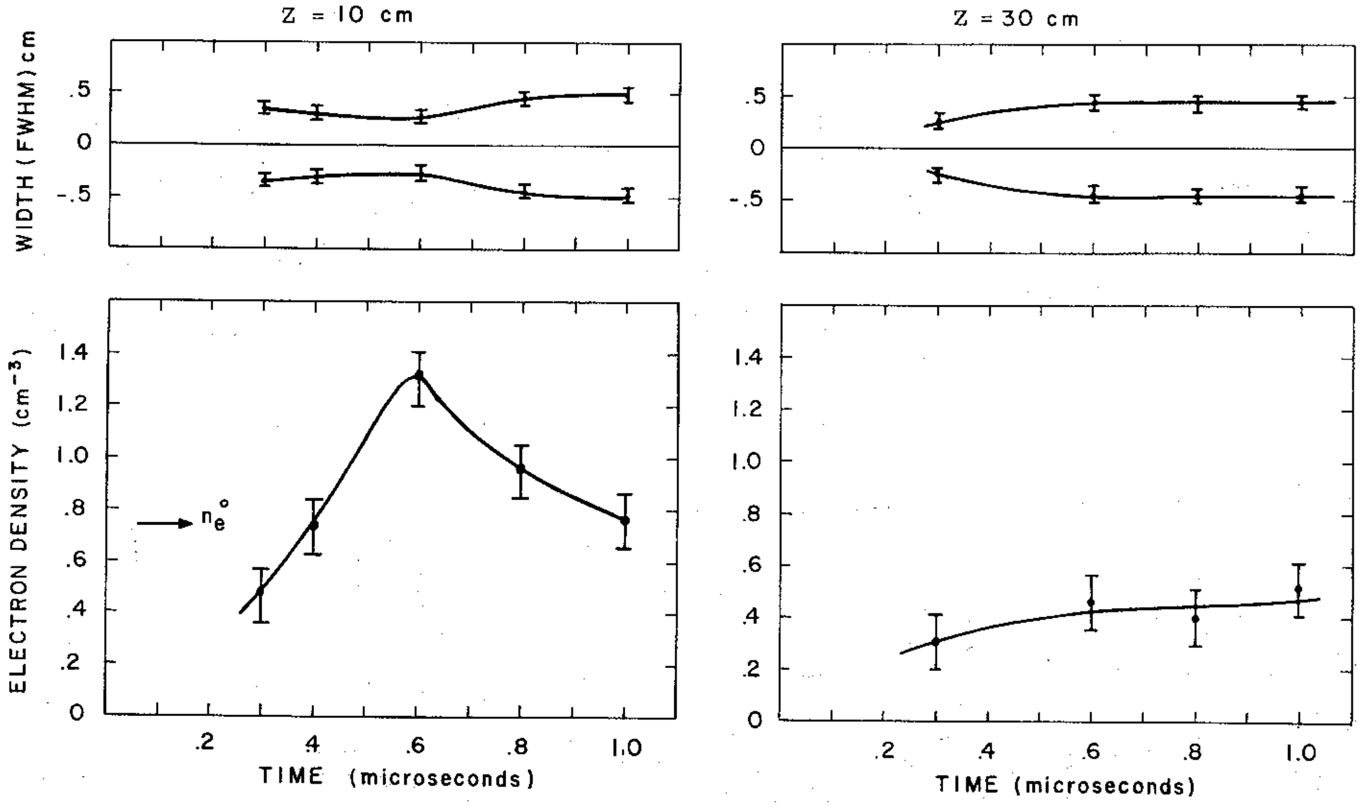

Figure 48. $N_e$ in Air at .3 Torr.

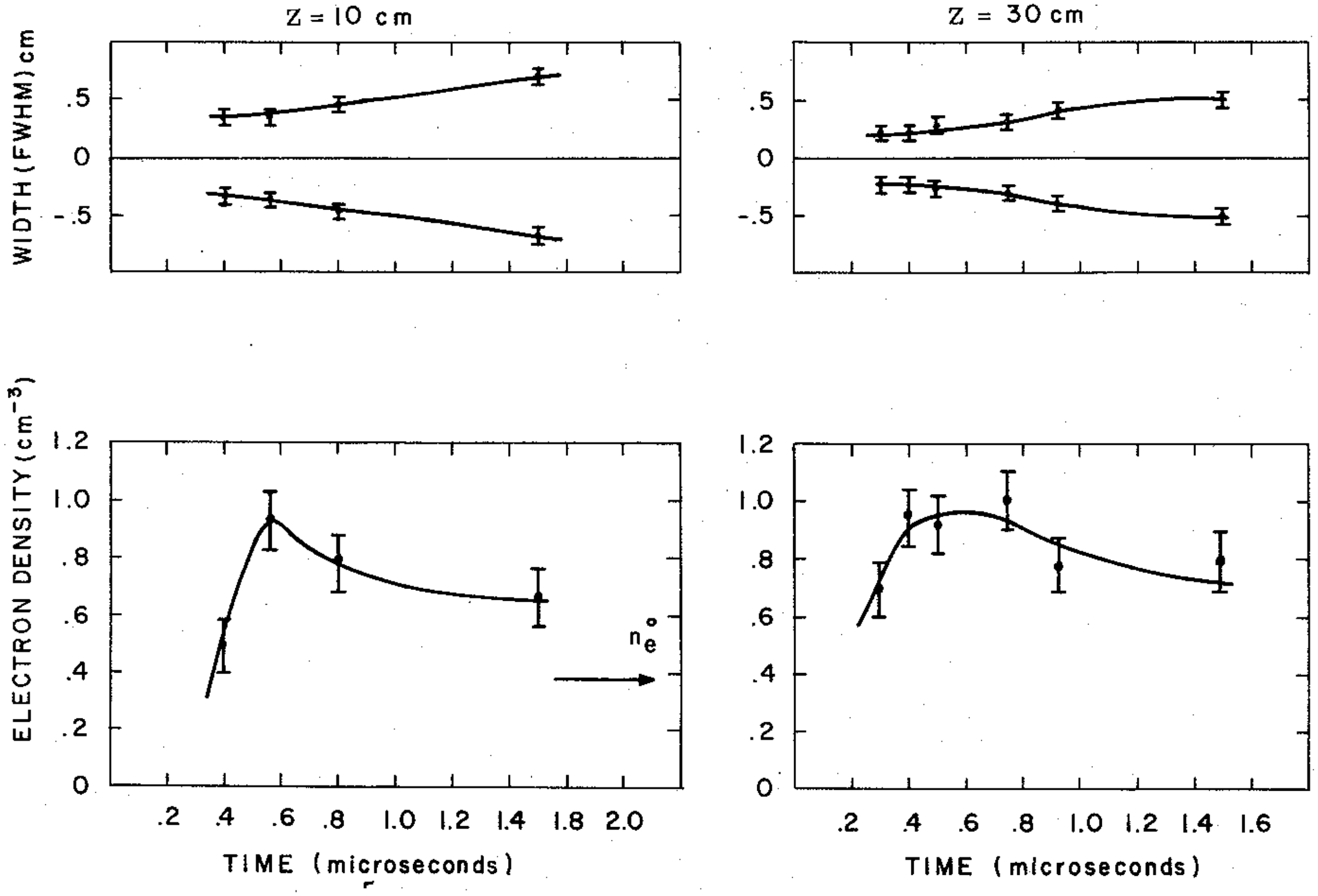

Figure 49. $N_e$ in Air at .15 Torr.

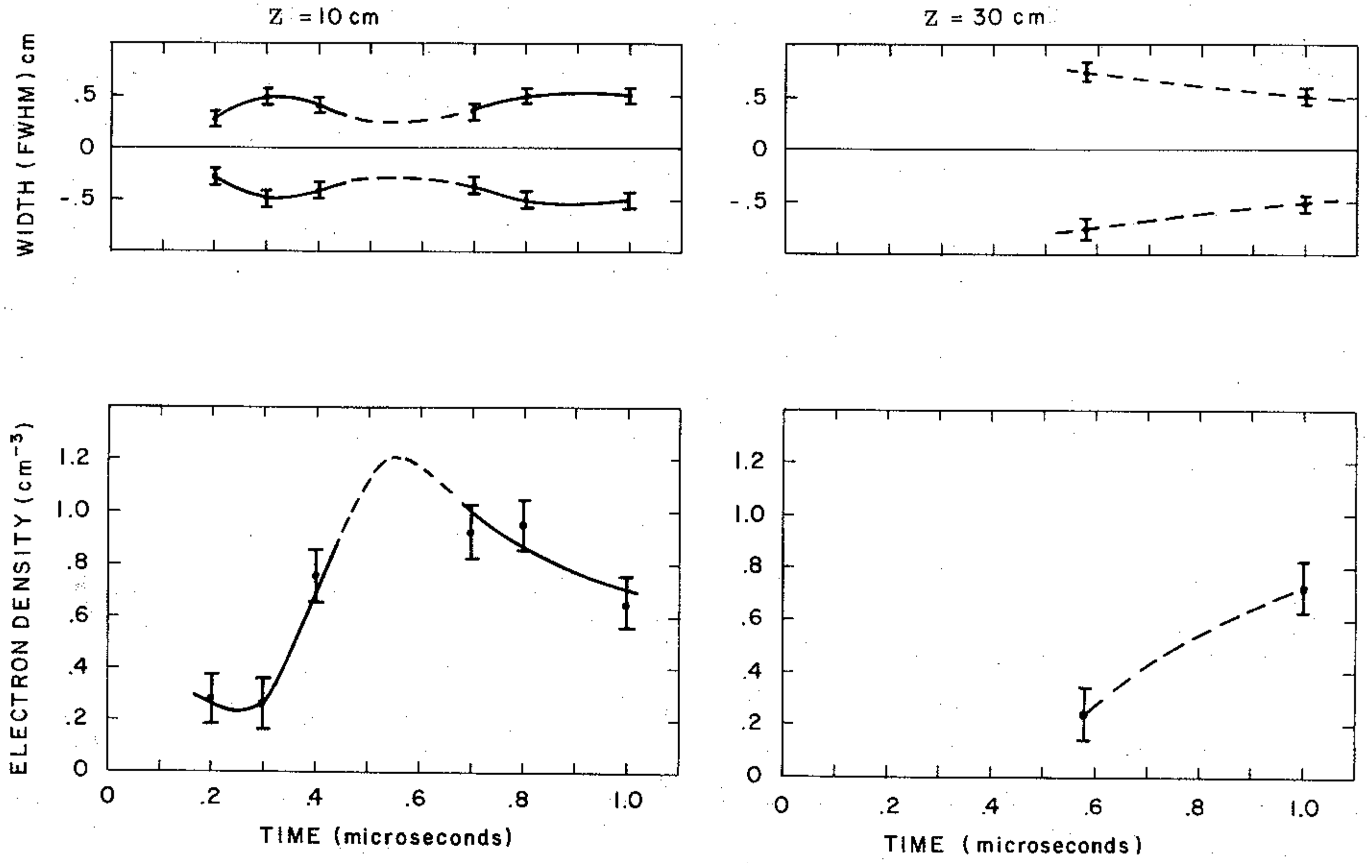

Figure 50. $N_e$ in Nitrogen at .3 Torr.

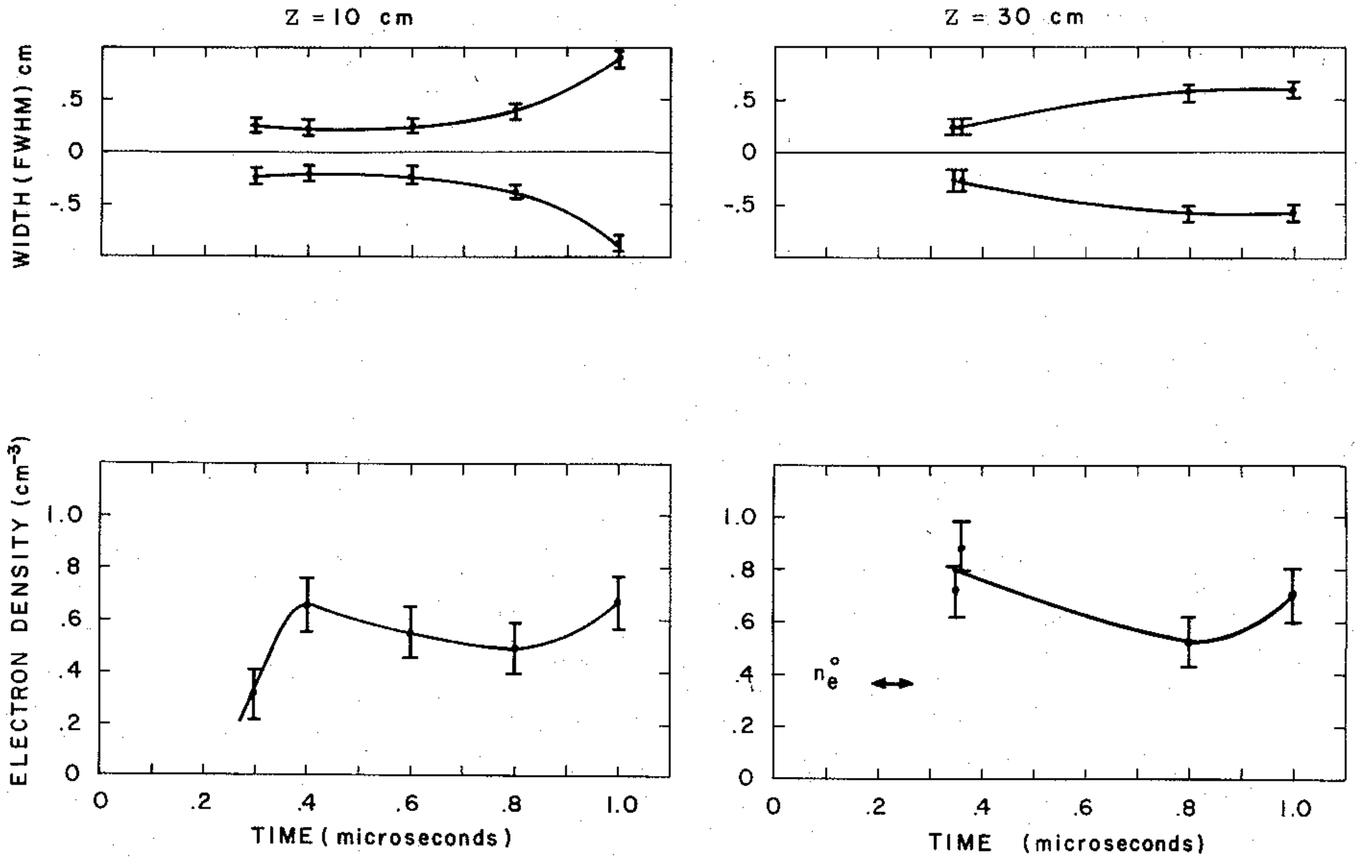

Figure 51. $N_e$ in Nitrogen at .15 Torr.

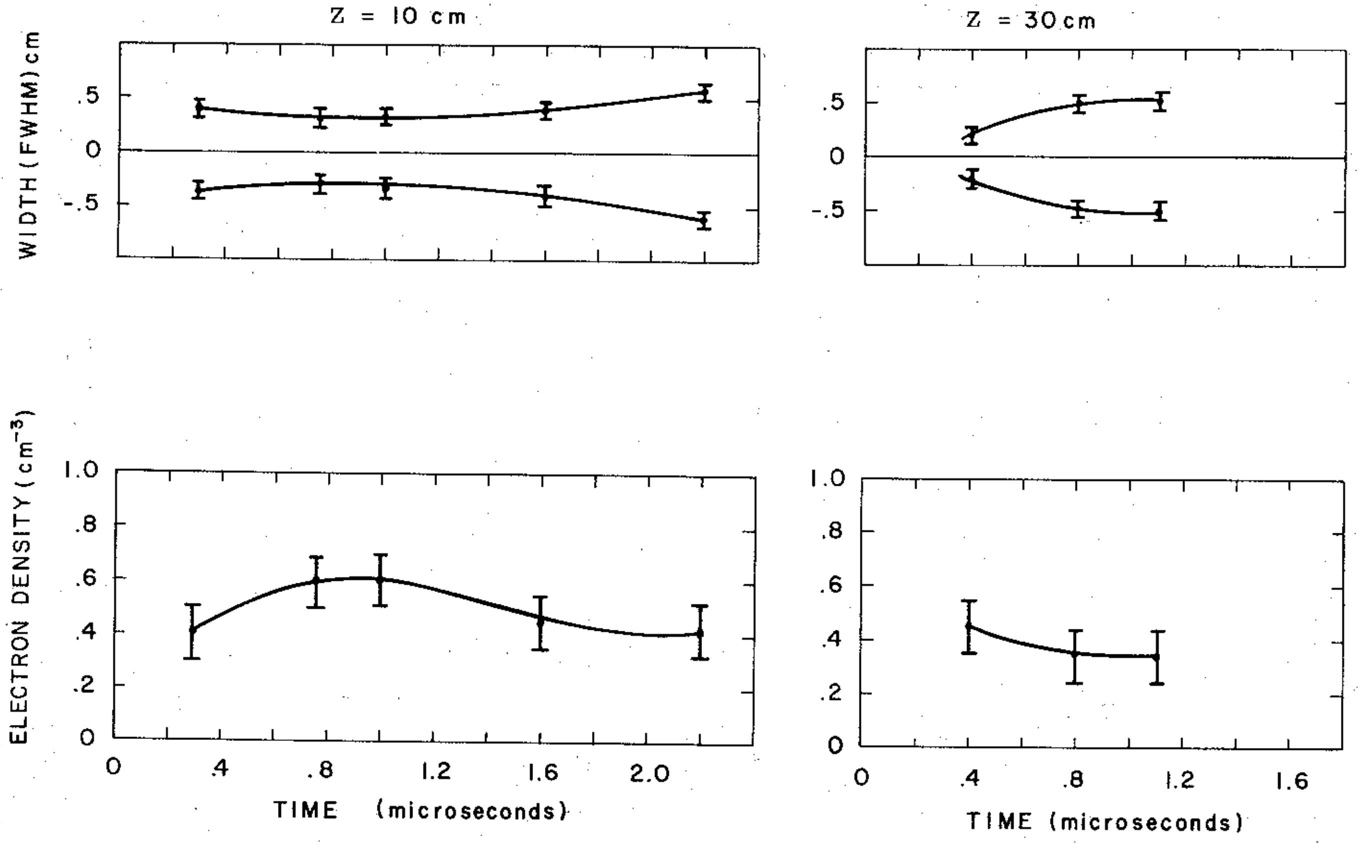

Figure 52. $N_e$ in Argon at .3 Torr.

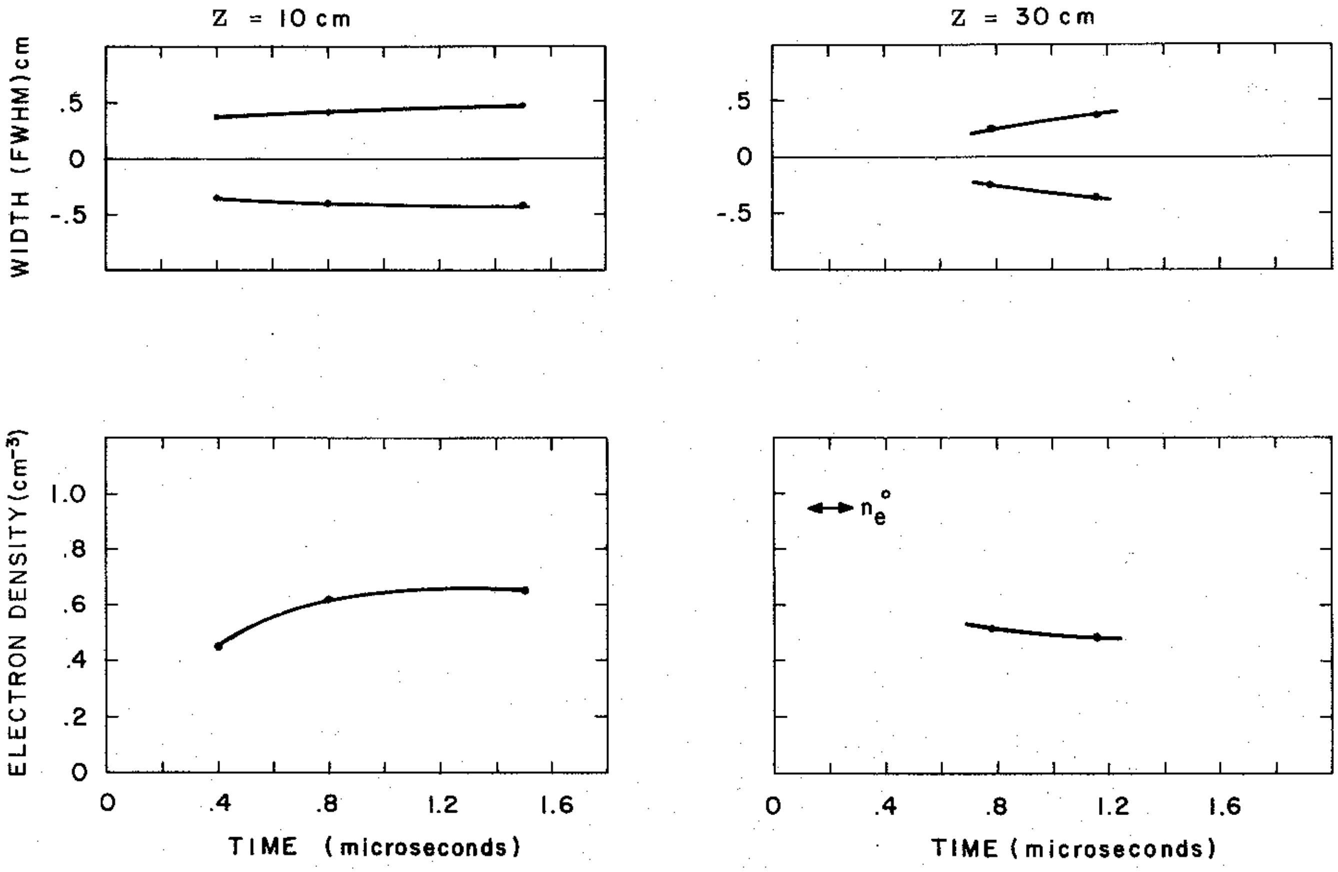

Figure 53. $N_e$ in Argon at .15 Torr.

## 3.6 Discussion

Examination of all the data gives a picture of a plasma with the initial conditions determined by the primary electron beam. The plasma does not freely expand but appears to be confined. The physical size of the plasmas remain stable for hundreds of nanoseconds and under some conditions will visibly narrow. The electron density is higher than the original density of available bound electrons for all light gases even presuming total stripping of the atoms. When the plasma is seen to narrow the density rises abruptly and falls back rapidly. The details of the density signatures are functions of axial distance in the region of observations.

These effects can be explained by considering the dynamics of the primary electron beam. The trajectories of the electrons in the primary beam are discussed in Section 5 of this report. The 10 cm window is in the region of the first well defined beam pinch and the 30 cm window is in the region of smeared pinching. The annular magnetic fields associated with a pinching electron beam are established during the current rise. In the region of the first pinches they form roughly biconical magnetic surfaces. Secondary electrons are largely trapped by the magnetic field.

Under the conditions we have been investigating, ionization of the gas by primary and secondary electrons can be very rapid. As the secondaries cannot get away, an ionization cascade can be formed which goes substantially to completion. The speed of the observed cascade ($N_e = 10^{16}$ cm$^{-3}$ before the end of the pulse) produces a level of ionization density much greater than the primary beam ($10^{12}$ cm$^{-3}$) by the time of the peak of the pulse. The plasma envelopes the magnetic field and the interaction of the two dominates the balance of the discharge. The magnetic field confines the plasma drift to diffusion rates through the field. The magnetic field pressure is unbalanced due to its curvature but in order for the field to move it must accelerate the entire mass of the ions in the plasma. Hence, for hundreds of nanoseconds the plasma moves very little and an image of the primary beam is preserved. When the magnetic field expands it does so by driving a secondary current through the center of the plasma in the same direction as the primary current and back through the outer plasma or walls.

Currents rising to 45,000 A in 20 ns, then smoothly decaying to 15000 A in 600 ns were previously measured in a drift tube filled with air at .2 Torr using the same cathode configuration as this study.(1) The peak current represents both primary (37000 A) and secondary currents (8000 A). An ion drift analysis was worked out by Rostoker,(7) for a cylinder carrying uniform current. The azimuthal field at r = a is

$$B_\theta = 2I/ca$$

For I = 45 kA and u = .5 cm

$$B_\theta = 18 \text{ k Gauss}$$

By 600 ns this has decayed to 15 kA and 6 kG.

A rate of pinching of the plasma can be estimated from momentum balance. The change in momentum of the ions due to the magnetic field is given by:

$$\frac{B_\theta^2}{8\pi} = 2nMV^2$$

For the observed $5 \times 10^{16}$ protons from hydrogen

$$V = 1/2 \frac{B_\theta}{\sqrt{4\pi n M}} = 1.5 \times 10^7 \text{ cm/sec}$$

This gives a time scale for pinching:

$$\tau = a/V = 33 \text{ ns.}$$

This is faster than the observed 600 ns pinching time, but might be the source of the small high density ($N_e > N_e^o$) core sometimes seen decaying at the earliest observable times (300 ns) in the downstream port (Figures 47 and 48).

The magnitude of the secondary current necessary to form a plasma pinch(8) is:

$$I^2 \geq 2nkT$$

where N is the total number of particles per cm of length and I is in emu. Estimating the plasma temperature at no greater than $10^5$ K° requires a current of $1.7 \times 10^4$ amperes to initiate a pinch. This value is exceeded in the observed discharge but it is not clear what value of T can be ascribed to the non-equilibrium plasma which exists before 600 ns. The only measured value we have is for a less energetic plasma formed with a single point cathode where at the beginning of equilibrium at 2 μs, $T = 10^4$ K° was observed.(9)

## 3.7 Summary

It has been demonstrated that the electron densities of relativistic electron beam produced plasma can be measured by techniques of visible light interferometry up to very early times in the discharge. Ionization of the filling gas is very rapid and can lead to an ionization cascade by secondary electrons which are trapped by the axmuthal magnetic field of the primary beam. Under these conditions the primary electron beam propagates in a plasma of its own making. The magnetic field of the beam becomes enclosed in the plasma slowing and stabilizing its expansion. Thus, the plasma retains the image of the primary beam for a considerable time. The subsequent expansion of the magnetic field drives a secondary current almost as large as the primary current.

The secondary current can be long lived and under some conditions is seen to pinch weakly. Peak densities of $2 \times 10^{17}$ cm$^{-3}$ and compressions > 2 were observed. The appearance of the pinch is consistent with a cooling plasma of ($T = 10^5$ K°, $N_e = 5 \times 10^{16}$ cm$^{-3}$) at about 600 ns.

# SECTION 4

# ION ACCELERATION STUDIES

## 4.1 Introduction

This section will review the ion acceleration studies, both experimental and theoretical, which were carried out during this phase of the DASA Beam-Plasma Program Contract DA-49-146-X2-553 (III). These studies were motivated by the observation, made during the previous phase of this contract, that linear electron beams can be used to accelerate light ions to an energy many times higher than the electron beam energy. Given that a physical model can be developed to explain this process, this model should also provide information on the dynamics of the beam propagation itself. This was one reason why it was decided to carry on these studies. Another reason for this work was the possibility that the ion beam could be used as the source of pulsed neutrons, which means that scaling laws are needed to assess how high a fluence level is attainable.

This section will begin with a review of the experimental results which were obtained, followed by a description of a physical model which explains all of the data. Much of the experimental work attempted to parametrize the acceleration process as thoroughly as possible to provide a test of the theory.

## 4.2 Experimental Results

### 4.2.1 Accelerator/Diode Considerations

The pulsed electron accelerator used for the ion acceleration studies is shown schematically in Figure 54. It consists of a 280 pF coaxial capacitor dc charged to 4.0 MV. The coaxial capacitor, which acts like a length of coaxial transmission line, is command switched to a capacitively graded pulse bushing which houses the cold cathode diode used in the experiment.

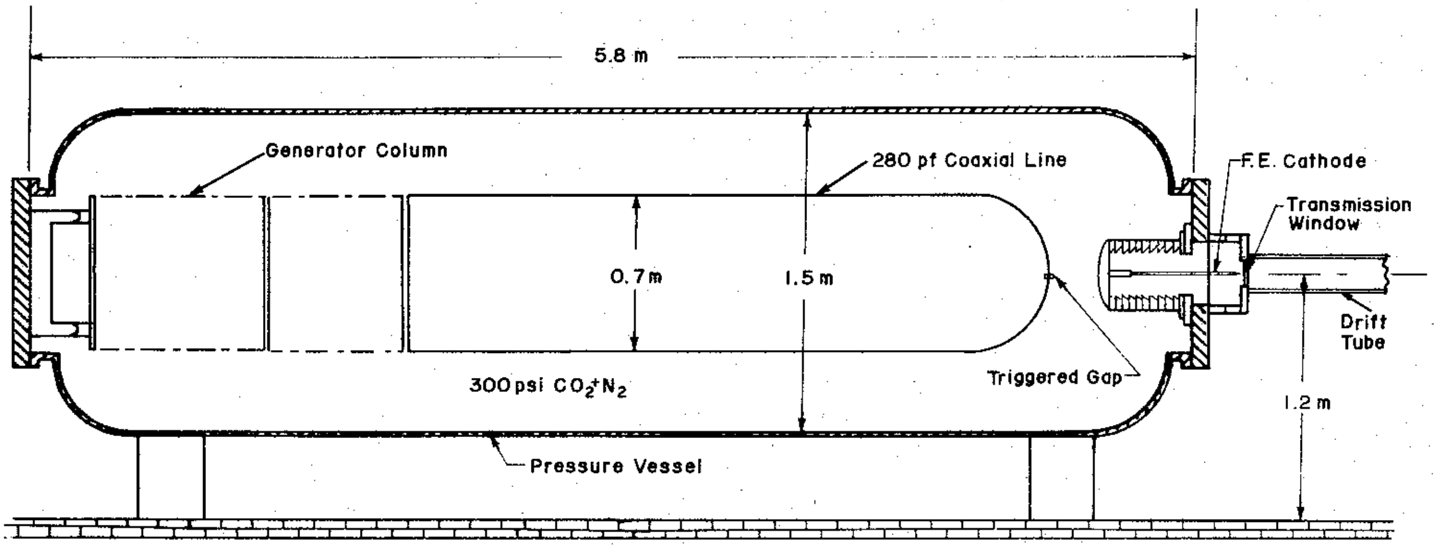

Figure 54. 4.0 MV Coaxial Accelerator Geometry

Two different diodes were used during the course of these studies. The first diode used a multi-point cathode and a thin (0.002-inch) titanium transmission anode. The time resolved voltage, current and calculated diode impedance are shown in Figure 55. Because the cathode is mounted at the end of a highly inductive shank, and the voltage monitor was located several inches behing the cathode, an inductive correction has been made to the voltage pulse. A more complete description of the voltage and current diagnostics, and the geometry of the multi-point cathode, can be found elsewhere in this report (Section 1).

The second diode used consisted of a flat disc of carbon, 1.7 cm in diameter, and again a thin titanium transmission anode. The characteristics of this diode are shown in Figure 56. The two diodes described are seen to have quite similar impedance characteristics, and it was observed that the ion acceleration produced by the electron beams from each diode was quite similar. Figure 57 shows time integrated photographs of the electron beam propagation obtained using the multi-point cathode. Note that in the pressure regime of interest (0.2 Torr) the electron beam propagates without stopping.

### 4.2.2 Time of Flight Measurements

The time of flight experiments conducted during this contract phase were extensions of the earlier work, with improvement being made in the time resolution of the measurements to see if there is, in fact, a dependence of ion energy on the filling gas pressure. Figure 58 shows schematically the experimental configuration used. The electron beam is injected into a 50 cm long drift pipe which contains the gas species of interest. After traversing the length of the drift tube, most of the electron beam is intercepted by the blank-off plate at the end. That portion of the electron beam which enters the smaller drift section, at the end of the main drift tube, is swept to the walls by a 3 k gauss magnet. The ions are only slightly perturbed by the magnetic field, and continue down the smaller drift section until they are intercepted by a Faraday current probe. Only one time of arrival point is obtained for each firing of the machine. The high degree of reproducibility of the system was checked by firing the machine several times, and observing that the time of arrival at a given point

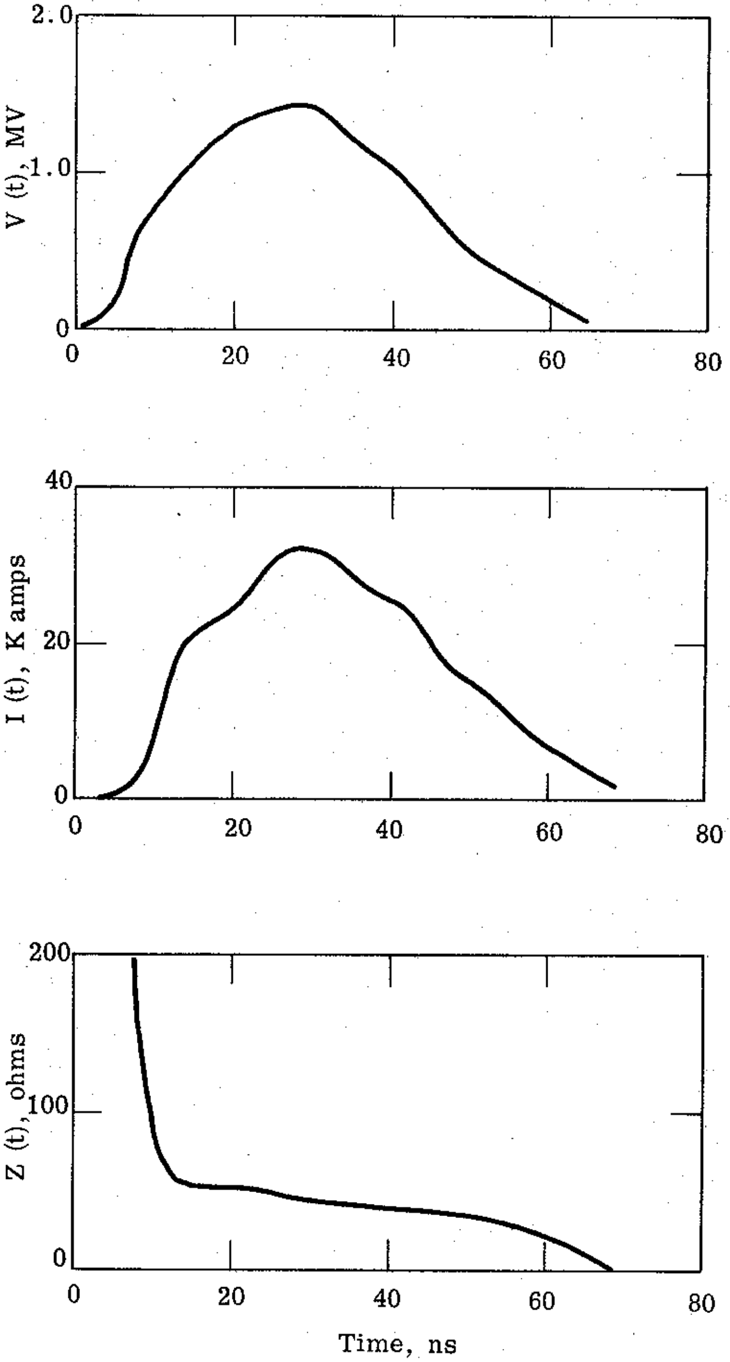

Figure 55. Beam Characteristics of Multi-Pin Cathode

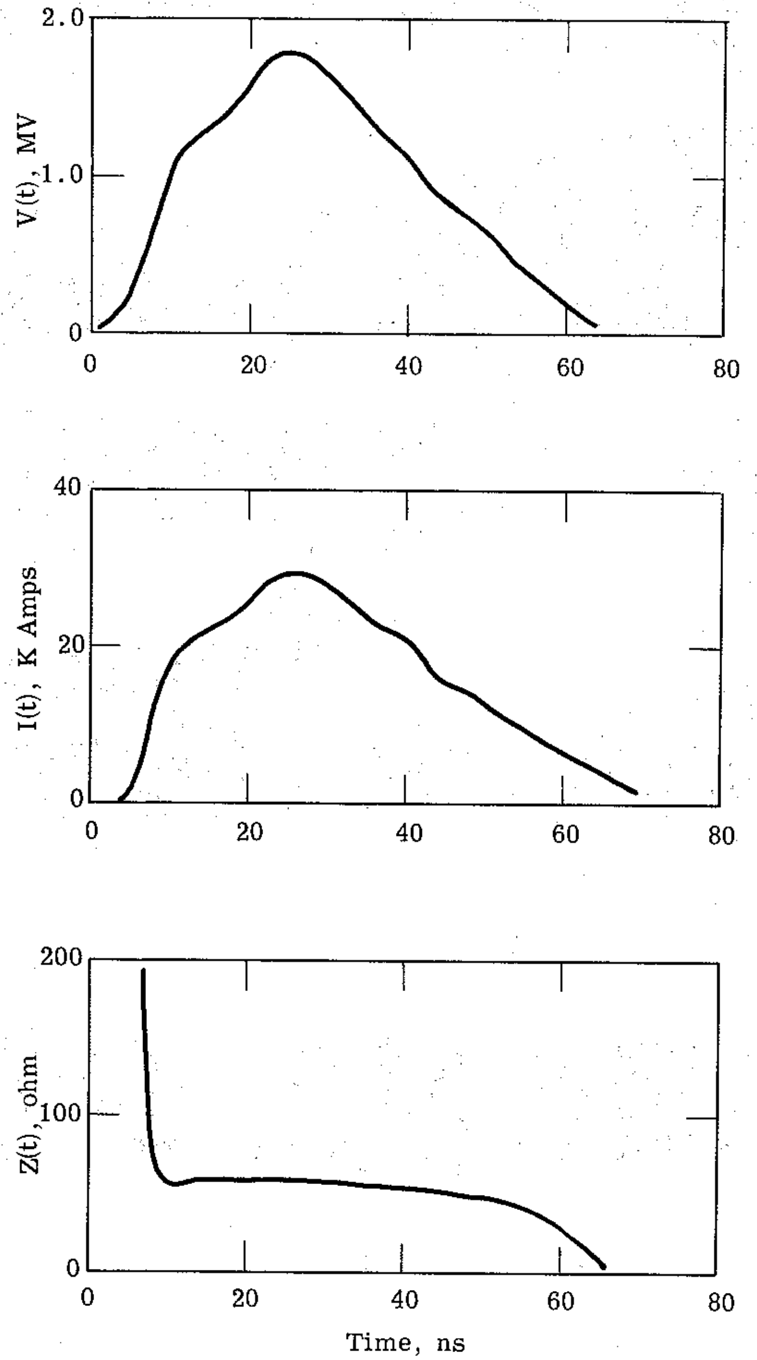

Figure 56. Beam Characteristics of Carbon Cathode

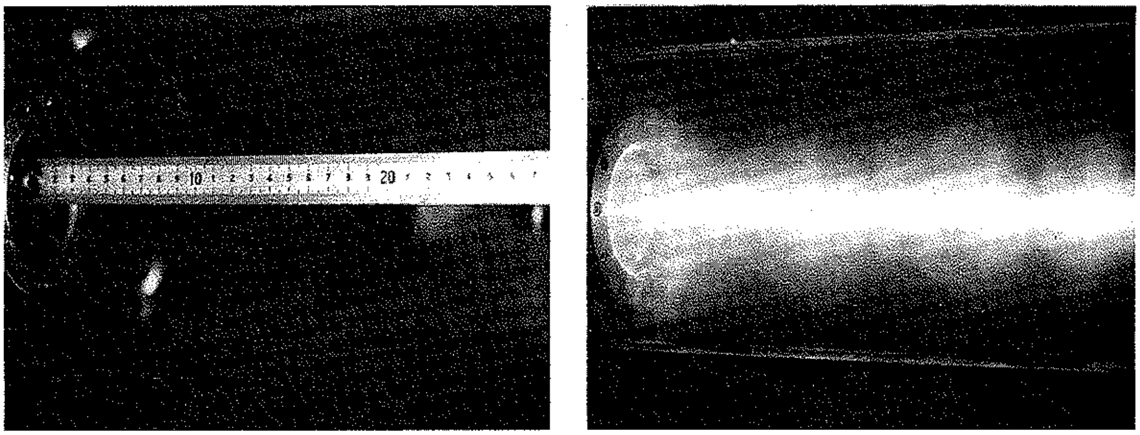

(a) Calibration Scale

(b) Ambient Pressure = 0.2 torr (Air)

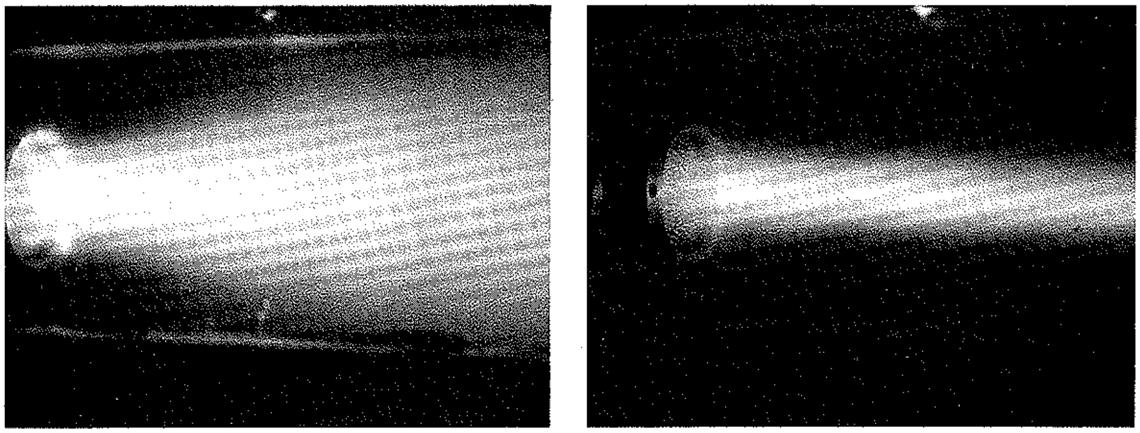

(c) Ambient Pressure = 1.0 torr (Air)

(d) Ambient Pressure = 100.0 torr (Air)

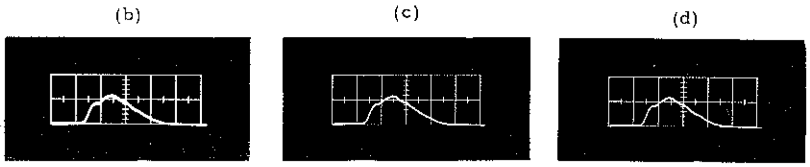

Beam Current Profile
Vertical Scale = 33.0 kA/cm
Horizontal Scale = 20.0 ns/cm

Figure 57 Beam Plasma Photographs for a Multi-Point, Low Impedance Cathode

2-943

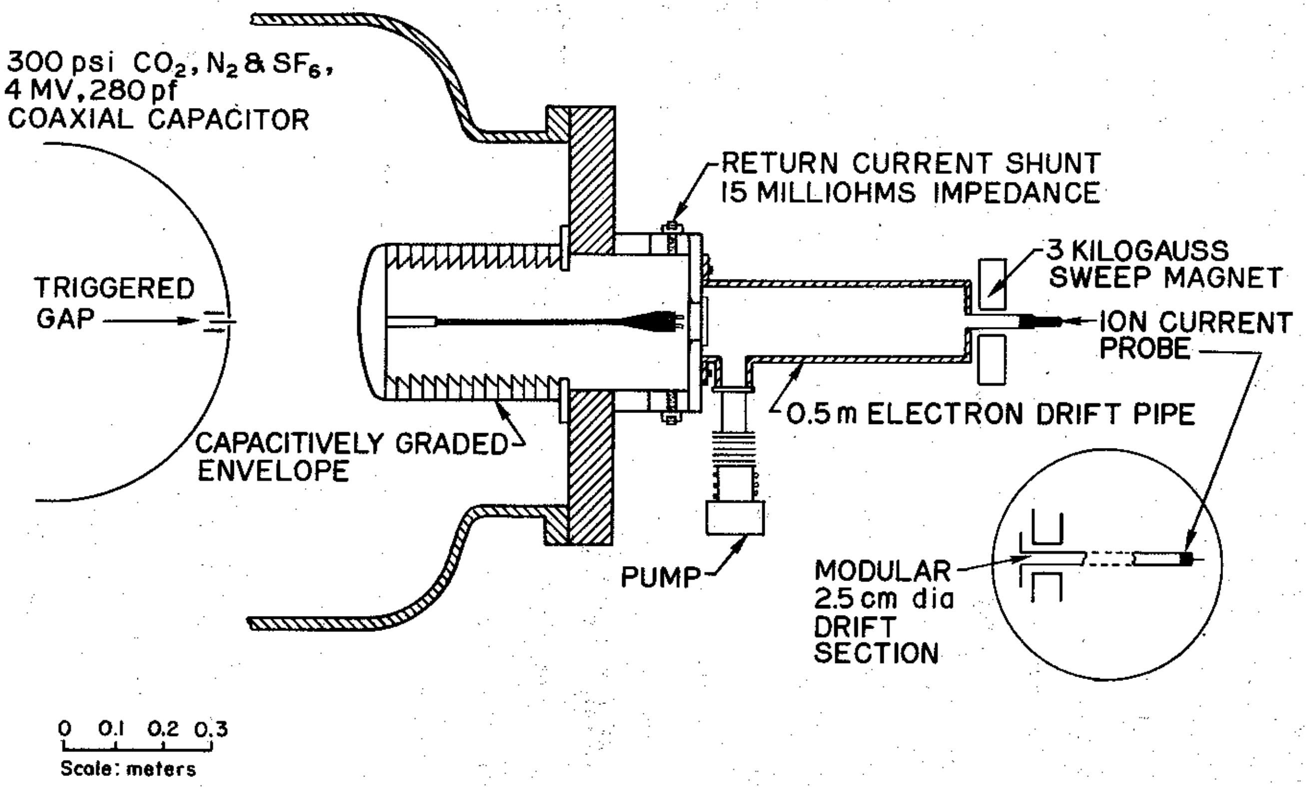

Figure 58. Experimental Arrangement for Beam Plasma Ion Detection

had a very small spread (typically ± 1 ns). The time of flight determination was obtained by measuring arrival times at three different locations.

The results of the time of flight experiments are summarized in Figures 59 and 60. Note that two time references were checked, namely the leading edge of the ion current pulse and also the peak of the ion current pulse. There is a slight difference in the spread in ion velocity versus pressure for the two ways of analyzing the data, but in general the results are consistent. It should also be noted that each data point represents the average value of arrival time of two or three separate measurements.

The results show that, for helium and nitrogen, the ion energy is not pressure dependent over the range of pressure studied, while hydrogen and deuterium do exhibit a dependence of ion energy on pressure. The plots shown in Figure 61 make this more apparent.

The improved timing for these measurements was achieved by adding TDR measured delay cables into the trigger cable for the oscilloscope used to measure ion current. This scope is generally swept at 5ns/cm. The reference signal was always taken to be the output of the current monitor used to measure the diode current. Figure 62 shows representative proton current signals obtained using this timing scheme. Note the high current (~ 250 A) and short pulse width (~ 3 ns FWHM) obtained. Figure 63 shows representative ion current signals for the various ion species studied.

### 4.2.3 Range-Energy Measurements

While the time-of-flight results described above clearly indicate that there are energetic ions produced by the beam-plasma system, there was some concern that we had not positively identified the ion species actually accelerated. To establish the identity of the accelerated ions, range measurements were made for the various filling gases used. The experimental configuration used was the same as in Figure 58. An aluminum foil absorber of varying thickness was placed in front of the Faraday current collector and plots of relative transmitted signal versus absorber thickness were obtained.

1-4486

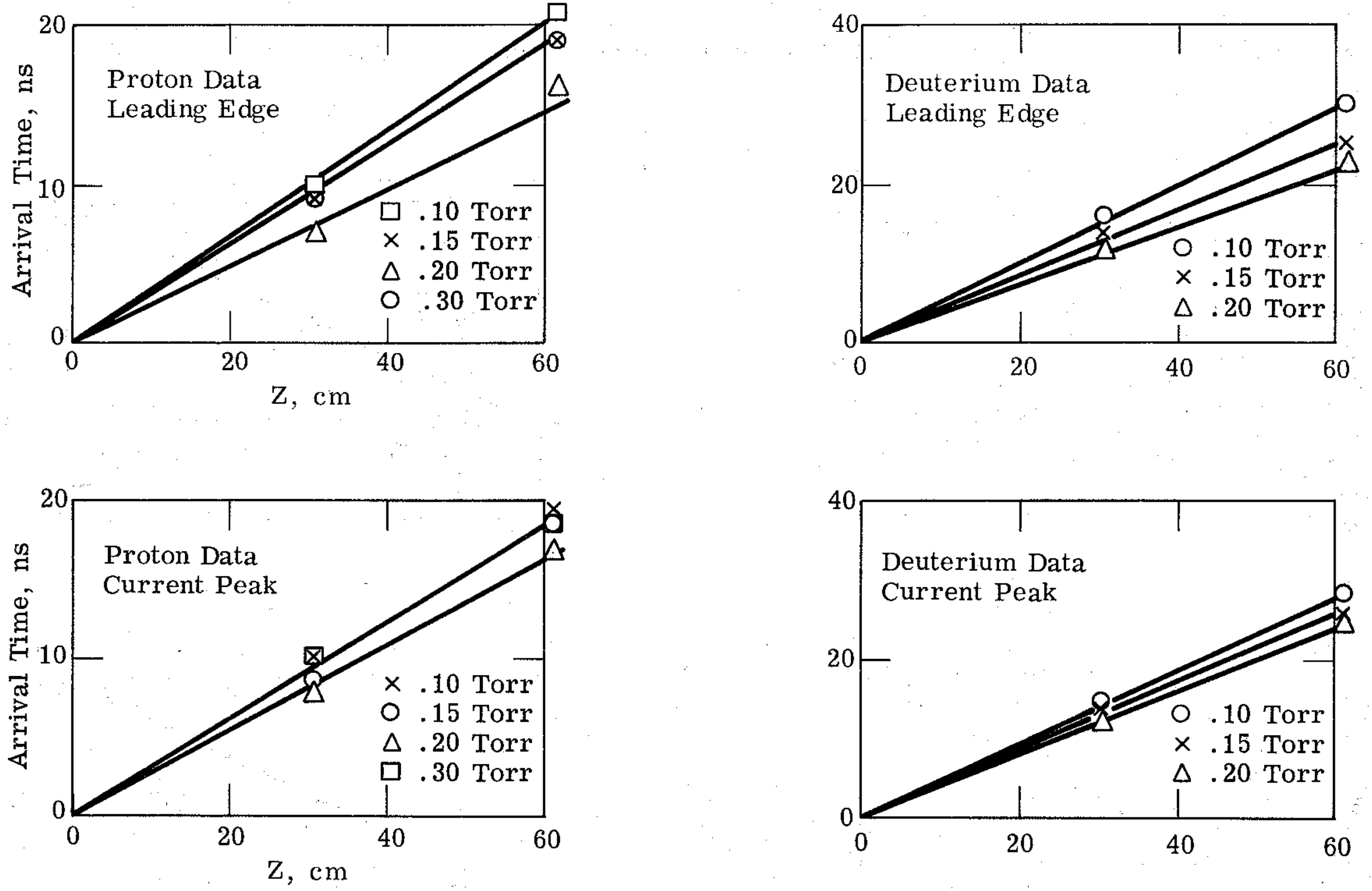

Figure 59. Ion Time of Flight - Hydrogen and Deuterium

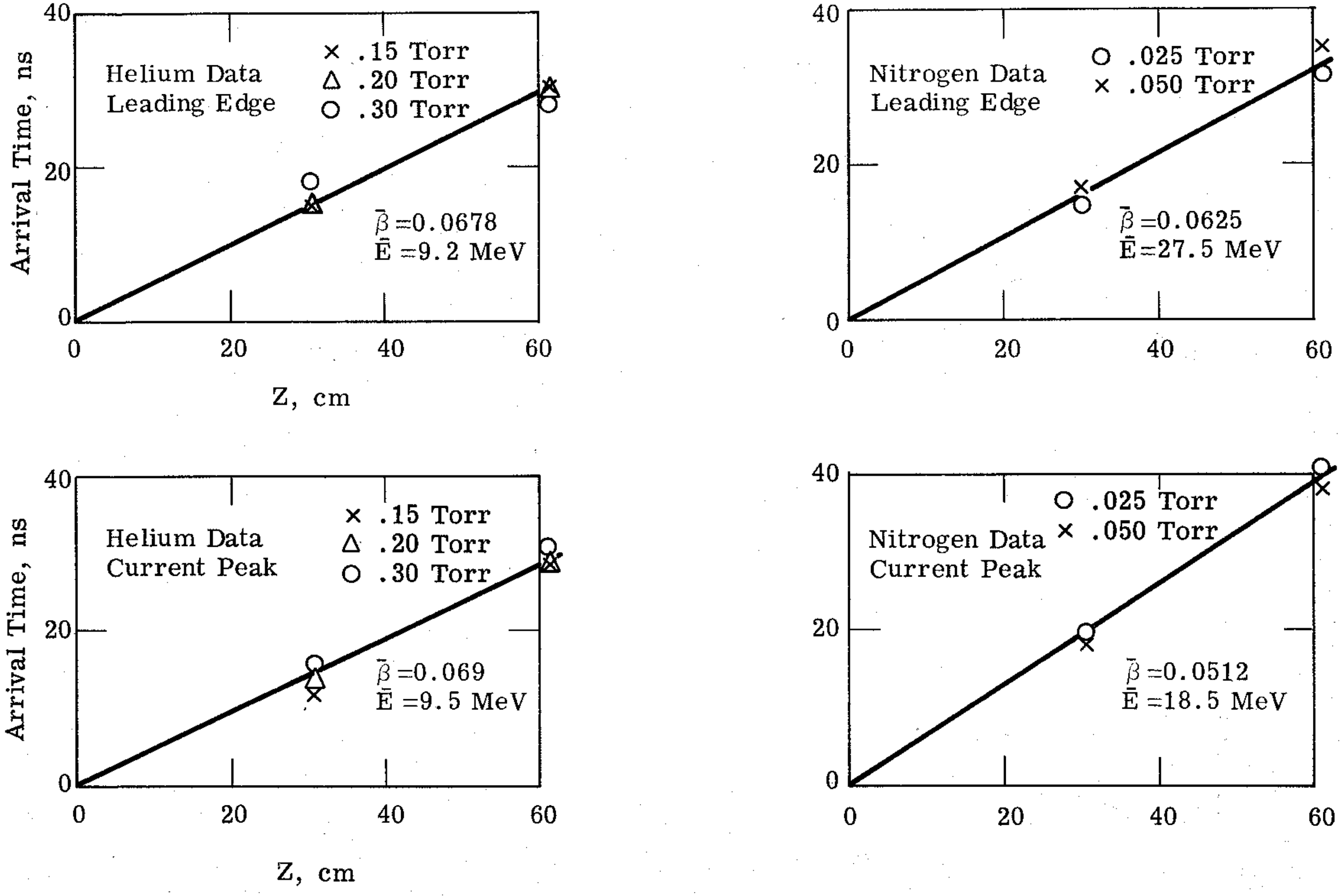

Figure 60. Ion Time of Flight - Helium and Nitrogen

1-4487

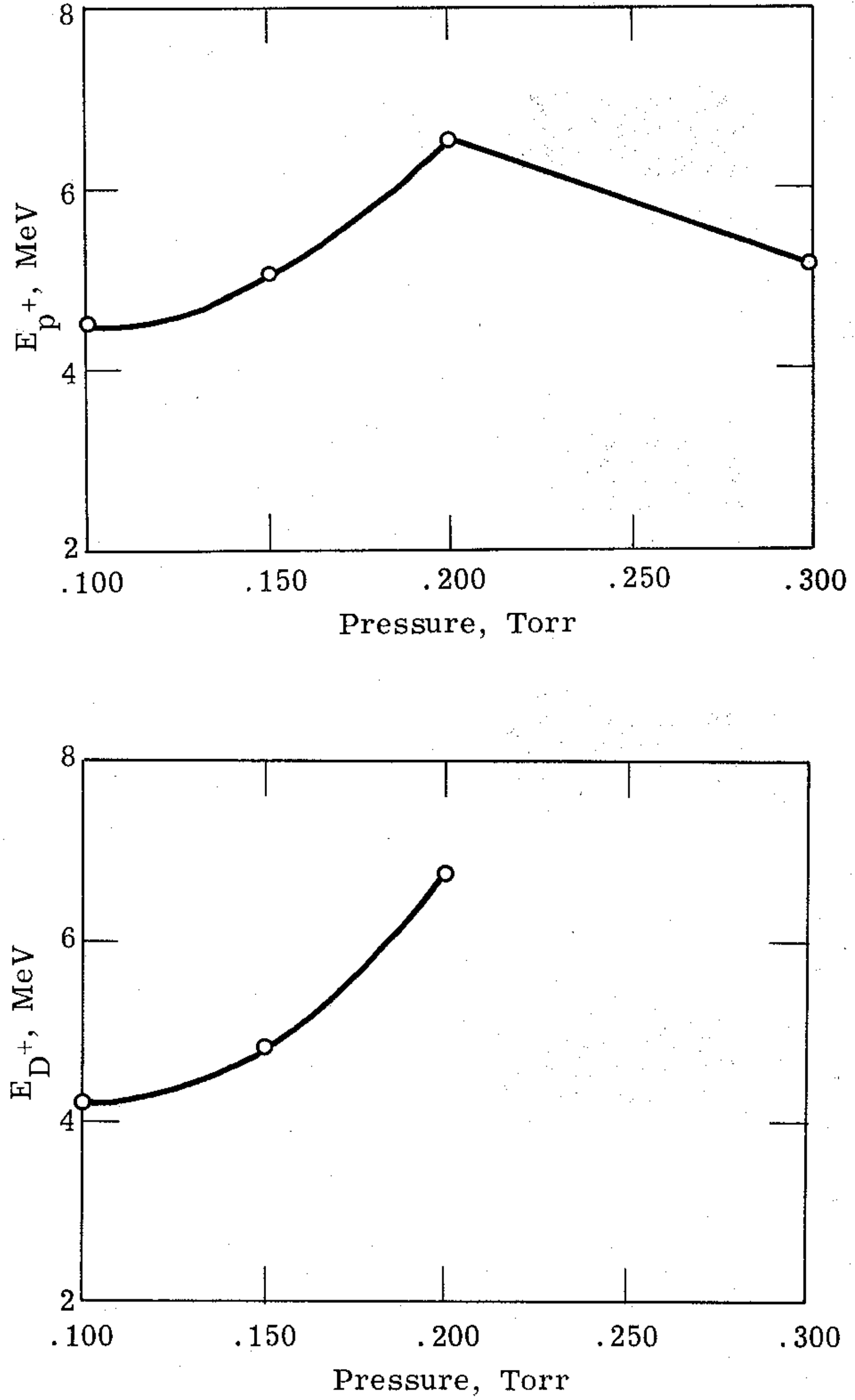

Figure 61. Pressure Dependence of Proton and Deutron Energies

1-4488

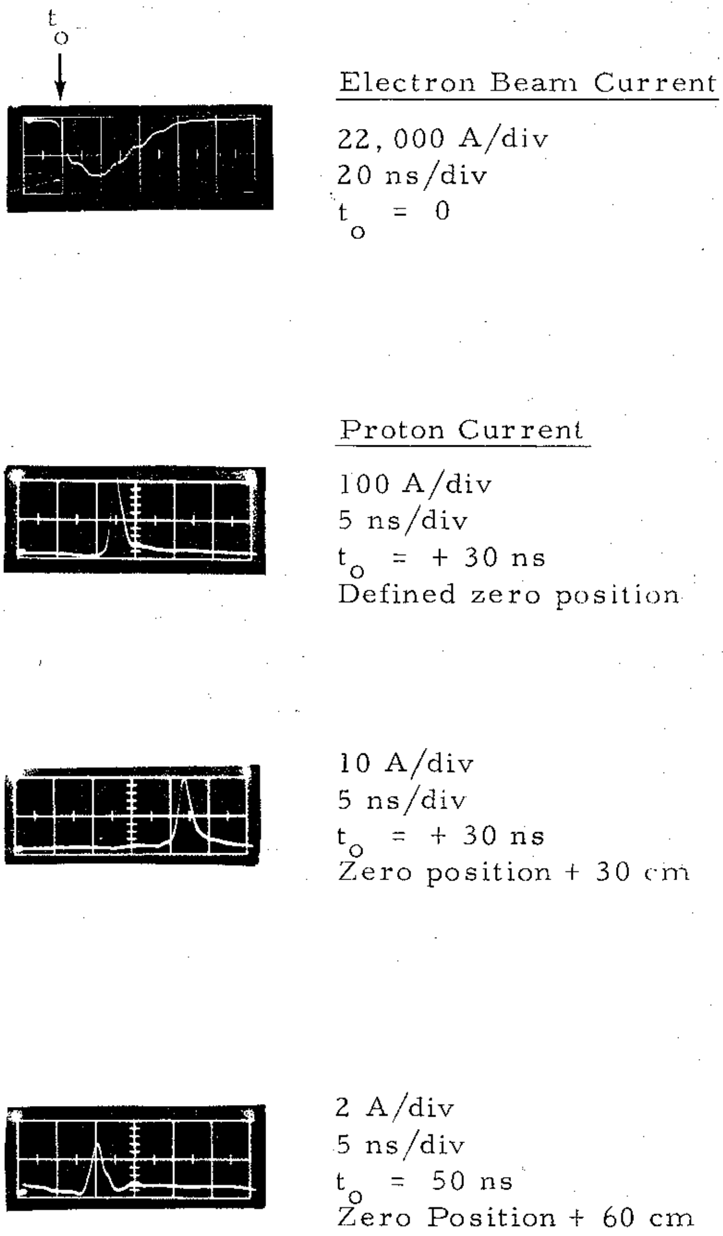

Electron Beam Current

22,000 A/div
20 ns/div
$t_o = 0$

Proton Current

100 A/div
5 ns/div
$t_o = +30$ ns
Defined zero position

10 A/div
5 ns/div
$t_o = +30$ ns
Zero position + 30 cm

2 A/div
5 ns/div
$t_o = 50$ ns
Zero Position + 60 cm

Representative Proton Flight Time Data
(Carbon Cathode)

Figure 62

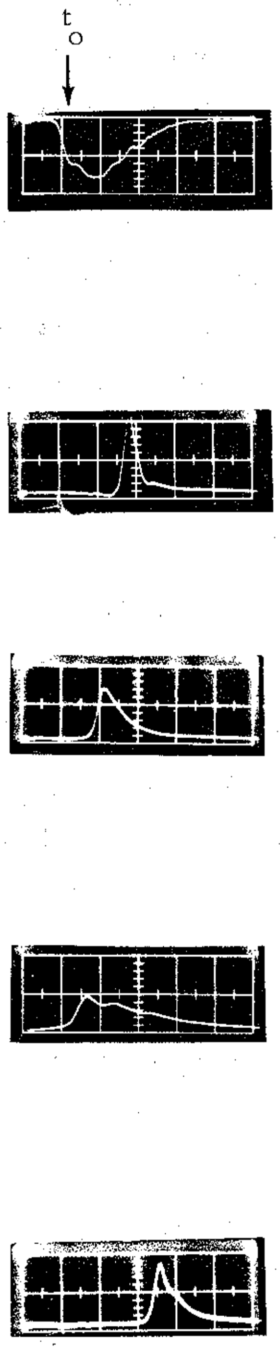

Electron Beam Current

22,000 A/div
20 ns/div
$t_o = 0$

Ion Current

Hydrogen - 0.15 Torr
100 A/div
5 ns/div
$t_o = + 30$ ns

Deuterium - 0.15 Torr
100 A/div
5 ns/div
$t_o = + 40$ ns

Helium - 0.20 Torr
20 A/div
5 ns/div
$t_o = + 45$ ns

Nitrogen - 0.025 Torr
10 A/div
20 ns/div
$t_o = 20$ ns

Representative Ion Pulses (Carbon Cathode)

Figure 63

Figure 64 shows a plot of energy versus range in aluminum for various ions. Note that for a given range there is a large spread in energy for the various ions. If the range measurements of ion energy agree with the energy calculated from the time-of-flight data, by assuming the ion mass is equal to the atomic mass of the filling gas, then it is safe to say that only those ions are present which correspond to the filling gas. Figure 65 shows the results of the range measurements. The energies derived are in good agreement with the time-of-flight results. This establishes that only ions corresponding to the filling species are accelerated.

### 4.2.4 Momentum Analysis Measurements

Since all of the mechanisms proposed to explain the acceleration process depend in some way on the charge state of the ion, a magnetic analysis of the momentum of the ions was carried out to determine the charge state. The results also help establish the mass (species) of the ion.

The experimental configuration used is shown in Figure 66. A thin slit (1 mm x 5 mm) was placed in front of the entrance to the small drift section extending out from the main drift tube. The smaller drift section was differentially pumped down to a good vacuum ($10^{-5}$ Torr range). As shown, part of this drift section consisted of a curved section (1.7 meter radius of curvature) placed inside the field of an electromagnet. Any electrons entering the system are swept out by this magnetic field.

After passing through the magnetic field region, the ions must pass through another slit which is used to increase the resolution of the system. A solid state detector was used to measure the amount of ion beam transported through the system. The magnetic field is varied by changing the driving current to the magnet, and by changing the field on each shot one can sweep through a P/Q range and determine what charge states are present (since the ion velocity is known from time of flight measurements). The relations of importance are

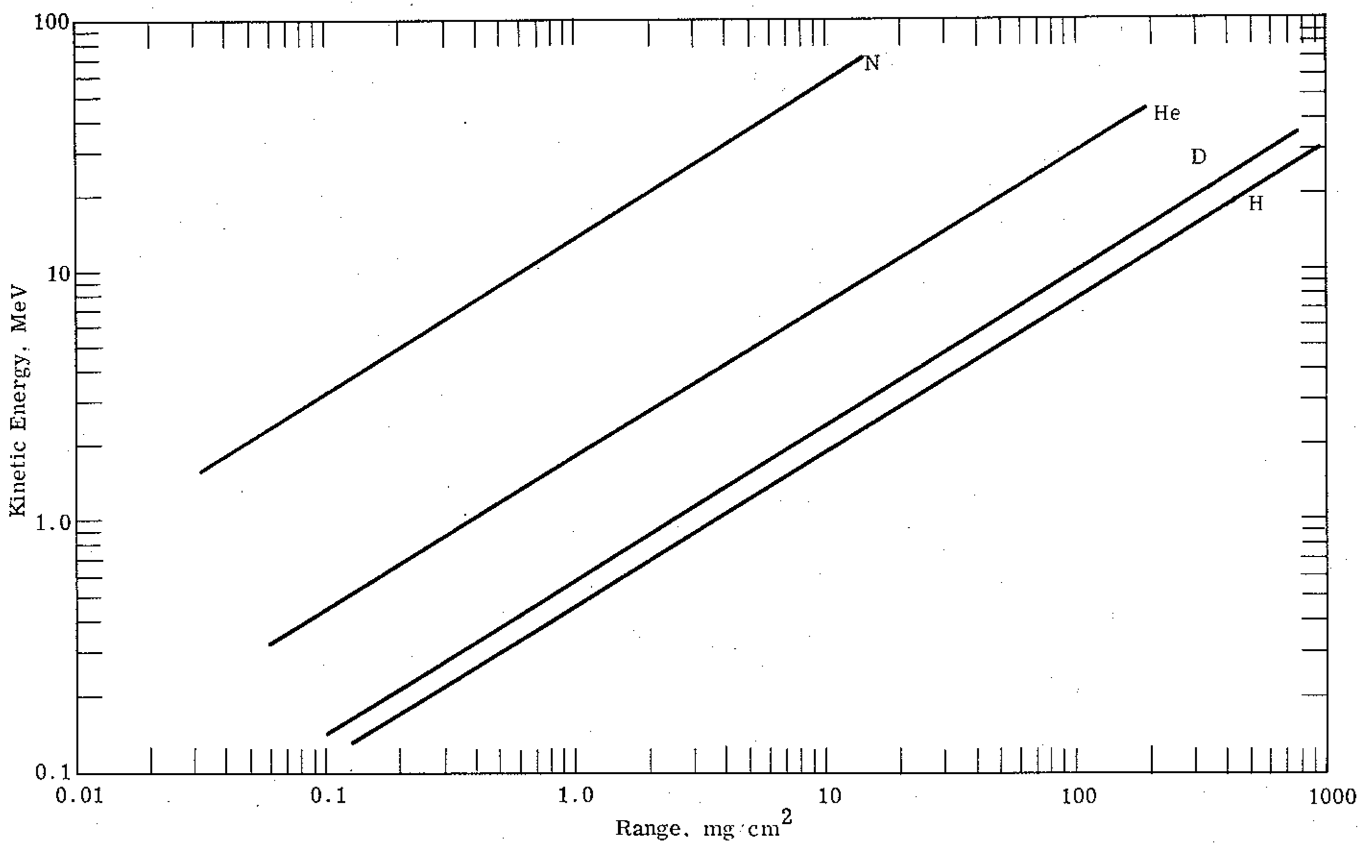

Figure 64. Range-Energy Curves for Various Ions in Aluminum

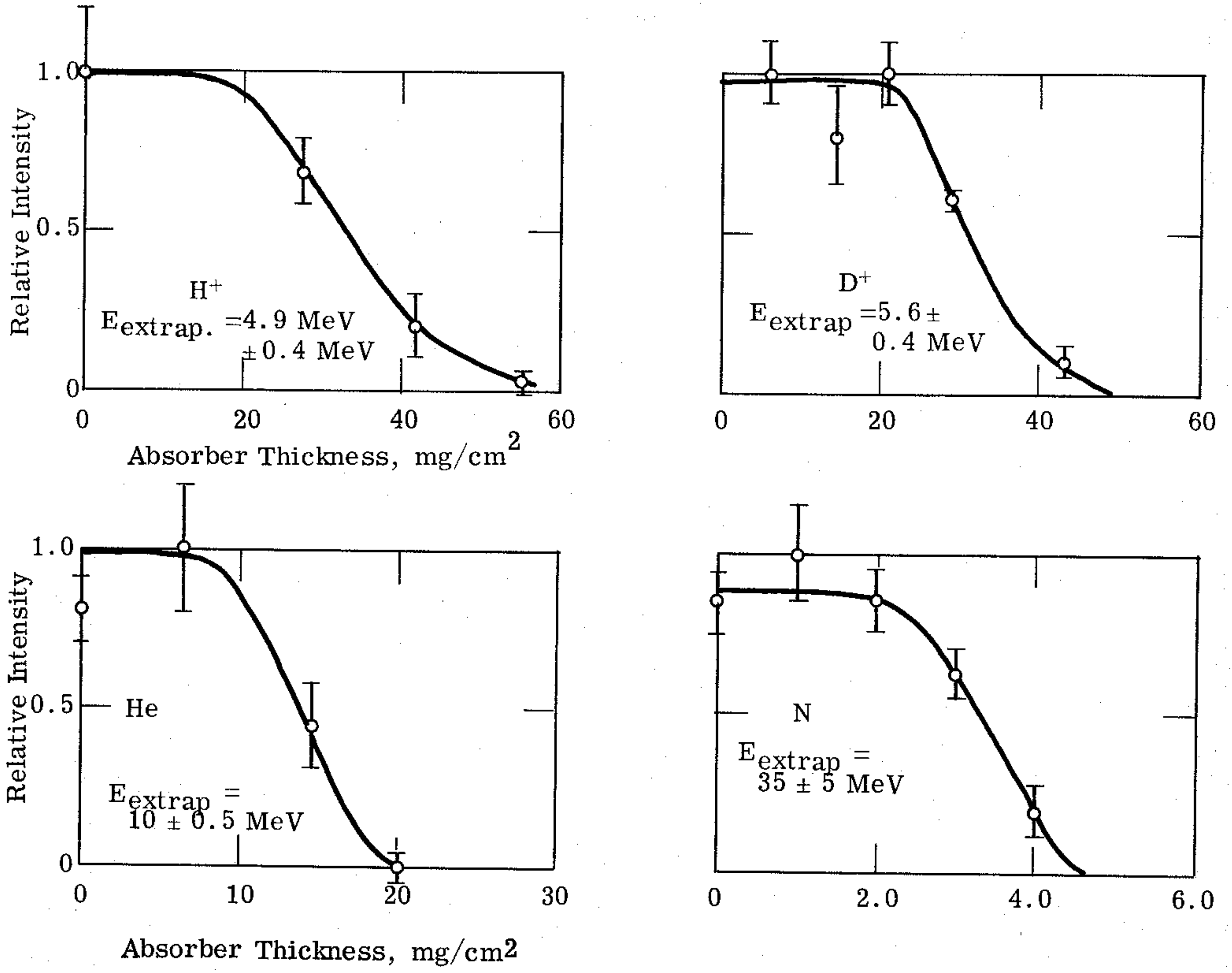

Figure 65. Range Measurements of Collectively Accelerated Ions

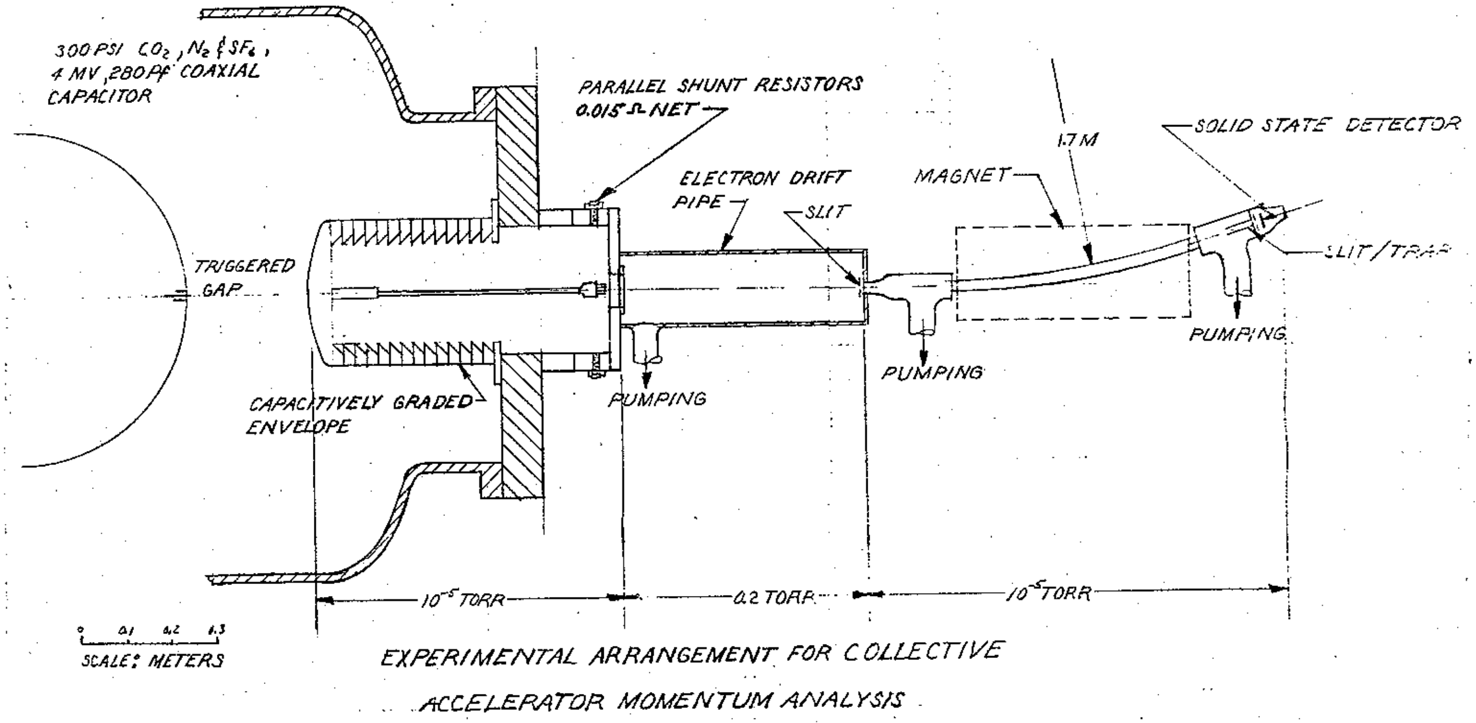

Figure 66. Experimental Arrangement for Collective Accelerator Momentum Analysis

$$\frac{P}{Q} = k_1 B$$

$$B = k_2 I$$

where:

$P$ = momentum of ion = $MV$

$Q$ = charge state of ion (degree of ionization)

$B$ = magnetic field

$I$ = magnet current

and $k_1$ and $k_2$ are two constant coefficients.

The experimental results are shown in Figure 67. The hydrogen data was used to calibrate the system. The arrows on the other plots show where the indicated species' charge state should occur given the hydrogen calibration. The deuterium and helium data prove that only the filling gas specie is present, and for helium the indication is that only completely ionized atoms are accelerated. The nitrogen data shows that highly stripped ions are formed, with the main contribution coming from six-times ionized nitrogen.

### 4.2.5 Neutron Yield Measurements

Studies were made of the neutron yields obtainable from the accelerated ion beams using Be (x, n) reactions. Protons, deuterons, and helium ions were allowed to impinge on a beryllium plate located on the blank-off plate at the end of the main drift tube. A total neutron yield detector of the Los Alamos type was used to measure the yield. The results shown in Figure 68 indicate that

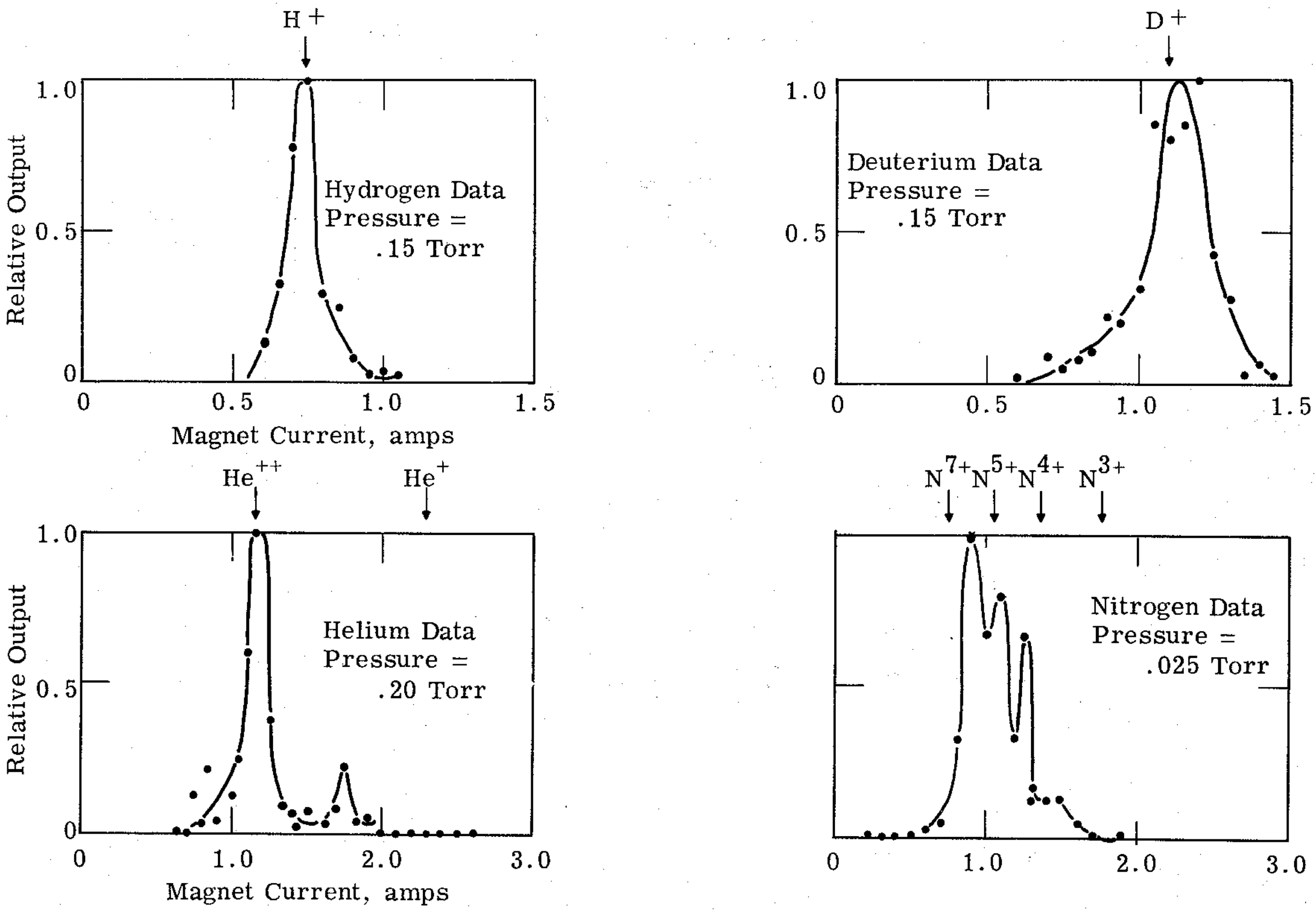

Figure 67. Magnetic Analysis Data for Various Ions

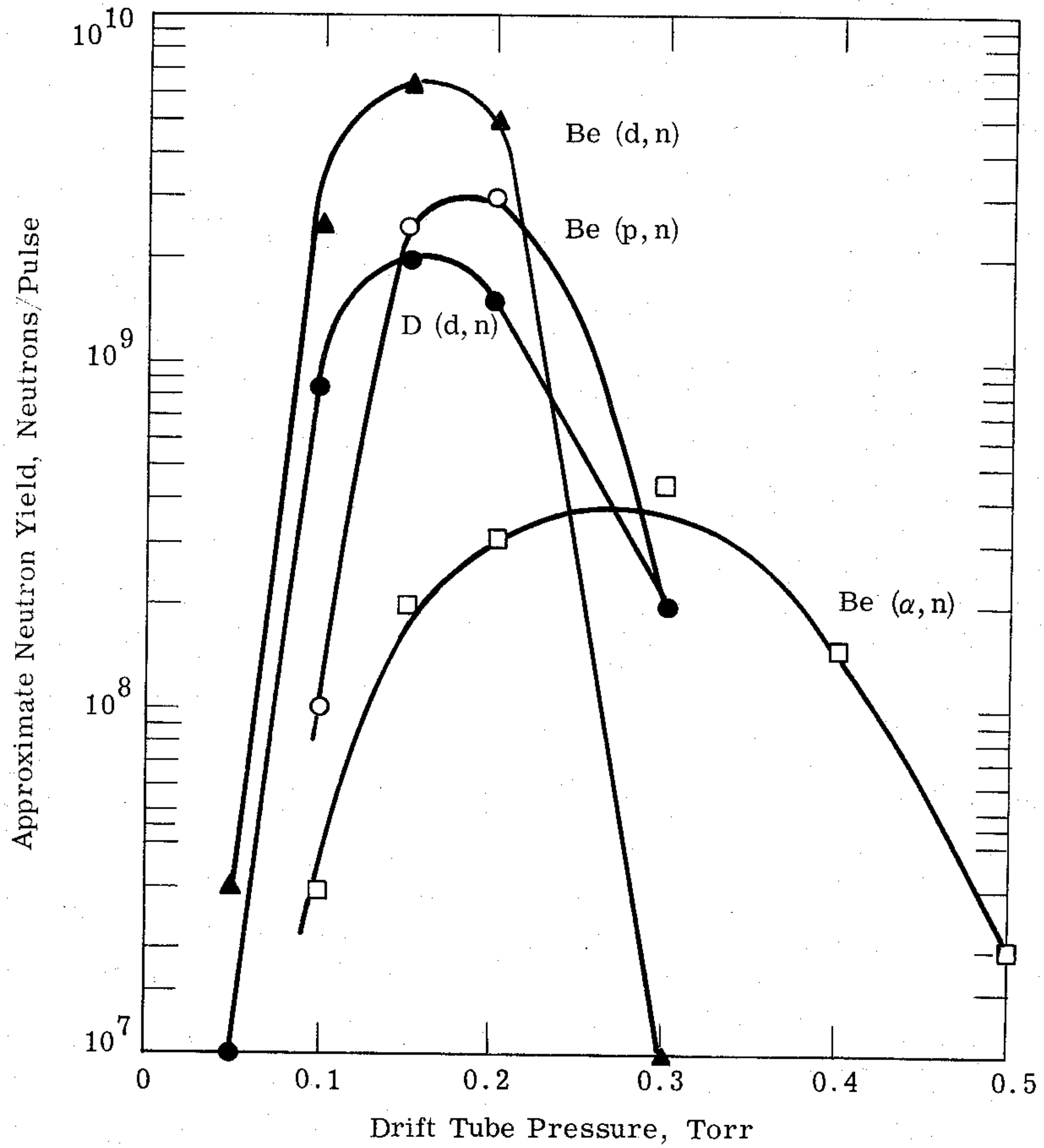

Figure 68. Neutron Yield versus Pressure Data

something approaching $10^{10}$ neutrons/pulse is attainable. Since the angular distribution is largely peaked in the forward direction, and the source size is a few $cm^2$, fluences of the order of $10^9$ $n/cm^2$ of high energy (> 1 MeV) neutrons are achievable. The neutron pulse lengths are known to be of the order of 100 ns, so that the flux level approaches $10^{16}$ $n/cm^2$ - sec).

### 4.2.6 Drift Tube Length Variation

One important experimental program which was carried out was the determination of the influence of drift tube length on the acceleration process. The experimental configuration was the same as in Figure 58, but the length of the main drift tube was varied from 20 cm to 100 cm. The time of arrival of the ion pulse at the end of the drift tube was measured, at different pressures and lengths, and the results are shown in Figure 69.

From Figure 69 it is clear that after the drift tube is greater than about 30 to 40 cm in length that ions travel with a constant velocity, while for lengths shorter than this there is a reduction in velocity. It will be shown below that this result is predicted by the accelerated potential well model, developed to explain our results.

### 4.2.7 Accelerated Potential Well Model

The physical model which was developed to explain the acceleration of ions by linear electron beams relied heavily on experimental results for guidance. For example, the results of Figure 70 indicated that no acceleration took place until the electron beam was force neutralized. The result of beam front propagation measurements, shown in Figure 16, indicate that by the time force neutralization has occurred the beam front has been long since intercepted by the drift tube blank-off plate. Thus, any potential well associated with the beam front is not responsible for ion acceleration. Finally, the photographs of Figure 57 indicate that after force neutralization the electron beam propagates in a reasonably well-defined cylinder (of radius ≈ 1 cm), while calorimetric measurements indicate that the beam current density is roughly constant across any portion of the beam.

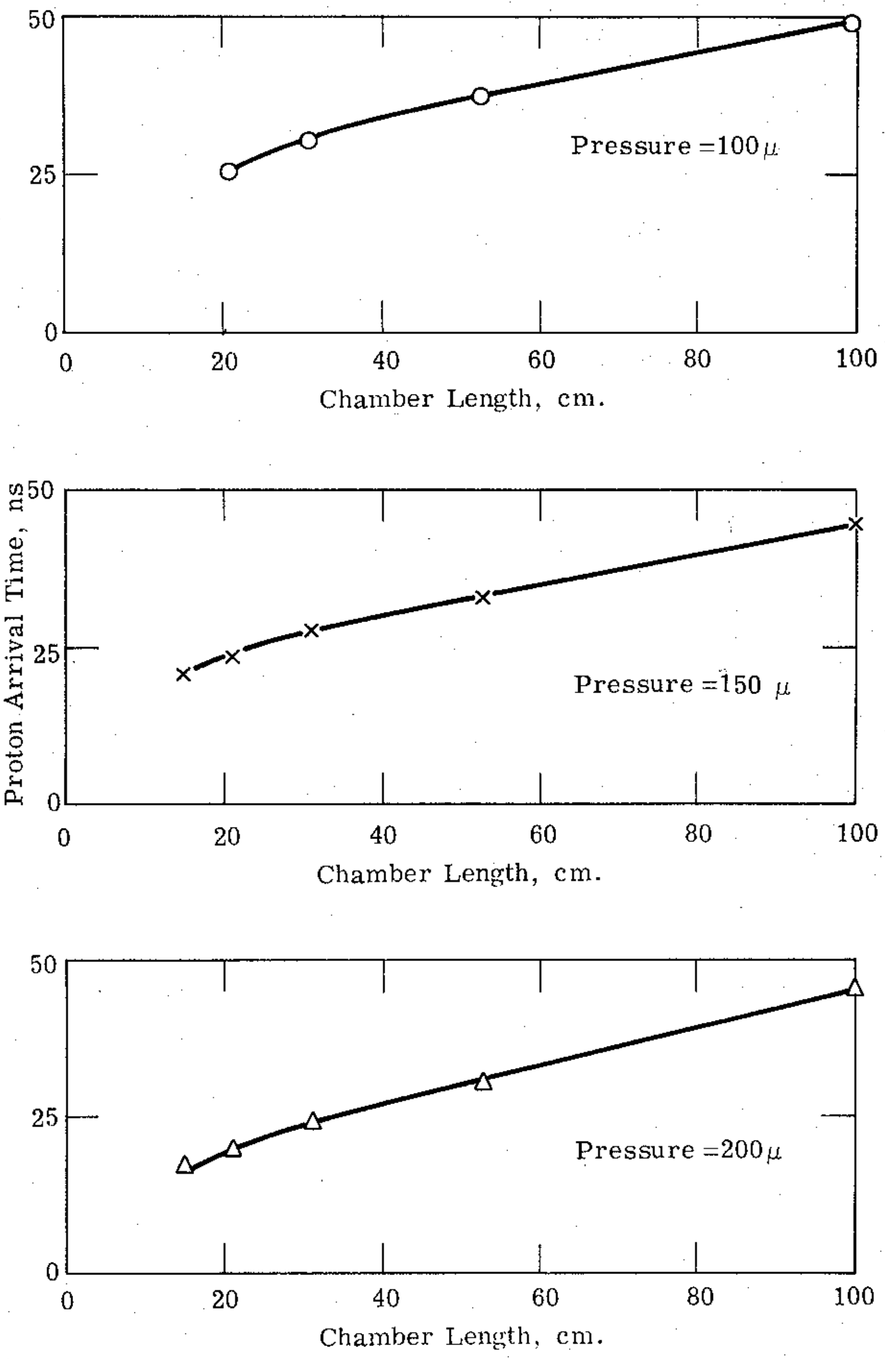

Figure 69. Beam Front Time of Flight Data

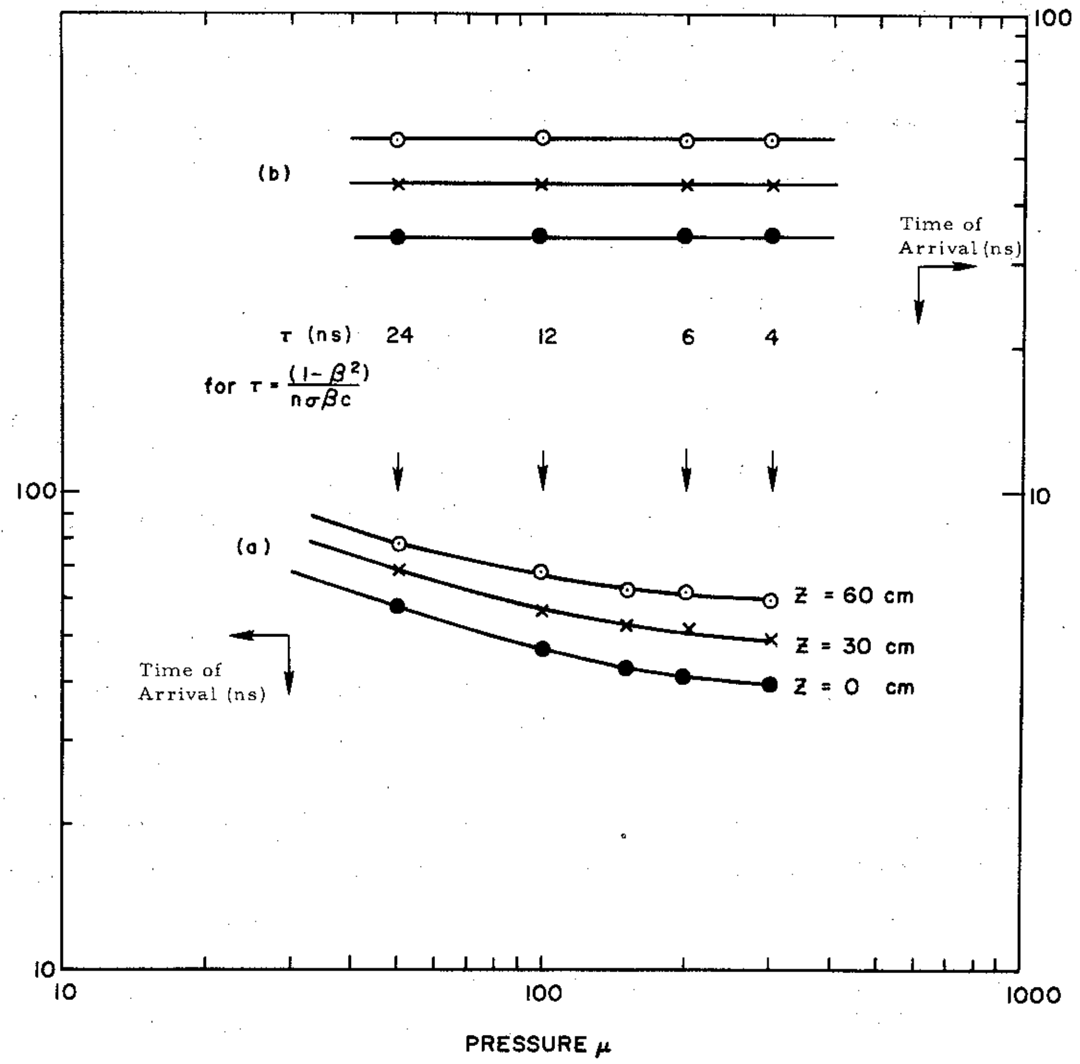

Figure 70. Dependence of Hydrogen Ion Arrival Time on Ambient Pressure

The model which was developed is really a qualitative one, since not enough detailed calculation has been done to refine the estimates given below. Nonetheless, even this crude description gives remarkably good agreement with experimental results. We have the following properties of a beam which has just become force neutralized:

- (a) the injection energy is ~ 1.5 MeV
- (b) the current density is ~ $10^4$ A/cm$^2$
- (c) the beam radius is ~ 1 cm
- (d) the beam is inside a grounded, enclosed cylinder of radius a and lengths L
- (e) the fractional space-charge neutralization is small (~ 10%)
- (f) the beam extends from one end of the drift tube to the other, with a uniform charge density out to a radius b = 1 cm.

Consider now the geometry shown in Figure 71. A beam is shown inside a closed cylinder of radius a, the beam radius being b. A length of the beam, A, is assumed space charge neutralized, while the remaining length is not neutralized. A static solution for the potential field inside the cylinder can be found using cylindircal Greens functions. Figure 72 shows the potential, on axis, for the beam under consideration when it has just become force neutralized, i.e. A = O. The main features to note are:

- (a) the well depth is ≈ 1 MeV
- (b) the distance over which the potential goes from zero to its maximum depth is ≈ 5 cm.

In the region near z = o there is a large longitudinal electric field, of the order of 200 kV/cm. Any secondary electrons produced in this region will be accelerated back to ground, and in particular an avalanche breakdown of the gas can occur. From Figure 73 we can estimate the time necessary to accomplish the breakdown for helium gas at 0.2 Torr. The time is:

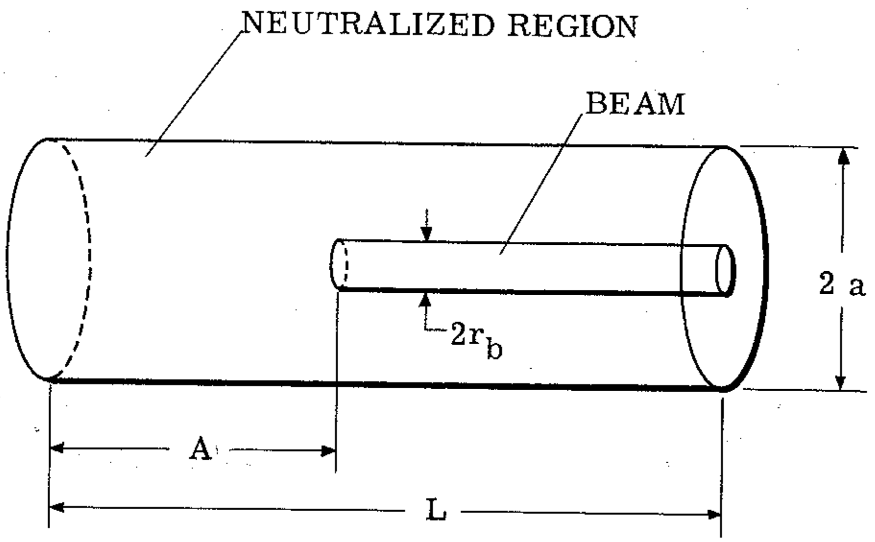

Figure 71. Beam-Drift Tube Geometry

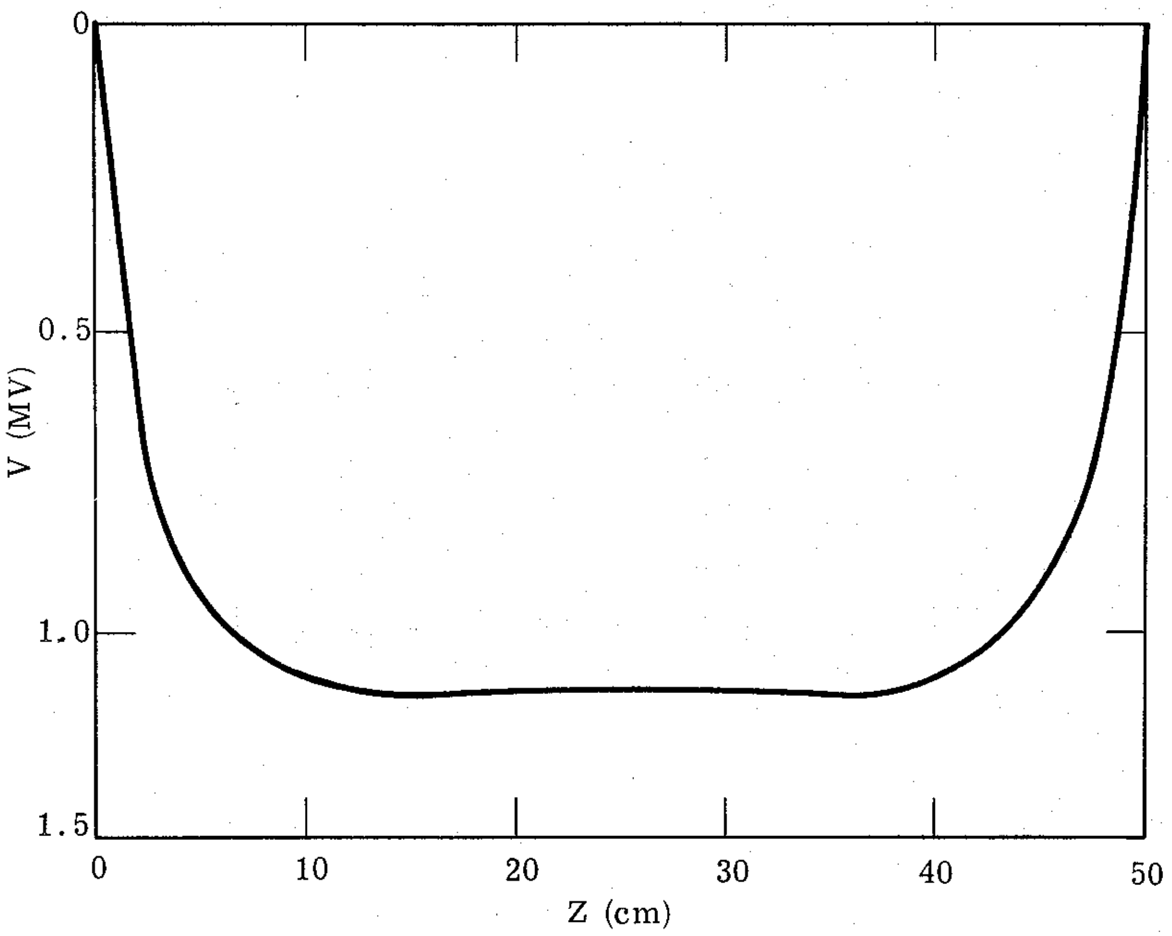

Figure 72. Potential Along Axis of Drift Tube
A = 0.0

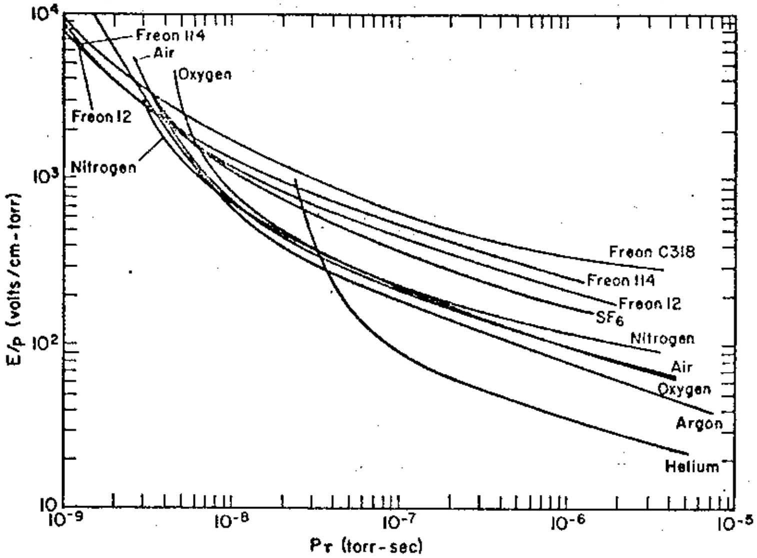

Figure 73. Breakdown Curves for Nine Test Gases (From P. Felsenthal and J. Proud, Phys. Rev. 139, A1796, (1965)).

$$\tau \approx 15 \text{ ns}$$

when a linear extrapolation of the data Figure 73 is made. The region of charge neutralization is now A ≈ 10 cm, and the new potential distribution is roughly as shown in Figure 74. The net effect is that the potential well has been "accelerated" through a distance of about 10 cm in 15 ns. The acceleration rate, $A_o$, of the well is then

$$1/2\, A_o\, \tau^2 \approx 10 \text{ cm}$$

or

$$\frac{A_o}{c} = \frac{d\beta_o}{dt} \approx 3 \times 10^{-3}/\text{ns}$$

Consider now the ideal problem shown in the figure below:

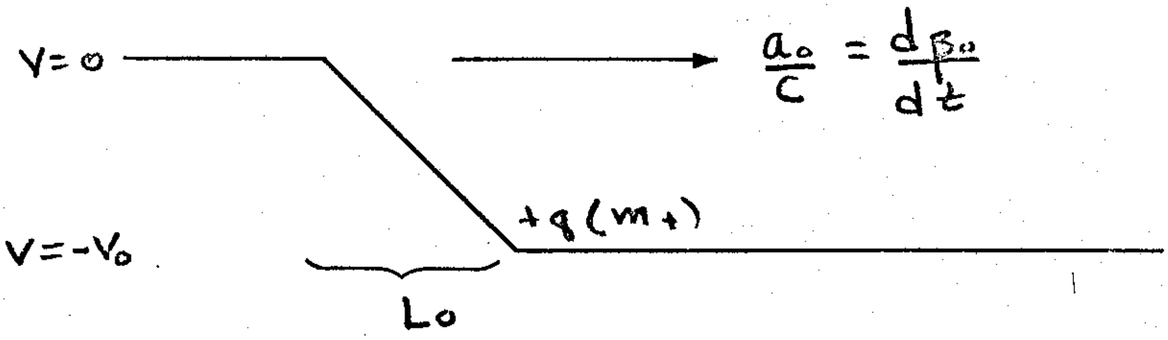

A particle created at the bottom of the well feels a force exerted on it as the potential well is accelerated to the right. The formula giving the energy gained by the particle after the well has passed it is:

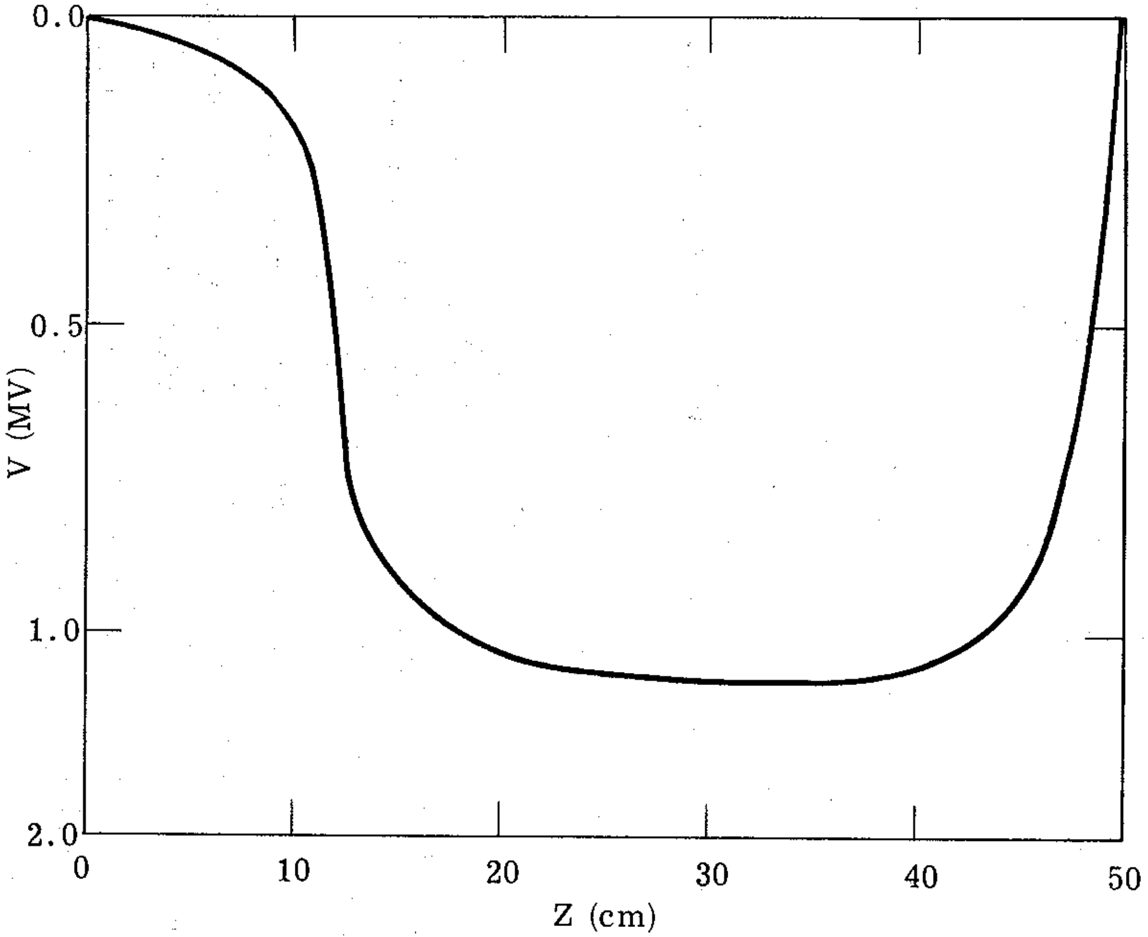

Figure 74. Potential Along Axis of Drift Tube
A = 12.5 cm

$$\frac{E+}{qV_o} = \frac{1}{\eta \frac{d\beta_o}{dt} \tau_o - 1}$$

where:

$$\eta = \frac{M_+ c^2}{qV_o}$$

and:

$$\tau_o = \frac{L_o}{C}$$

Using $He^{++}$ $V_o \approx 1$ MV, $L_o \approx 10$ cm, and the fact that $E_{He^{++}} \approx 10$ MeV, we find

$$\frac{d\beta_o}{dt} \approx 2 \times 10^{-3}/\text{ns}$$

Thus, these crude estimates indicate that an avalanche-type process is probably the reason the potential well is "accelerated".

Another property which tends to favor the accelerated potential well model is the fact that ion energies scale like the charge, a fact which has been demonstrated experimentally. Finally, the model would predict that roughly 35 cm of path length is necessary to bring the ions up to full energy. This agrees well with the results shown in Figure 69.

# SECTION 5

# BEAM PROPAGATION THEORY

## 5.1 Beam Front Propagation Velocity

A limit to the speed with which the electron beam front can propagate is the rate at which energy is supplied to the system. The source of energy is the kinetic energy supplied by the accelerator at the entrance aperture to the drift tube. This energy is then divided between magnetic field energy and beam kinetic energy. The geometry of the beam-drift tube system determines how efficiently energy from the accelerator is used and how fast the beam front propagates. The most efficient system would have no stored magnetic energy; in this case the velocity of the electrons at the entrance aperture would be the velocity of the beam front.

It is useful before performing a maximum beam front velocity calculation as determined by energy rates to examine some cases to see how efficiently they divide energy. To this end, the ratio of magnetic field energy to particle kinetic energy will be calculated for two cases.

- Case 1 - Uniform beam filling a drift tube.

The magnetic field energy/unit length for this case is as follows:

$$\mu = \frac{1}{2\mu_o} \int_o^{r_b} B_\Theta^2 \; 2\pi r \, dr \tag{1}$$

where:

$$B_\Theta = \frac{\mu_o I r}{2\pi r_b^2} \tag{2}$$

Integrating,

$$\mu = \frac{\mu_o}{4\pi} \frac{I^2}{r_b^4} \int_o^{r_b} r^3 dr = \frac{1}{4} \frac{\mu_o}{4\pi} I^2 \tag{3}$$

The particle energy per unit length is:

$$\mu_p = (\gamma - 1) mc^2 N = (\gamma - 1) \frac{mc^2}{e} \frac{I}{\beta c} \tag{4}$$

where N = number of electrons/unit length. The ratio is

$$\frac{\mu}{\mu_p} = \frac{1}{4} \frac{\mu_o}{4\pi} I^2 \beta c/(\gamma - 1) \frac{mc^2}{e} = \frac{I}{17,000} \frac{(\gamma + 1)^{1/2}}{4\gamma(\gamma - 1)^{1/2}} \tag{5}$$

For I = 40 k A, $\gamma = 4$ (1.5 MeV), this ratio is

$$\frac{\mu}{\mu_p} = 0.2.$$

Thus the case wherein the beam fills the drift tube is a fairly efficient user of energy; however the ratio increases linearly with current so that for a megampere at the same initial energy the magnetic field energy would be five times the beam energy per unit length, if such a beam would propagate at all.

- Case 2 - Uniform beam partially filling a drift tube

  For this case the magnetic field energy is calculated as follows:

$$\mu = \frac{1}{2\mu_o} \int_o^{r_b} B_\Theta^2 \, 2\pi r dr + \frac{1}{2\mu_o} \int_{r_b}^{r_c} B_\Theta^2 \, 2\pi r dr \tag{6}$$

where:

$$B_4 = \frac{\mu_o I r}{2\pi r_b^2} \quad \text{for} \quad r < r_b$$

and

$$B_4 = \frac{\mu_o I}{2\pi r} \quad \text{for} \quad r > r_b$$

The ratio of field to particle energy is then:

$$\frac{\mu}{\mu_p} = (1 + 4 \ln r_c/r_b) \frac{I}{17,000} \frac{(\gamma + 1)^{1/2}}{4\gamma(\gamma - 1)^{1/2}} \tag{7}$$

For I = 40 k A, $\gamma = 4$, and $r_c/r_b = 5$, this ratio is:

$$\frac{\mu}{\mu_p} = 1.5$$

For a megampere at the same voltage the ratio is:

$$\frac{\mu}{\mu_p} = 37.5$$

Again this high current beam would not propagate in this mode because of over pinching, but even if it could, too much energy would be tied up in fields to make it useful.

It is obvious that for any of these cases plasma return current either in the beam or outside it serve to reduce the magnetic field and hence the amount of field energy.

The beam front velocity can be calculated based on a power flow argument. The sum of the rate of change of magnetic field energy plus the rate of increase of particle kinetic energy must equal the power influx to the drift tube. For this calculation a very sharp beam front is envisioned. The power balance equation is, for the case of a beam partially filling a drift tube, as follows:

$$VI = 1/4 \, \frac{\mu_o}{4\pi} \, I^2 \, (1 + 4 \ln r_c/r_b) \, \beta_z \, c + (\gamma - 1) \, \frac{mc^2}{e} \, I \tag{8}$$

I is the injection current which has been accelerated by a potential V. $\beta_z$ and $\gamma = 1/(1 - \beta_z^2)^{1/2}$ pertain to the beam in the drift tube.

Rearranging the above equation obtains the following:

$$V + \frac{mc^2}{e} - \frac{\gamma mc^2}{e}^2 = I \, \frac{Z_o^2}{16\pi} \, (1 + 4 \ln r_c/r_b)^2 \, \frac{\gamma^2 - 1}{2} \tag{9}$$

where:

$$Z_o = 377 \text{ ohm}$$

For the case V = 1.5 MV, I = 40 k A, $r_c/r_b = 5$, this equation determines $\gamma$ to be:

$$\gamma = 1.3$$

This in turn yields for $\beta$:

$$\beta = \frac{1}{\gamma}\sqrt{\gamma^2 - 1} = 0.63$$

## 5.2 Electric Field at Beam Front

The above discussion found a value for the beam front propagation velocity without saying anything about how the initially fast electrons were slowed down from $\beta_{zo} = .9$ to $\beta = 0.63$. The mechanism is of course the induced electric field in the z direction due to the increasing magnetic field. In this section we derive a formula for this field on the beam axis.

The induced electric field may be most easily calculated using Faraday's law and the contour shown in Figure 75.

$$\int E \, d\ell = - \frac{d}{dt} \int \phi \, ds$$

$$E_z(r = o) = \frac{-\mu_o}{2\pi} \frac{\partial J}{\partial t} \int_o^{r_b} r \, dr$$

where we have used

$$B_\phi = \frac{\mu_o J}{2} r$$

$$E_z(r = o) = - \frac{\mu_o}{4} r_b^2 \frac{\partial J}{\partial t}$$

$$E_z(r = o) = - 10^{-7} \frac{dI}{dt} \qquad (10)$$

If the beam is envisioned as having a very sharp front, then $\frac{dI}{dt}$ will be very large and the front of the beam will experience very strong fields. The front electrons would be slowed down so much that they would be overtaken by the back electrons. This procedure would have to take place in such a way that the beam front would proceed according to the limit imposed by input power flow derived in the previous section.

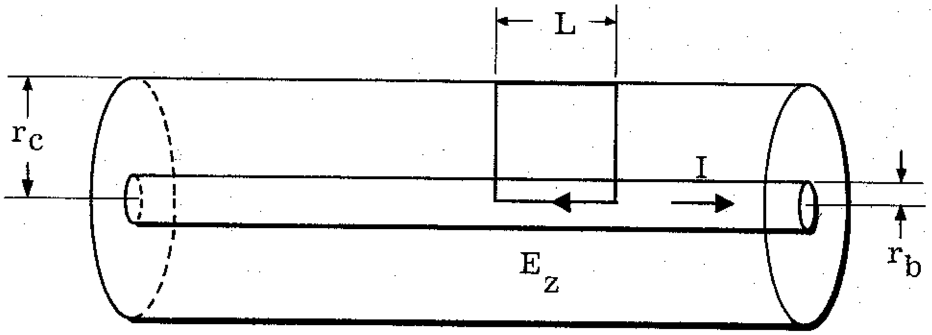

Figure 75. Schematic for Electric Field at Beam Front

More typically the beam front is not really sharp, but has a risetime on the order of 10 ns; e.g. for a 40 k A beam then

$$E_z = - 10^{-7} \frac{.4 \times 10^4}{10^{-8}} = .4 \text{ MV}/_m$$

which says that electrons at the beam front would be slowed appreciably only after traveling a fraction of a meter. Again faster electrons at the rear would overtake the front electrons only to be slowed down as they become the leaders, also the beam front velocity will be limited to $\beta = 0.63$ (for the 40 k A, 1.5 MV case).

If the beam were injected into a preformed plasma the conductivity of the plasma would short the electric field. In such a case the previous analysis would not apply and the beam front velocity would be greater than the limit imposed by equation (9) depending, essentially, on ambient gas pressure. If the time for ionization sufficient for magnetic neutralization is long compared to the current risetime, then the beam velocity would be limited according to equation (9). Otherwise, the beam front velocity would be faster in proportion to the amount of magnetic neutralization.

## 5.3 Average Velocity of Electrons in the Beam

In the previous section an upper bound to beam front propagation velocity was found, based on energy considerations. In this section we consider the velocity of electrons within the beam, in the steady state. The average forward velocity will be less than that as determined from the accelerating potential because of the oscillatory nature of the trajectory.

The average forward velocity will be calculated based on the following basic equations of motion for an electron moving in a uniform beam of radius $r_b$:

$$\frac{d\beta_r}{dt} = - \frac{A_o v_z}{r_b} (r/r_b) \tag{11}$$

$$\frac{d\beta_z}{dt} = \frac{A_o v_r}{r_b^2} r \tag{12}$$

where:

$$A_o = \frac{I_o}{8500\,\gamma} = \frac{2\eta}{\gamma} \beta_{z,o} \tag{13}$$

Equation (12) can be solved for $\beta_z(r)$;

$$\beta_z(r) = \beta_{z,o} + \frac{1}{2} \frac{A_o (r^2 - r_i^2)}{r_b^2} \tag{14}$$

where $r_i$ is the initial radius of the electron.

Averaging as if the trajectory were sinusoidal (which it nearly is for $A_o \sim 1$), $< r^2 > = 1/2\, r_i^2$ and

$$< \beta_z > = \beta_{z,o} - \frac{A_o r_i^2}{4 r_b^2} \tag{15}$$

For an electron starting at the outside of the beam, $r_i = r_b$, (15) becomes:

$$<\beta_z(1)> = \beta_{z,o} - \frac{A_o}{4} \tag{16}$$

For a 40 k A, 1.5 MeV beam $A_o = 1.18$, and

$$<\beta_z(1)> = 0.69$$

Just as for the beam front propagation velocity the extent to which the beam is magnetically neutralized affects this result. $<\beta_z>$ increases for increased magnetic neutralization.

## 5.4 Computed Trajectories in a Drift Tube

A computer program has been written to calculate the trajectories in a drift tube, i.e. a tube free of all applied fields. Each trajectory represents a cylindrical shell of current, the sum of the currents carried by the trajectories being equal to the beam current. The trajectory motion is calculated step-by-step using the Lorentz force:

$$F = q(E + v \times B)$$

where E and B are the self fields of the beam. The electric field at any point in the cylinder shown in Figure 75 is computed from a potential $\phi(r, z)$ as follows:

$$E_r = -\frac{\partial\phi}{\partial r}(r, z) \tag{17}$$

$$E_z = \frac{\partial\phi}{\partial z}(r, z) \tag{18}$$

The potential $\phi$ (r, z) as determined by a Green's function technique is given in terms of the beam's space charge as follows:

$$\phi\ (r, z) = \frac{4}{\epsilon L} \sum{}' \epsilon_{mn}\, Q_{mn}\, J_o\, (\lambda_m\, r/a)\ \sin \frac{n\pi}{(n\pi\ z/L)} \tag{19}$$

where:

$$Q_{mn} = \iint J_o\, (\lambda_m\, r/a)\ \sin\ (n\pi\ z/L)\, \rho\ (r, z)\ dr dz \tag{20}$$

The integration extends over the source points, i.e. the whole volume of the beam.

The magnetic field is determined from ampere's law. Because of the cylindrical symmetry of the beam, the magnetic field at any radius depends only on the total current within that radius. Thus ampere's law:

$$\int \vec{B} \cdot d\vec{\ell} = \int \vec{J} \cdot d\vec{s} \tag{21}$$

becomes,

$$B_\theta\, (r, z) = \frac{\mu_o}{2\pi r} \sum_{k=1}^{L} I_k = \frac{\mu_o}{r\,(L)} \sum_{k=1}^{L} \frac{v_z(k)\, r_o(k)\, J_o(k)}{r\,(k)} \tag{22}$$

In this equation $I_{kV}$ is the current carried by the kth trajectory, the trajectories are numbered in order from the beam axis outward to the Lth trajectory. $B_\Theta$ (r, z) is then the magnetic field at the Lth trajectory. The trajectories are calculated in parallel, i.e. the <u>r</u> co-ordinate for all trajectories is calculated for each <u>z</u> co-ordiante, then the <u>z</u> co-ordinate is incremented. This is done so that the self-magnetic field can be determined by equation 22.

After all trajectories have been calculated for the whole drift tube, the space charge which has been stored as the trajectory calculation was being done is used to calculate the potential and the electric field. Then using these new fields the whole trajectory calculation is repeated. As sufficient number of these major cycles is run until the trajectories from successive iterations agree. In this way a trajectory pattern self-consistent with electric and magnetic fields is assured.

The program is set up so that the only input required is the total beam current, injection energy, injection beam radius, and drift tube radius. The program then determines the number of trajectories to be calculated and proceeds to calculate them.

Results of the trajectory calculations show that if there is no space charge neutralization, the beam on entering the drift tube pinches near the window (vacuum pinch) and then blows up.

Figures 76 through 78 show trajectories for various sets of parameters for the case of complete space charge neutralization, but no magnetic neutralization, i.e. no backstreaming current within the beam.

For Figure 76 the parameters are as follows:

$I_o$ = 24,000 amperes
$V_o$ = 2.0 MeV
$r_{bo}$ = 2.0 cm
$r_{co}$ = 7.5 cm
$\nu/\gamma$ = 0.289

Rather surprisingly, the trajectories for this relatively low $\gamma/\gamma$ ratio are decidedly not those predicted by the Lawson model, i.e. they are not sinusoidal. In particular the Lawson wavelength (paraxial approximation) for this beam is:

$$\lambda = \frac{2\pi r_b}{2\nu/\gamma} = 16.2 \text{ cm}$$

Thus we would expect from paraxial considerations the first pinch to occur at $\lambda/4$ = 4.1 cm. From Figure 76, however, we see that electrons first cross

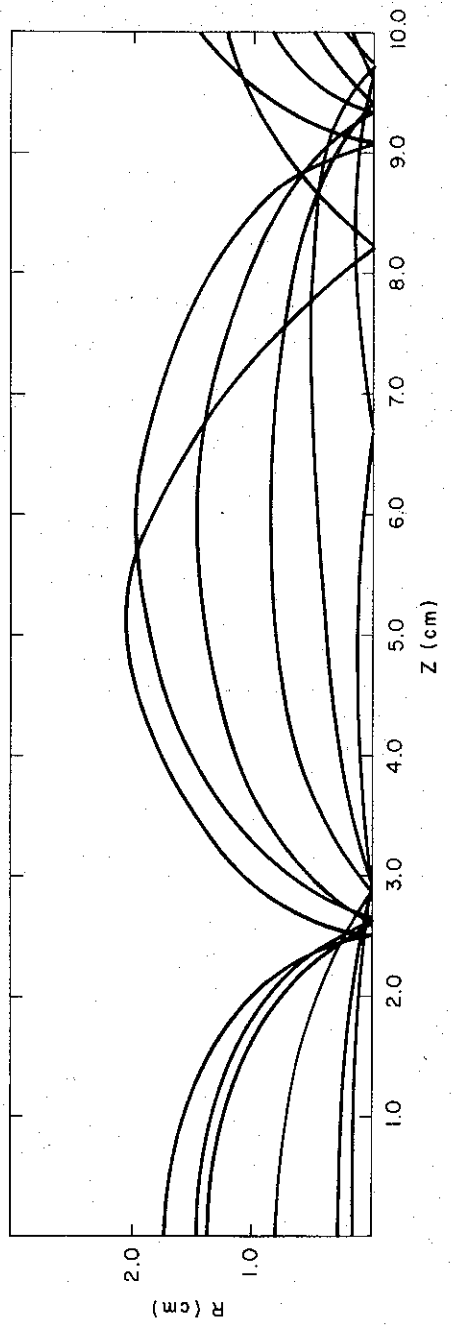

Figure 76. Electron Trajectories in Drift Tube

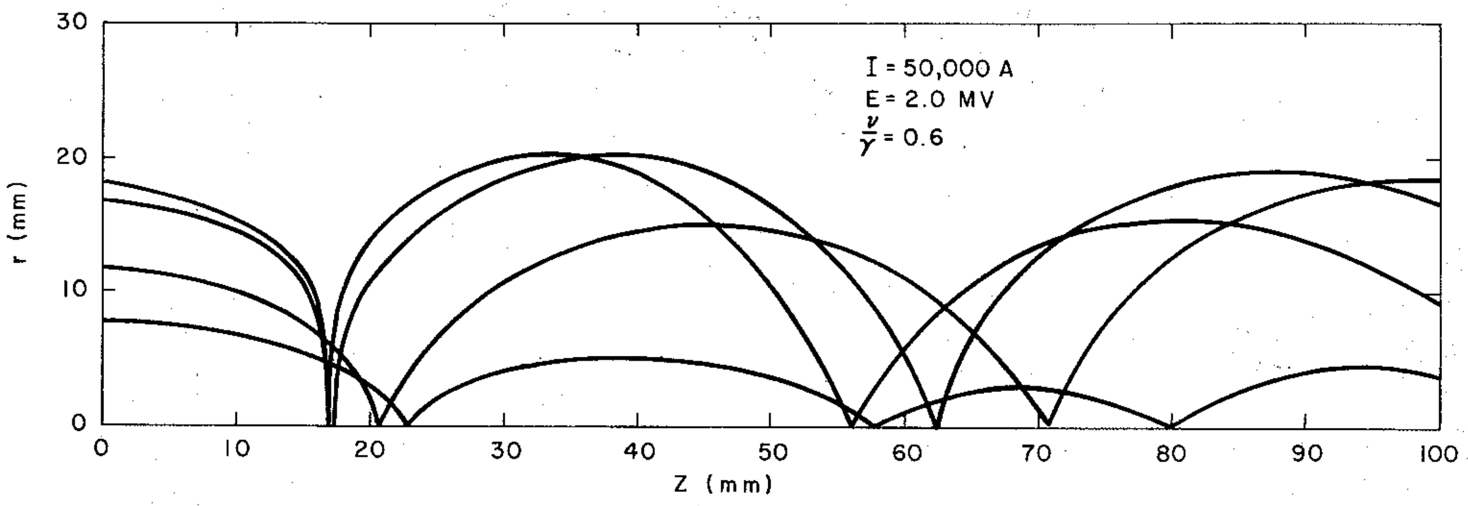

Figure 77. Electron Trajectories in Drift Tube (Space Charge Neutralized)

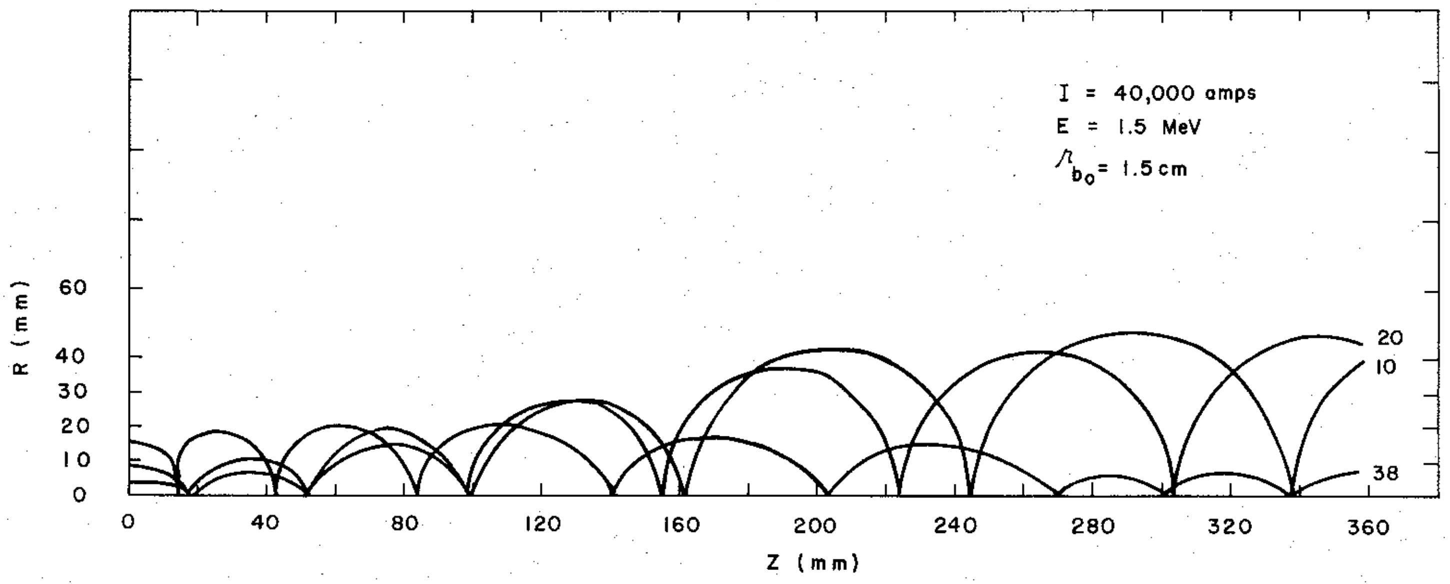

Figure 78. Electron Trajectories in Drift Region - Space Charge Neutralized No Magnetic Neutralization

1-4353

the axis between 2.5 cm and 3.0 cm. It is reasonable that our calculation would predict an earlier pinch point than the paraxial theory.

In the paraxial approximation, the magnetic field goes as r; the magnetic field in our case does not decrease so fast as r decreases, because the effect on the magnetic field of the increased current along and near the axis is taken into account. This stronger field near the axis increases the inward force on the trajectory and causes it to cross the axis earlier.

A second effect of the increased magnetic field due to collapsing trajectories is the loss of coherence of the trajectories as shown in Figure 76. Whereas in the Lawson theory the beam would remain coherent every $\lambda/2$ along the beam axis, our calculations show that actually the beam starts to lose coherence after the first pinch.

Increased current causes even greater loss of coherence as shown by Figure 77 for which the parameters are the same as before, except I = 50 k A, $\nu/\gamma = 0.6$.

The parameters chosen for Figure 78 closely related to our experimental values, are as follows:

$I_o = 40$ k A
$V_o = 1.5$ MV
$r_{bo} = 1.5$ cm
$r_c = 7.5$ cm

The effect of the beam's loss of coherence at the pinch points on beam propagation is clearly indicated in this calculation. The beam, even though it is assumed space charge neutralized, spreads. Higher injection current would lead to increased spreading up to a certain point. At some current, (near $\nu/\gamma = 1$) for a given voltage we know that electron turn around occurs and the beam does not propagate at all.

## 5.5 Return Current and Beam Propagation

In this section the role of plasma return currents inside the beam will be discussed. It will be shown that under certain conditions such a current can exist in sufficient amount to cancel the beam current and thus reduce the azimuthal magnetic field which depends on net current. This reduction of the magnetic field prevents over focusing which leads to beam expansion as shown in Figures 76 through 78 or which can lead in the extreme to beam stopping.

## 5.6 Analysis

A schematic for our model is shown in Figure 79. A beam of radius $r_b$ uniform in the z direction is envisioned propagating in a drift tube of radius $r_c$ filled with a conducting plasma. The beam current is taken to be rising exponentially in time as follows:

$$J_{Beam} = J_{max} (1 - e^{-\alpha t}) \quad r \leq r_b \tag{23}$$

$$J_{Beam} = 0 \quad r > r_b \tag{24}$$

This assumption of time variation but no spatial variation in the z direction is justified only if the beam risetime is long compared to the transit time for the section of beam under consideration.

The plasma current is simply:

$$J_{plasma} = \sigma E_z \tag{25}$$

where $E_z$ is the electric field induced by the rising beam current.

The appropriate Maxwell's equations are:

$$\nabla \times \vec{E} = - \dot{\vec{B}} \tag{26}$$

$$\nabla \times B = \mu_o \left[ \vec{J}_{Beam} + \vec{J}_{plasma} \right] \tag{27}$$

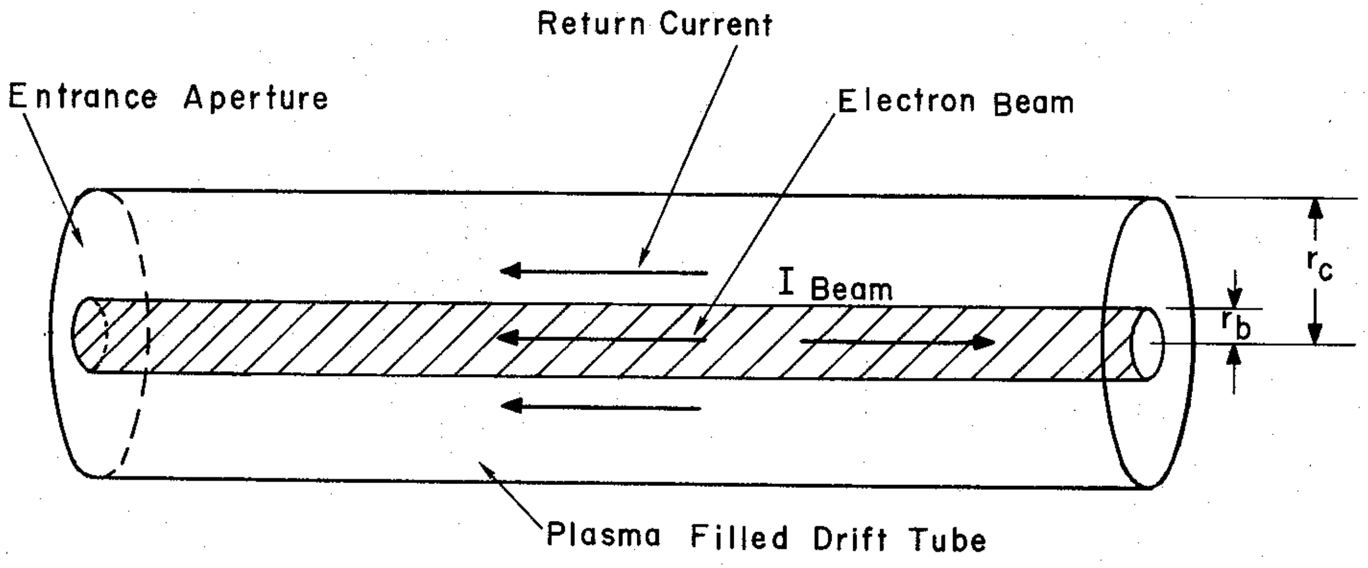

Figure 79. Schematic for Return Current Calculation

Combining (26) and (27), we get after Laplace transforming:

$$\frac{1}{r}\frac{\partial}{\partial r}\left(r\frac{\partial E_z}{\partial r}\right) - \mu_o \sigma sE = (sI(s) - I_o)\frac{\mu_o}{\pi r_b^2} \tag{28}$$

where $E_z$ is the electric field driving the return current and the term on the right due to the beam current is the driving term.

A Green's function for the cylindrical symmetric case is established as follows:

$$\nabla^2 G + k^2 G = -\frac{\delta(r - r_o)}{r} \tag{29}$$

$$\nabla^2 J_o(k_n r) + k_n^2 J_o(k_n r) = 0$$

where $_n$ is determined by:

$$J_o(k_n r_c) = 0$$

$$G = \Sigma_n A_n J_o(\ _n r)$$

$$\Sigma A_n (k^2 - k_m^2) J_o(k_m r) = -\frac{\delta(r - r_o)}{r}$$

Multiply by $r J_o(k_n r)$ and integrate to get $A_n$

$$A_n \int_o^{r_c} r J_o^2(k_n r)\, dr = \frac{J_o(k_n r_o)}{k_n^2 - k^2}$$

So:

$$G = \sum_n \frac{J_o(k_n r_o)\, J_o(k_n r)}{(k_n^2 - k^2) \int_o^{r_c} r\, J_o^2(k_n r)\, dr}$$

The electric field will then by given as (in the frequency domain),

$$E(r, s) = \int f(r, s)\, G(r, s)\, 2\pi\, r\, dr$$

and the return current density will be,

$$J_{return}(r, s) = \sigma \int f(r, s)\, G(r, s)\, 2\pi r dr$$

where:

$$f(r, s) = \left[ s\, I(s) - I_o \right] \frac{\mu_o}{\pi r_b^2} \quad r < r_b$$

$$f(r, s) = 0 \quad r > r_b$$

Integrating, we get the total return current inside a radius r,

$$I(r, s) = \int_o^r J(r, s)\, 2\pi\, r\, d\, r$$

Carrying out these integrations and inverting the Laplace transforms, we finally get the result below:

$$I_{\text{return}}(r,t) = \frac{4\alpha}{r_b r_c^2}\, r \sum_n J_1(k_n r_b)\, J_1(k_n r) \Big/$$

$$ {}_n^2\, J_1^2(k_n r_c)\,(\alpha - {}_n^2/\mu_o\sigma)$$

$$\left[e^{-\alpha t} - e^{-\frac{kn^2}{\mu_o\sigma} t}\right] \qquad (37)$$

Some results from equation (37) are shown in Figures 80 and 81. These show that if the conductivity is high, the plasma return current tends to be inside the beam, and therefore able to magnetically neutralize the beam.

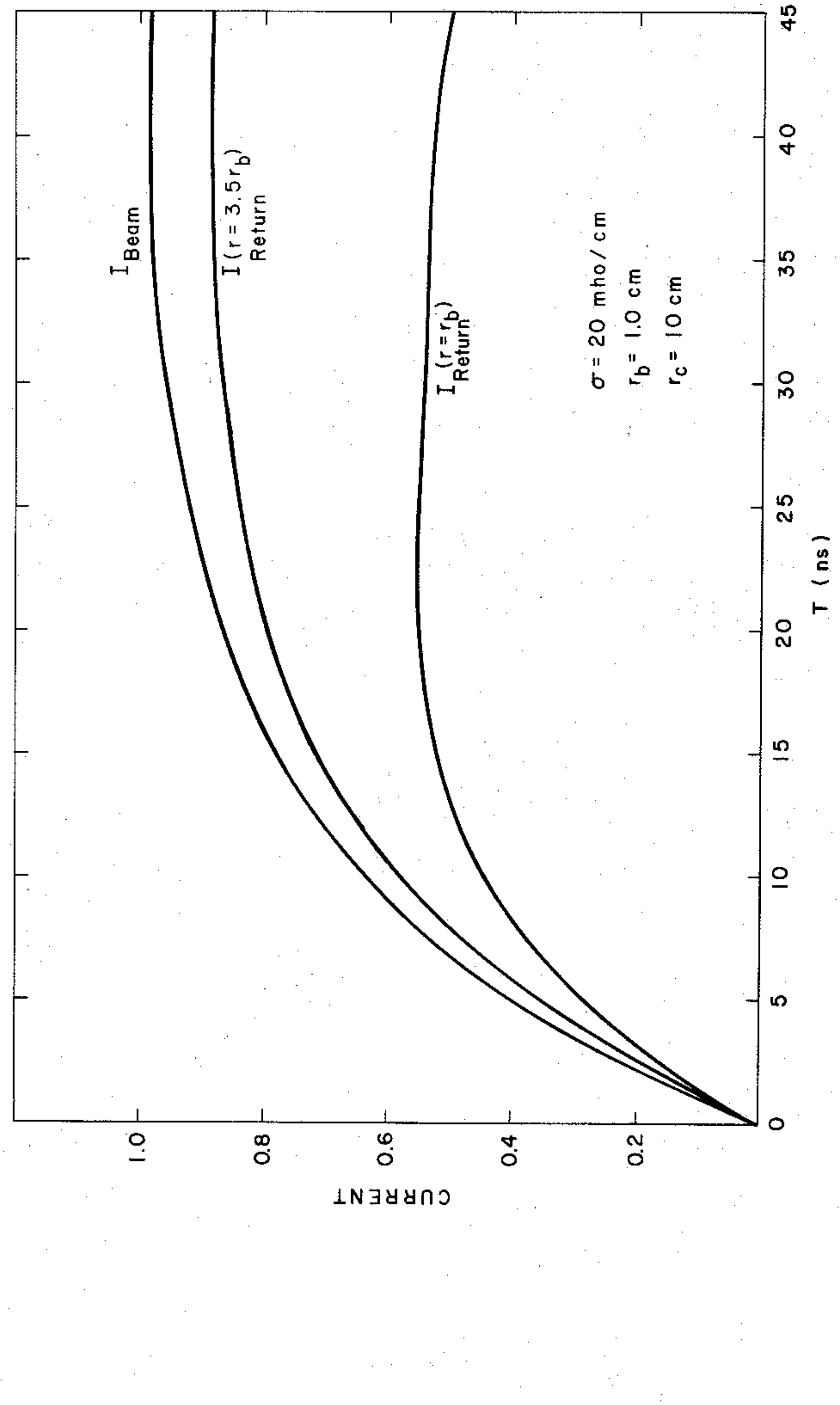

Figure 80. Return Current for R = $R_b$ and R = 3.5 $R_b$

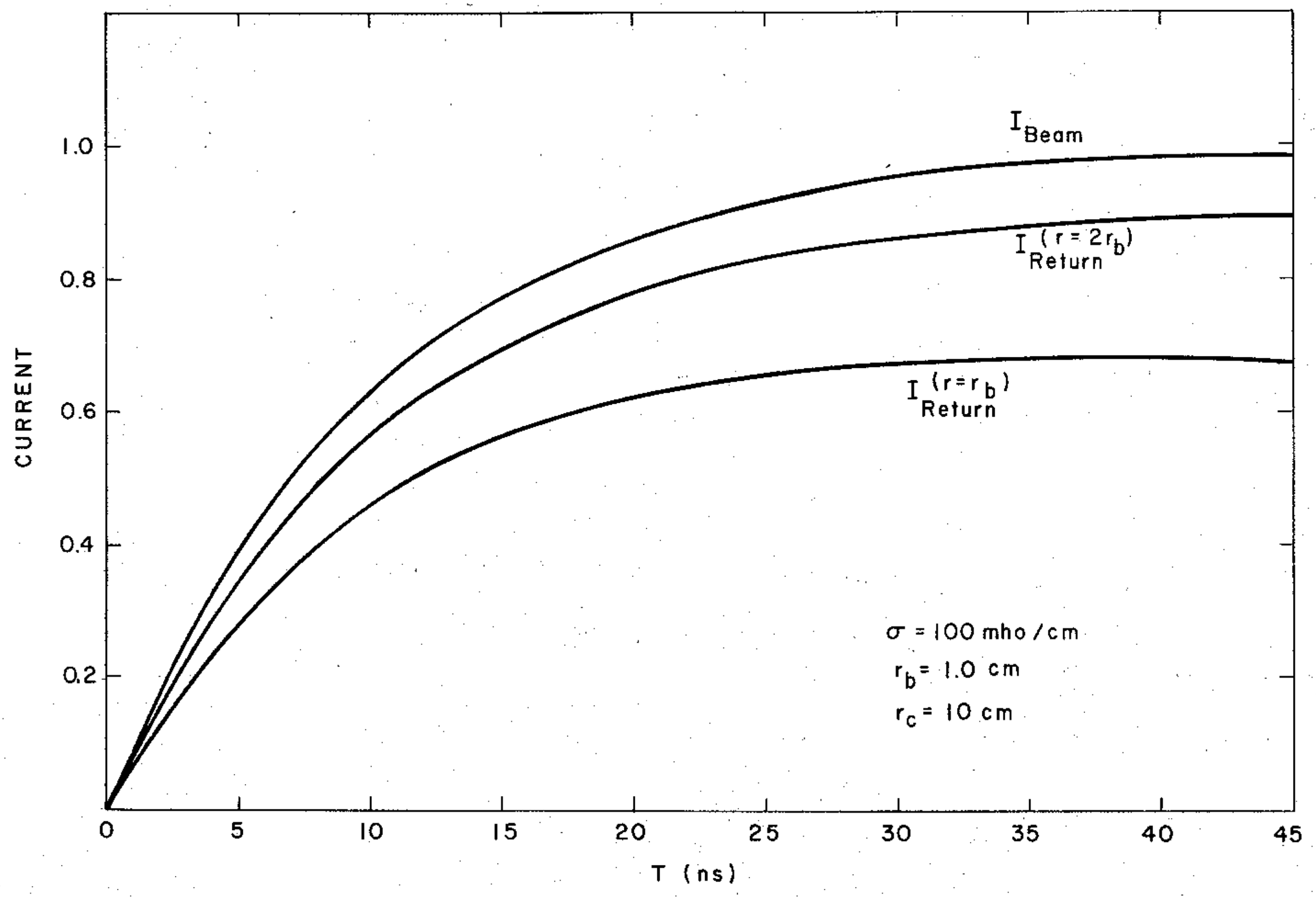

Figure 81. Return Current for $R = R_b$ and $R = R_b$

# SECTION 6

# REFERENCES

( 1) Final Report, Contract DA-49-146-XZ-553 (I); Final Report, Contract DA-49-146-XZ-553 (II).

( 2) R.A. Alpher and D.W. While, Physics of Fluids, 2, 162 (1959)

( 3) R.G. Buser and J.J. Kainz, Applied Optics, 3, 1495, (1964)

( 4) A.J. Alcock and S.A. Ramsdon, J. Appl. Phys. Letters, 8, 187, (1966)

( 5) C. David, P.V. Avigonix, H. Weichel, C. Bruce and K.D. Pyatt, IEEE Journal of Quantum Electronics, QE-2, 493 (1966)

( 6) L. Spitzer, "Physics of Fully Ionized Gases", p. 50, Interscience Publishers, New York (1956)

( 7) N. Rostoker (Private Communication)

( 8) R.F. Post, Reviews of Modern Physics, 28, 338, (1956)

( 9) J.E. Rizzo, Journal of Applied Physics, 11, (November 1969)